

**Shining Light on Dark Matter,  
One Photon at a Time**

by

Brandon Leigh Allen

Submitted to the Department of Physics  
in partial fulfillment of the requirements for the degree of

Doctorate of Science in Physics

at the

MASSACHUSETTS INSTITUTE OF TECHNOLOGY

June 2019

© Massachusetts Institute of Technology 2019. All rights reserved.

Author .....  
Department of Physics  
May 18, 2019

Certified by .....  
Christoph E.M. Paus  
Professor  
Thesis Supervisor

Accepted by .....  
Nergis Mavalvala  
Associate Department Head for Education



**Shining Light on Dark Matter,  
One Photon at a Time**

by

Brandon Leigh Allen

Submitted to the Department of Physics  
on May 18, 2019, in partial fulfillment of the  
requirements for the degree of  
Doctorate of Science in Physics

**Abstract**

A search is conducted for new physics in final states containing a photon and missing transverse momentum in proton-proton collisions at  $\sqrt{s} = 13$  TeV. The data collected by the CMS experiment at the CERN LHC correspond to an integrated luminosity of 35.9 inverse femtobarns. No deviations from the predictions of the standard model are observed. The results are interpreted in the context of dark matter production and limits on new physics parameters are calculated at 95% confidence level. For the two simplified dark matter production models considered, the observed (expected) lower limits on the mediator masses are both 950 (1150) GeV for 1 GeV dark matter mass.

Thesis Supervisor: Christoph E.M. Paus

Title: Professor



## Acknowledgments

This is the acknowledgements section. You should replace this with your own acknowledgements.



# Contents

<b>1</b>	<b>The Standard Model</b>	<b>11</b>
1.1	Strong Interactions . . . . .	13
1.2	Renormalization and Hadrons . . . . .	14
1.3	Electroweak Interactions . . . . .	16
1.4	Electroweak Symmetry Breaking . . . . .	17
1.5	Fermion Masses . . . . .	19
1.6	Flavor Mixing . . . . .	20
1.7	Summary . . . . .	21
<b>2</b>	<b>Dark Matter</b>	<b>25</b>
2.1	Astrophysical Evidence . . . . .	26
2.1.1	Galactic Clusters . . . . .	26
2.1.2	Galactic Rotation Curves . . . . .	27
2.1.3	Gravitational Lensing . . . . .	28
2.1.4	Cluster Collisions . . . . .	29
2.2	Relic Density . . . . .	32
2.3	Dark Matter Candidates . . . . .	34
2.3.1	Weakly-Interacting Massive Particles . . . . .	35
2.3.2	Axions . . . . .	35
2.3.3	Sterile Neutrinos . . . . .	36
2.4	Simplified Models for LHC . . . . .	38
2.5	Non-collider Searches . . . . .	40
2.5.1	Direct Detection . . . . .	40

2.5.2	Indirect Detection . . . . .	43
2.6	Summary . . . . .	45
<b>3</b>	<b>The Large Hadron Collider</b>	<b>47</b>
3.1	Experimental Apparatus . . . . .	47
3.2	Collider Phenomenology . . . . .	49
3.2.1	Parton Distribution Functions . . . . .	51
3.2.2	Hard Scattering . . . . .	52
3.2.3	Parton Shower . . . . .	52
3.2.4	Hadronization . . . . .	53
<b>4</b>	<b>The CMS Detector</b>	<b>55</b>
4.1	Inner Trackers . . . . .	58
4.2	Electromagnetic Calorimeter . . . . .	60
4.2.1	Preshower Detector . . . . .	62
4.3	Hadronic Calorimeter . . . . .	62
4.4	Muon Chambers . . . . .	64
4.5	Online Trigger System . . . . .	67
4.6	Detector Simulation . . . . .	69
<b>5</b>	<b>Global Event Reconstruction</b>	<b>71</b>
5.1	Particle Flow Elements . . . . .	73
5.1.1	Tracks . . . . .	73
5.1.2	Primary Vertexing . . . . .	74
5.1.3	Secondary Vertexing . . . . .	75
5.1.4	ECAL Superclusters . . . . .	75
5.1.5	HCAL Clusters . . . . .	76
5.1.6	Muon Segments . . . . .	77
5.1.7	Isolation . . . . .	77
5.2	Particle Identification . . . . .	79
5.2.1	Muons . . . . .	79

5.2.2	Electrons . . . . .	80
5.2.3	Isolated Photons . . . . .	81
5.2.4	Hadrons . . . . .	83
5.2.5	Jets . . . . .	85
5.2.6	Missing Tranverse Energy . . . . .	86
5.2.7	ECAL gain-switch effect . . . . .	87
<b>6</b>	<b>The Monophoton Analysis</b>	<b>89</b>
6.1	Dataset . . . . .	90
6.1.1	Trigger Efficiency . . . . .	91
6.1.2	Pileup Reweighting . . . . .	92
6.2	Event Selection . . . . .	94
6.2.1	Signal Regions . . . . .	95
6.2.2	Control Regions . . . . .	95
6.2.3	Proxy Samples . . . . .	96
6.2.4	Measurement Samples . . . . .	97
6.3	Efficiencies and Scale Factors . . . . .	97
6.3.1	$e/\gamma$ ID Efficiency . . . . .	98
6.3.2	$\gamma$ -specific ID Efficiency . . . . .	103
6.3.3	Lepton Veto Efficiency . . . . .	108
6.4	Misidentified electrons . . . . .	111
6.5	Misidentified hadrons . . . . .	113
6.6	Irreducible backgrounds . . . . .	116
6.6.1	Simulation of $V+\gamma$ Processes . . . . .	116
6.6.2	Data-driven Control Regions . . . . .	121
6.7	Beam halo . . . . .	125
6.8	ECAL spikes . . . . .	130
6.9	Minor SM Backgrounds . . . . .	138
6.10	Statistical Interpretation . . . . .	138
6.11	Results . . . . .	139

6.11.1	Limits . . . . .	142
6.11.2	Comparison to Results from Other Experiments . . . . .	143
6.11.3	Interpretation of Additional Models . . . . .	144

# Chapter 1

## The Standard Model

The Standard Model (SM) of particle physics describes the physical properties and dynamics of fermions, the fundamental constituents of matter, and their interactions in the language of a Lorentz-invariant quantum field theory (QFT). The discussion of the SM in this chapter is heavily indebted to the book *Modern Particle Physics* by Mark Thomson [1], in both organization and content. Additional references are included where necessary.

The Standard Model consists of a set of fermion fields, shown in Table 1.1, and the local gauge symmetry group that acts on them

$$G_{\text{SM}} = \text{SU}(3)_C \times \text{SU}(2)_L \times \text{U}(1)_Y, \quad (1.1)$$

which is composed of the subgroups

$$\begin{aligned} G_{\text{QCD}} &= \text{SU}(3)_C \quad \text{and} \\ G_{\text{EWK}} &= \text{SU}(2)_L \times \text{U}(1)_Y, \end{aligned} \quad (1.2)$$

corresponding to the strong and electroweak interactions, respectively. Each fermion field exists in a unique representation of  $G_{\text{SM}}$ , also summarized in Table 1.1. The possible representations of  $\text{SU}(3)_C$  are triplet, conjugate, and singlet, denoted by **3**,  **$\bar{3}$** , and **1**, respectively, while the possible representations of  $\text{SU}(2)_L$  are doublet and

singlet, denoted by **2** and **1**, respectively. All fermions exist in the singlet representation of  $U(1)_Y$ , only distinguished by differing values of the weak hypercharge  $Y$ . Conversely, all fermions in non-singlet representations of  $SU(3)_C$  and  $SU(2)_L$  have the same interaction strength, a feature known as universality.

Name	Symbol	$Y$	$SU(2)_L$ rep.	$SU(3)_C$ rep.
Left-handed quark	$q_L$	$\frac{1}{6}$	<b>2</b>	<b>3</b>
Right-handed up-type quark	$u_R$	$\frac{2}{3}$	<b>1</b>	<b>3</b>
Right-handed down-type quark	$d_R$	$-\frac{1}{3}$	<b>1</b>	<b>3</b>
Left-handed lepton	$\ell_L$	$-\frac{1}{2}$	<b>2</b>	<b>1</b>
Right-handed charged lepton	$e_R$	-1	<b>1</b>	<b>1</b>
Right-handed neutrino	$\nu_R$	$\frac{1}{6}$	<b>1</b>	<b>1</b>

Table 1.1: The categories of SM fermions and the action of the SM local gauge symmetry group  $G_{SM}$ . Each category contains three members, one for each generation of the Standard Model. A corresponding table exists for the charge conjugated fields representing the anti-fermions. The subscripts  $L$  and  $R$  denote whether the field is left- or right-handed.

For each category of fermion listed in Table 1.1, there exist three generations or copies in the Standard Model, identical except for differing masses. The lepton electroweak doublets contain the left-handed charged leptons and neutrinos

$$\ell_L = \begin{pmatrix} \nu_e \\ e_L^- \end{pmatrix}, \begin{pmatrix} \nu_\mu \\ \mu_L^- \end{pmatrix}, \begin{pmatrix} \nu_\tau \\ \tau_L^- \end{pmatrix}, \quad (1.3)$$

and the right-handed lepton singlets contain the right-handed projections of the same leptons and neutrinos. The quark electroweak doublets contain the left-handed up-type and down-type quarks

$$q_L = \begin{pmatrix} u_L \\ d_L \end{pmatrix}, \begin{pmatrix} c_L \\ s_L \end{pmatrix}, \begin{pmatrix} t_L \\ b_L \end{pmatrix}, \quad (1.4)$$

and the right-handed quark singlets contain the right-handed projections of the same quarks. Quarks also exist in a strong triplet, which will be denoted with a superscript  $c$  as necessary.

## 1.1 Strong Interactions

The strong interactions of quarks and gluons are described by quantum chromodynamics (QCD) [2, 3], with the Lagrangian

$$\mathcal{L}_{\text{QCD}} = i\bar{q}_f^a \not{D}^{ab} q_f^b + m_f \bar{q}_f^a q_f^a - \frac{1}{4} G_{\mu\nu}^a G^{a,\mu\nu} + \theta \frac{g_s^2}{72\pi^2} \epsilon_{\mu\nu\rho\sigma} G^{c,\mu\nu} G^{c,\rho\sigma}, \quad (1.5)$$

where repeated indices are contracted. The  $q_f^a$  are the quark-field Dirac spinors of flavor  $f \in \{u, d, c, s, t, b\}$ , color  $a \in \{r, g, b\}$  the basis elements of the triplet representation of  $\text{SU}(3)_C$ , and mass  $m_f$ . The first term in Equation 1.5 contains the QCD covariant derivative

$$D_\mu^{ab} = \delta^{ab} \partial_\mu - ig_s \sum_c t_c^{ab} G_{c,\mu}, \quad (1.6)$$

where  $g_s$  is the strong interaction coupling strength with associated coupling constant  $\alpha_s = g_s^2/(4\pi)$ , the  $t_c$  are the eight  $3 \times 3$  Hermitian traceless matrices that serve as the generators of the triplet representation of  $\text{SU}(3)_C$ , and the  $G_c$  are the corresponding eight gluon fields. The third term in Equation 1.5 contains the gluon field strength tensors

$$G_{\mu\nu}^a = \partial_\mu G_\nu^a - \partial_\nu G_\mu^a - g_s f^{abc} G_\mu^b G_\nu^c, \quad (1.7)$$

where  $f^{abc}$  are the structure constants of  $\text{SU}(3)_C$ . The non-Abelian structure of the  $\text{SU}(3)_C$  group allows for 3-gluon and 4-gluon interactions in addition to the quark-antiquark-gluon interactions.

The last term in Equation 1.5 violates CP conservation and produces a non-zero electric dipole moment (EDM) for the neutron. Experimental limits on the neutron EDM constrain the observed QCD vacuum angle  $\theta$  to be smaller than  $10^{-10}$  [4]. The Peccei-Quinn theory [5, 6] provides a possible explanation for this contradiction by introducing the hypothetical axion particle  $a$  with the following Lagrangian

$$\mathcal{L}_a = \frac{1}{2} \partial_\mu a \partial^\mu a + \frac{a}{f_a} \frac{g_s^2}{72\pi^2} \epsilon_{\mu\nu\rho\sigma} G^{c,\mu\nu} G^{c,\rho\sigma}, \quad (1.8)$$

where  $f_a$  is axion decay constant that determines its characteristic scale. The second

term in Equation 1.8 cancels the last term in Equation 1.5 when the axion field dynamically assumes its vacuum expectation value  $\langle a \rangle = -f_a\theta$ . The axion is a potential dark matter candidate.

## 1.2 Renormalization and Hadrons

Due to higher-order corrections to propagators in a QFT, physical quantities such as coupling constants and masses acquire a scale-dependence, where the value of the quantity changes as a function of the probed energy scale  $q^2$ . The process of recovering scale-invariance is called renormalization and ensures that any divergent terms from the higher-order corrections cancel out in the physical values. Given the value of an arbitrary coupling constant  $\alpha$  at some known scale  $\mu^2$ , the value of  $\alpha$  at arbitrary scale  $q^2$  is

$$\alpha(q^2) = \frac{\alpha(\mu^2)}{1 - \alpha(\mu^2) [\Pi(q^2) - \Pi(\mu^2)]}, \quad (1.9)$$

where  $\Pi(q^2)$  and  $\Pi(\mu^2)$  are the self-energy correction of the propagator at scales  $q^2$  and  $\mu^2$ . While these individual terms are separately divergent, their difference is finite and calculable.

For values of  $q^2$  and  $\mu^2$  larger than the QCD confinement scale  $\Lambda_{\text{QCD}} = 218 \text{ MeV}$ , the difference between the gluon self-energy corrections to one-loop order is given by

$$\Pi_s(q^2) - \Pi_s(\mu^2) \approx -\frac{\beta_{\text{QCD}}}{4\pi} \ln \left( \frac{q^2}{\mu^2} \right) \quad (1.10)$$

where  $\beta_{\text{QCD}}$  depends on the number of quark and gluon loops. For  $N_c$  colors and  $N_f$  quark flavors with mass below  $|q|$ ,

$$\beta_{\text{QCD}} = \frac{11N_c - 2N_f}{12\pi}. \quad (1.11)$$

In the Standard Model,  $N_c = 3$  and  $N_f \leq 6$  regardless of energy, thus  $\beta_{\text{QCD}}$  is always

positive. Combining Equations 1.9 and 1.10, the evolution of  $\alpha_s$  is given by

$$\alpha_s(q^2) = \frac{\alpha_s(\mu^2)}{1 + \beta_{\text{QCD}}\alpha_s(\mu^2) \ln\left(\frac{q^2}{\mu^2}\right)} \approx \frac{1}{\beta \ln\left(\frac{q^2}{\Lambda_{\text{QCD}}^2}\right)} \quad (1.12)$$

for a sufficiently large energy scale  $q^2 \gg \Lambda_{\text{QCD}}^2$ . Through electron-positron collisions, the value of  $\alpha_s$  at the  $Z$ -pole has been measured to be  $\alpha_s(m_Z^2) = 0.1181 \pm 0.0011$  [4].

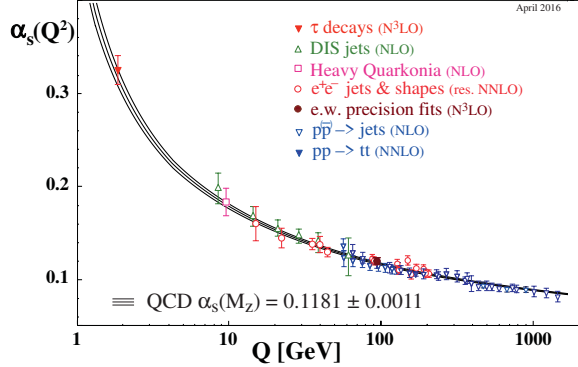


Figure 1-1: Running of  $\alpha_s$  as a function of energy. Reprinted from Reference [4].

From Equation 1.12, we see that  $\alpha_s$  decreases with increasing  $q^2$  as shown in Figure 1-1. At  $|q| \sim 1 \text{ GeV}$ , the value of  $\alpha_s$  is of  $\mathcal{O}(1)$  confining quarks and gluons to hadrons in a strongly-bound non-perturbative state. However,  $|q| \gtrsim 100 \text{ GeV}$ , we have  $\alpha_s \approx 0.1$  which is small enough that perturbation theory can be used and quarks can be treated as quasi-free particles. This property of QCD is known as asymptotic freedom [7].

Below the confinement scale  $\Lambda_{\text{QCD}}$ , colored objects are always confined to color singlet states and no objects with non-zero color charge propagate as free particles. This low-energy non-perturbative phenomenon is known as color confinement. Thus, free quarks and gluons are not observed in nature, only in colorless bound states called hadrons [8]. The most common states consist of a quark-antiquark pair or three quarks, called mesons and baryons, respectively. Rarer pentaquark states have recently been found by the LHCb collaboration [9].

### 1.3 Electroweak Interactions

The electroweak interactions of fermions are described by the  $SU(2)_L \times U(1)_Y$  gauge group [10–12], with the Lagrangian

$$\mathcal{L}_{EWK} = i\bar{\psi}_i \not{D} \psi_i - \frac{1}{4} \vec{W}_{\mu\nu} \cdot \vec{W}^{\mu\nu} - \frac{1}{4} B_{\mu\nu} B^{\mu\nu} \quad (1.13)$$

where repeated indices are contracted and  $\psi \supseteq \{q_L, u_R, d_R, \ell_L, e_R, \nu_R\}$  is the set of SM fermions, and the gauge field tensors are given by

$$\begin{aligned} B_{\mu\nu} &= \partial_\mu B_\nu - \partial_\nu B_\mu \quad \text{and} \\ \vec{W}_{\mu\nu} &= \partial_\mu \vec{W}_\nu - \partial_\nu \vec{W}_\mu + g \vec{W}^\mu \times \vec{W}^\nu, \end{aligned} \quad (1.14)$$

where  $\vec{W}_\mu$  and  $B_\mu$  are the gauge fields for  $SU(2)_L$  and  $U(1)_Y$ , respectively, and  $g$  is the coupling strength for  $SU(2)_L$ . The first term in Equation 1.13 contains the EWK covariant derivative

$$D_\mu = \partial_\mu - ig\vec{T} \cdot \vec{W}_\mu - ig'YB_\mu, \quad (1.15)$$

where  $g'$  is the coupling strength for  $U(1)_Y$ ,  $Y$  is the  $U(1)_Y$  hypercharge of the fermion field, and  $\vec{T}$  are the generators of the doublet representation of  $SU(2)_L$ . The generators can be written in terms of the Pauli spin matrices  $\vec{T} = \vec{\sigma}/2$  and only have non-zero action on left-handed particles. The values of the hypercharge  $Y$  shown in Table 1.1 are chosen such that the physical electric charge of each fermion is given by  $Q = T_3 + Y$ .

However, this theory of the electroweak interactions is not sufficient to explain the observed behavior of the weak force. Equation 1.13 contains three massless gauge bosons for weak isospin and one massless gauge boson for hypercharge, but experimentally three massive weak gauge bosons and one massless photon have been observed. Introducing explicit mass terms of the form  $-m_W^2 W_\mu W^\mu$  to the Lagrangian breaks the  $SU(2)_L$  gauge invariance and makes the theory non-renormalizable. Spontaneous breaking of the  $SU(2)_L$  gauge invariance provides the mechanism we need to provide mass to the weak gauge bosons without breaking gauge invariance.

## 1.4 Electroweak Symmetry Breaking

The development of a dynamical photon mass in the Bardeen-Cooper-Schrieffer theory of superconductivity [13] provided the template for spontaneous symmetry breaking in the electroweak sector. Spontaneous symmetry breaking occurs when the vacuum is degenerate with none of the possible ground states exhibiting the symmetry of the underlying theory [14, 15]. However, as a consequence of the Nambu-Goldstone theorem [16, 17], massless spin-0 bosons appear after spontaneous symmetry breaking but no such particles are observed in nature. Fortunately, Brout, Englert, and Higgs as well as Guralnik, Hagen, and Kibble discovered that when an additional field is used to break a gauge symmetry, the gauge bosons acquire a nonzero mass by absorbing the Nambu-Goldstone bosons [18–23]. Building upon these ideas, Glashow, Weinberg, and Salam developed a theory of electroweak unification [10–12] that explained the observed massive weak bosons and t’Hooft and Veltman proved it was renormalizable [24]. We shall walk through the key points of these developments now.

The  $SU(2)_L$  symmetry is broken by introducing a left-handed complex scalar doublet  $\phi$  with  $Y_\phi = 1/2$  to the Lagrangian in the following manner

$$\mathcal{L}_{\text{EWK}} \mapsto \mathcal{L}_{\text{EWK}} + |D_\mu \phi|^2 + \mu^2 \phi^2 - \lambda |\phi|^4. \quad (1.16)$$

We choose to write this complex doublet, known as the complex Higgs field, in terms of four real-valued fields so that

$$\phi = \frac{1}{\sqrt{2}} \begin{pmatrix} \phi_1 + i\phi_2 \\ \phi_3 + i\phi_4 \end{pmatrix}. \quad (1.17)$$

Fortunately, the two self-interaction terms create a Higgs potential with a degenerate global minimum at the vacuum expectation value (vev)

$$v \equiv \langle |\phi| \rangle = \sqrt{\frac{\mu^2}{\lambda}}, \quad (1.18)$$

and through gauge rotations we set  $\langle \phi_{1,2,4} \rangle = 0$ , removing three degrees of freedom

and producing three massless Nambu-Goldstone bosons. The remaining degree of freedom is the real Higgs field  $H$  which expresses small perturbations around the vev in the third component of the complex Higgs field  $\phi_3 = v + H$ .

The kinetic term in Equation 1.16 couples the complex Higgs field to the EWK gauge bosons as follows at the vev

$$|D_\mu \phi|^2 = \frac{v^2}{8} \left[ (gW_\mu^1)^2 + (gW_\mu^2)^2 + (g'B_\mu - gW_\mu^3)^2 \right]. \quad (1.19)$$

Diagonalizing this term gives rise to the three massive weak bosons and the massless photon that we observe in nature:

$$\begin{array}{l} W_\mu^\pm \equiv \frac{1}{\sqrt{2}} (W_\mu^1 \mp W_\mu^2) \\ Z_\mu \equiv \cos \theta_W W_\mu^3 - \sin \theta_W B_\mu \\ A_\mu \equiv \sin \theta_W W_\mu^3 + \cos \theta_W B_\mu \end{array} \left| \begin{array}{l} m_W = \frac{1}{2}vg \\ m_Z = \frac{1}{2}v\sqrt{g^2 + (g')^2} \\ m_A = 0, \end{array} \right. \quad (1.20)$$

where  $\tan \theta_W = g'/g$  and  $\cos \theta_W = m_W/m_Z$ . With this, we rewrite Equation 1.13 in terms of the observed electromagnetic (EM), charged weaked (CC), and neutral weak (NC) currents as follows:

$$\begin{aligned} \mathcal{L}_{\text{EWK}} = & \bar{\psi}_i (i\cancel{D} - eQ\cancel{A}) \psi_i - \frac{g}{2\sqrt{2}} \bar{\psi}_i \left( T^+ W^+ + T^- W^- \right) \psi_i - \frac{1}{2} m_W^2 W_\mu^+ W^{-\mu} \\ & - \frac{g}{2 \cos \theta_W} \bar{\psi}_i (g_V - g_A \gamma^5) \cancel{Z} \psi_i - \frac{1}{2} m_Z^2 Z_\mu Z^\mu, \end{aligned} \quad (1.21)$$

where  $e = g' \cos \theta_W$  is the charge of the electron with associated coupling constant  $\alpha = e^2/(4\pi)$ ,  $T^\pm = (T_1 \mp iT_2)/\sqrt{2}$  are the weak isospin raising and lowering operators, and  $g_V = T_3$  and  $g_A = T_3 - 2Q \sin^2 \theta_W$  are the vector and axial-vector couplings for the neutral weak current. We can also expand Equation 1.16 about the vev giving us the following Higgs Lagrangian

$$\begin{aligned} \mathcal{L}_H = & \frac{1}{2} \partial_\mu H \partial^\mu H - \frac{1}{2} m_H^2 H^2 + \frac{m_H^2}{2v} H^3 + \frac{2m_W^2}{v} W_\mu^+ W^{-\mu} H + \frac{m_Z^2}{v} Z_\mu Z^\mu H \\ & + \frac{m_H^2}{8v^2} H^4 + \frac{m_W^2}{v^2} W_\mu^+ W^{-\mu} H^2 + \frac{m_Z^2}{2v^2} Z_\mu Z^\mu H^2, \end{aligned} \quad (1.22)$$

where  $m_H = \mu\sqrt{2}$ . Thus, we see that the real Higgs field  $H$  has trilinear and quartic couplings to itself and the weak gauge bosons with coupling strengths proportional to the mass squared of the appropriate boson.

## 1.5 Fermion Masses

Notice that Equation 1.21 does not contain a Dirac mass term like that found in Equation 1.5. This is because the term

$$m\bar{\psi}\psi = m(\bar{\psi}_L\psi_R + \bar{\psi}_R\psi_L) \quad (1.23)$$

mixes the left-handed and right-handed fermions leading to a Lagrangian that is no longer invariant under  $SU(2)_L$ . As the observed fermions are not massless, the Lagrangian given in Equation 1.13 is incomplete. Thankfully, introducing Yukawa couplings between the complex Higgs field  $\phi$  and the SM fermion fields provides an economical way to add mass terms for the fermions.

First, we start with the terms for charged leptons,

$$\mathcal{L}_Y^{\text{leptons}} = -\bar{\ell}_L Y_e \phi e_R - \bar{e}_R Y_e^\dagger \phi^\dagger \ell_L, \quad (1.24)$$

where  $Y_e$  is the Yukawa matrix for the charged leptons. In general, Yukawa matrices and thus mass matrices are non-diagonal and hence we need to convert from the electroweak eigenstates  $f_{L,R}$  to the mass eigenstates  $\tilde{f}_{L,R} = U_{L,R}^f f_{L,R}$  where  $U_{L,R}^f$  is a unitary matrix. With this we rewrite Equation 1.24 in terms of the mass eigenstates

$$\begin{aligned} \mathcal{L}_Y^{\text{leptons}} &= -\bar{\tilde{\ell}}_L U_L^e Y_e \phi U_R^{e\dagger} \tilde{e}_R - \bar{\tilde{e}}_R U_R^e Y_e^\dagger \phi^\dagger U_L^{e\dagger} \tilde{\ell}_L \\ &= -\bar{\tilde{\ell}}_L \tilde{Y}_e \phi \tilde{e}_R - \bar{\tilde{e}}_R \tilde{Y}_e^\dagger \phi^\dagger \tilde{\ell}_L, \end{aligned} \quad (1.25)$$

where  $\tilde{Y}_e = U_L^e Y_e U_R^{e\dagger}$  is the diagonalized Yukawa matrix for the charged leptons. After

electroweak symmetry breaking, these terms become

$$\begin{aligned}\mathcal{L}_Y^{\text{leptons}} &= -\frac{v+H}{\sqrt{2}} \left( \bar{e}_L \tilde{Y}_e \tilde{e}_R + \bar{e}_R \tilde{Y}_e^\dagger \tilde{e}_L \right) \\ &= -\left( 1 + \frac{H}{v} \right) \left( \bar{e}_L \tilde{M}_e \tilde{e}_R + \bar{e}_R \tilde{M}_e^\dagger \tilde{e}_L \right) \\ &= -\tilde{M}_e \bar{e} e - \frac{\tilde{M}_e}{v} \bar{e} e H,\end{aligned}\tag{1.26}$$

where  $\tilde{M}_e = v \tilde{Y}_e / \sqrt{2}$  is the diagonalized mass matrix for the charged leptons and  $e$  is the set of massive Dirac spinors for the charged leptons.

From Equation 1.26, we see that the Yukawa couplings between the complex Higgs field  $\phi$  and the charged leptons result in a Dirac mass term and a coupling to the real Higgs field  $H$  that is proportional to the mass of the charged leptons and the vev. The same procedure is used to introduce mass terms for the down-type quarks whereas for the neutrinos and up-type quarks we must use the conjugate doublet  $\phi_c = -i\sigma_2\phi^*$  in place of  $\phi$  to obtain the same result.

## 1.6 Flavor Mixing

For the charged leptons and up-type quarks, it is possible to define a basis of simultaneous electroweak and mass eigenstates, so in practice  $\tilde{Y}_{e,u} = Y_{e,u}$  as  $U_L^{e,u} = U_R^{e,u} = \mathbf{I}$ . However, it is not possible to do this for the neutrinos at the same time as the charged leptons or for the down-type quarks at the same time as the up-type quarks.

In Equation 1.21, the charged current term involves interactions between the up-type and down-type quarks and is not preserved under the transform  $f \rightarrow \tilde{f}$ . Writing this in terms of the mass eigenstates we have

$$\begin{aligned}\mathcal{L}_{\text{CC}} &= -\frac{g}{2\sqrt{2}} \left( \bar{u}_L T^+ W^+ d_L + \bar{d}_L T^- W^- u_L \right) \\ &= -\frac{g}{2\sqrt{2}} \left( \bar{u}_L T^+ W^+ V_{\text{CKM}} \tilde{d}_L + \bar{d}_L T^- W^- V_{\text{CKM}}^\dagger u_L \right),\end{aligned}\tag{1.27}$$

where  $V_{\text{CKM}} = U_L^{u\dagger} U_L^d$  is the Cabibbo-Kaboyshi-Maskawa matrix [25, 26] and  $u_L = \tilde{u}_L$

by construction. The CKM matrix is unitary with four free parameters, the mixing angles between quark generations  $\phi_{12}$ ,  $\phi_{23}$ , and  $\phi_{13}$  as well as a CP-violating phase  $\delta$ . In terms of these parameters, the CKM matrix is

$$V_{\text{CKM}} = \begin{pmatrix} c_{12} & s_{12} & 0 \\ -s_{12} & c_{12} & 0 \\ 0 & 0 & 1 \end{pmatrix} \times \begin{pmatrix} 1 & 0 & 0 \\ 0 & c_{23} & s_{23} \\ 0 & -s_{23} & c_{23} \end{pmatrix} \times \begin{pmatrix} c_{13} & 0 & s_{13}e^{-i\delta} \\ 0 & 1 & 0 \\ -s_{13}e^{i\delta} & 0 & c_{13} \end{pmatrix}, \quad (1.28)$$

where  $s_{ij} = \sin \phi_{ij}$  and  $c_{ij} = \cos \phi_{ij}$ . It has been experimentally determined that the CKM is mostly diagonal with  $s_{13} \ll s_{23} \ll s_{12} \ll 1$ .

The equivalent mixing matrix for the neutrinos is the Pontecorvo-Maki-Nakagawa-Sakata matrix  $U_{\text{PMNS}}$  [27–29], which converts from the mass eigenstates  $\nu_1$ ,  $\nu_2$ , and  $\nu_3$  to the electroweak eigenstates  $\nu_e$ ,  $\nu_\mu$ ,  $\nu_\tau$ . Unlike the CKM matrix, the PMNS matrix is non-diagonal resulting in stronger mixing in the neutrino sector. The values of the mixing angles  $\theta_{12}$ ,  $\theta_{23}$ , and  $\theta_{13}$  have been measured in neutrino oscillation experiments while the CP-violating phase  $\delta'$  has not yet been directly measured. From cosmological measurements of the large-scale structure of the universe, it is known that the sum of the neutrino masses is less than one eV.

## 1.7 Summary

The Standard Model has a total of 26 free parameters and 17 physical particles. The parameters are the twelve Yukawa couplings for the fermions, the four parameters of the CKM matrix, the four parameters of the PMNS matrix, the two coupling constants  $\alpha_s$  and  $\alpha$ , the masses of the weak gauge bosons  $m_W$  and  $m_Z$ , the mass of the Higgs boson  $m_H$ , and the QCD vacuum angle  $\theta$ . The best fit values of the SM parameters, excluding masses, are summarized in Table 1.2.

The physical particles are the single-particle states of the various mass eigenfields and their properties are summarized in Table 1.3. Each of the fermion fields has a corresponding anti-particle with the electromagnetic and color charges inverted. Most of these single-particle states have finite lifetimes and decay to lower energy

Parameter	Description	Best Fit Value
$\phi_{12}$	CKM 12-mixing angle	$13.1^\circ$
$\phi_{23}$	CKM 23-mixing angle	$2.4^\circ$
$\phi_{13}$	CKM 13-mixing angle	$0.4^\circ$
$\delta$	CKM CP-violating phase	0.995
$\sin^2 \theta_{12}$	PMNS 12-mixing angle	0.297
$\sin^2 \theta_{23}$	PMNS 23-mixing angle	0.437
$\sin^2 \theta_{13}$	PMNS 13-mixing angle	0.0214
$\delta'$	PMNS CP-violating phase	1.35
$\alpha_s$	QCD coupling constant	0.1181
$\alpha$	EM coupling constant	$1/137.036$
$\theta$	QCD vacuum angle	$< 10^{-10}$

Table 1.2: The free parameters of the Standard Model, not including masses [4]

Name	Symbol	Spin	Charge	Mass
up quark	$u$	$1/2$	$2/3$	2.2 MeV
down quark	$d$	$1/2$	$-1/3$	4.7 MeV
charm quark	$c$	$1/2$	$2/3$	1.28 GeV
strange quark	$s$	$1/2$	$-1/3$	95 MeV
top quark	$t$	$1/2$	$2/3$	173 GeV
bottom quark	$b$	$1/2$	$-1/3$	4.18 GeV
electron neutrino	$\nu_e$	$1/2$	0	-
electron	$e$	$1/2$	-1	511 keV
muon neutrino	$\nu_\mu$	$1/2$	0	-
muon	$\mu$	$1/2$	-1	105 MeV
tau neutrino	$\nu_\tau$	$1/2$	0	-
tau	$\tau$	$1/2$	-1	1.78 GeV
gluon	$g$	1	0	0
photon	$\gamma$	1	0	0
Z boson	$Z$	1	0	91.2 GeV
W boson	$W^\pm$	1	$\pm 1$	80.4 GeV
Higgs boson	$H$	0	0	125 GeV

Table 1.3: The physical particles of the Standard Model [4].

configurations. The only particles whose decays have not been observed are the photon, the electron, the neutrinos, and the proton (a baryon of flavor content  $uud$ ). Additionally, stable bound states of protons and neutrons (a baryon of flavor content  $udd$ ) exist in the form of atomic nuclei.



# Chapter 2

## Dark Matter

As a theory of the fundamental particles and forces of nature, the Standard Model should also help explain physics at the largest scales. The  $\Lambda$ CDM model [30] best explains all current cosmological observations including the structure of the cosmic microwave background; the abundances of hydrogen, helium, and lithium; the large-scale structure in the distribution of galaxies, and the accelerating expansion of the universe. However, results from many cosmological observations show that baryonic matter (matter consisting of various combinations of protons, neutrons, and electrons) only contributes  $\sim 5\%$  of the total energy of the universe, with radiation (photons and relativistic neutrinos) contributing less than a hundredth of a percent.

The remaining 95% of energy comes from just two sources:  $\sim 27\%$  from non-relativistic non-baryonic matter referred to as dark matter and  $\sim 68\%$  from an unknown form of energy that permeates all of space referred to as dark energy. Current observations show that dark energy is uniform in space and time producing a similar effect to that of the cosmological constant in the Einstein field equations of general relativity. Not much else is known about dark energy, although there are many experiments attempting to discover additional properties. The work in this thesis shall focus on trying to explain dark matter.

Dark matter cannot be explained by the 17 particles of the Standard Model, yet its gravitational effects have been observed in many circumstances. The rest of this chapter will cover the astrophysical evidence for dark matter (Sections 2.1 and 2.2),

various dark matter candidates (Section 2.3) and the models investigated at the LHC (Section 2.4), and non-collider searches for dark matter (Section 2.5).

## 2.1 Astrophysical Evidence

All existing evidence for dark matter comes from astrophysical observations of its gravitational effects on the universe at various length scales. We shall focus on four different sources of evidence: the average velocity of galaxies in clusters, the rotation curves of spiral galaxies, strong gravitational lensing, and merging galactic clusters. The evidence presented here is not exhaustive, see Reference [31] for more detail.

### 2.1.1 Galactic Clusters

Galactic clusters are the largest gravitational bound systems, with the orbital velocities of the individual clusters determined by the total gravitational mass of the cluster. Applying the Virial Theorem gives the explicit relation

$$v^2 = \frac{GM}{2r}, \quad (2.1)$$

where  $v$  is the average orbital velocity of a galaxy in the cluster,  $r$  is the average separation between galaxies in the cluster,  $M$  is the total gravitational mass of the cluster, and  $G$  is the Newtonian constant of gravitation. In 1933, Fritz Zwicky measured the average orbital velocity of the Coma cluster and using Equation 2.1 calculated that its mass was a factor of ten larger than the observed visible mass, leading to the conclusion that the majority of the cluster consisted of non-luminous matter [32]. Today studies show that stars only contribute 1% of the total cluster mass, with a hot, baryonic intracluster medium and dark matter contributing the remaining 14% and 85% of the total cluster mass, respectively [31].

### 2.1.2 Galactic Rotation Curves

Spiral galaxies are stable gravitational bound systems with stars and interstellar gas rotating around the galactic center in nearly circular orbits in a single plane. For these galaxies, the orbit of an individual star is stable when the gravitational force acting on the star balances the centripetal acceleration of the star. With this condition, the expected stellar velocity  $v$  is a function of distance  $r$  from the galactic center given by

$$v = \sqrt{\frac{GM(r)}{r}}, \quad (2.2)$$

where  $M(r)$  is the total gravitational mass inside radius  $r$ . Thus, past a certain critical radius  $r_c$ , the stellar velocity should fall with as  $r^{1/2}$  as the mass of the galaxy is no longer increasing significantly [33].

In 1980, Vera Rubin and Kent Ford observed that instead of decreasing at distances outside the visible galaxy, the stellar velocity stayed constant out to a very great distance, necessitating an additional non-luminous source of mass [34]. The most common explanation for this missing mass is the existence of an isotropic dark matter halo surrounding the galaxy. With the inclusion of interstellar gas, the total mass inside radius  $r$  is given by

$$M(r) = 4\pi \int_0^r dr' (r')^2 [\rho_S(r') + \rho_g(r') + \rho_{DM}(r')], \quad (2.3)$$

where  $\rho_S$ ,  $\rho_g$ , and  $\rho_{DM}$  are the density profiles of the stars, interstellar gas, and dark matter in the galaxy, respectively. Once these densities have been specified, it is possible to plot the fraction of the total stellar velocity due to each mass source as a function of distance from the galactic center. Figure 2-1 shows the results of doing this using the observed stellar and interstellar mass density profiles and the expected density from an isotropic dark matter halo for two different spiral galaxies. In both cases, this reproduces the observed flat galactic rotation curve incredibly well, lending strong support for the existence of galactic dark matter halos.

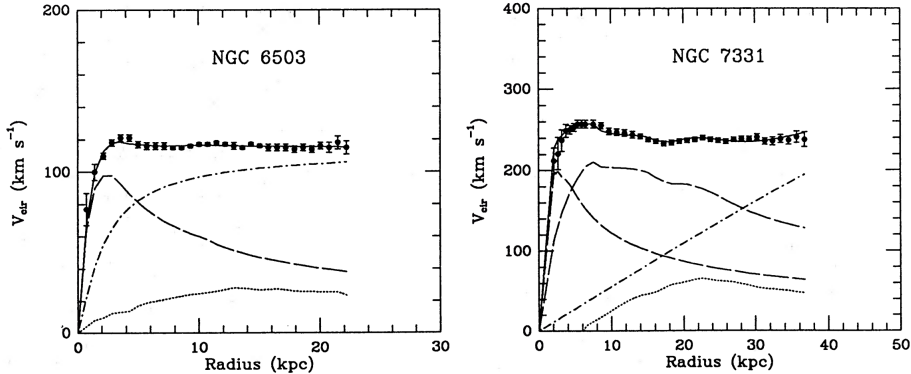


Figure 2-1: The observed (points) and fitted (solid line) rotation curves for two sample galaxies. The fit consists of three components: the stellar component (dashed), the interstellar gas (dotted), and the dark matter halo (dash-dotted). Reprinted from Reference [35].

### 2.1.3 Gravitational Lensing

As a consequence of Einstein's equivalence principle, a massive body will deflect light, a phenomenon known as gravitational lensing. In the language of general relativity, this means that the photons take the path given by the geodesic lines following the curvature of space-time due to the massive body. For most observations of gravitational lensing due to astrophysical bodies, the physical size of the lensing object is much smaller than the distance between observer, lens, and source allowing us to use the thin lens approximation. Approximating the lens as a planar distribution of matter, the angular deflection is given by

$$\vec{\alpha}(\vec{x}) = \frac{4G}{c^2} \int d^2x' \frac{\vec{x} - \vec{x}'}{|\vec{x} - \vec{x}'|^2} \int dz \rho(\vec{x}', z) \quad (2.4)$$

where  $\vec{x}$  is a two-dimensional vector in the plane of the lens,  $z$  is the perpendicular distance from the plane of the lens, and  $\rho$  is the three dimensional density [36]. If the source is treated as a point mass, this reduces to

$$\alpha = \frac{4G}{c^2} \cdot \frac{M}{b} \quad (2.5)$$

where  $b = |\vec{x} - \vec{x}'|$  is the impact parameter and  $M$  is the total mass of the object. Thus, measuring the angle of deflection due to gravitational lensing around an astrophysical object provides an independent measurement of the total mass of the body which can be compared to the mass of the luminous objects in the body.

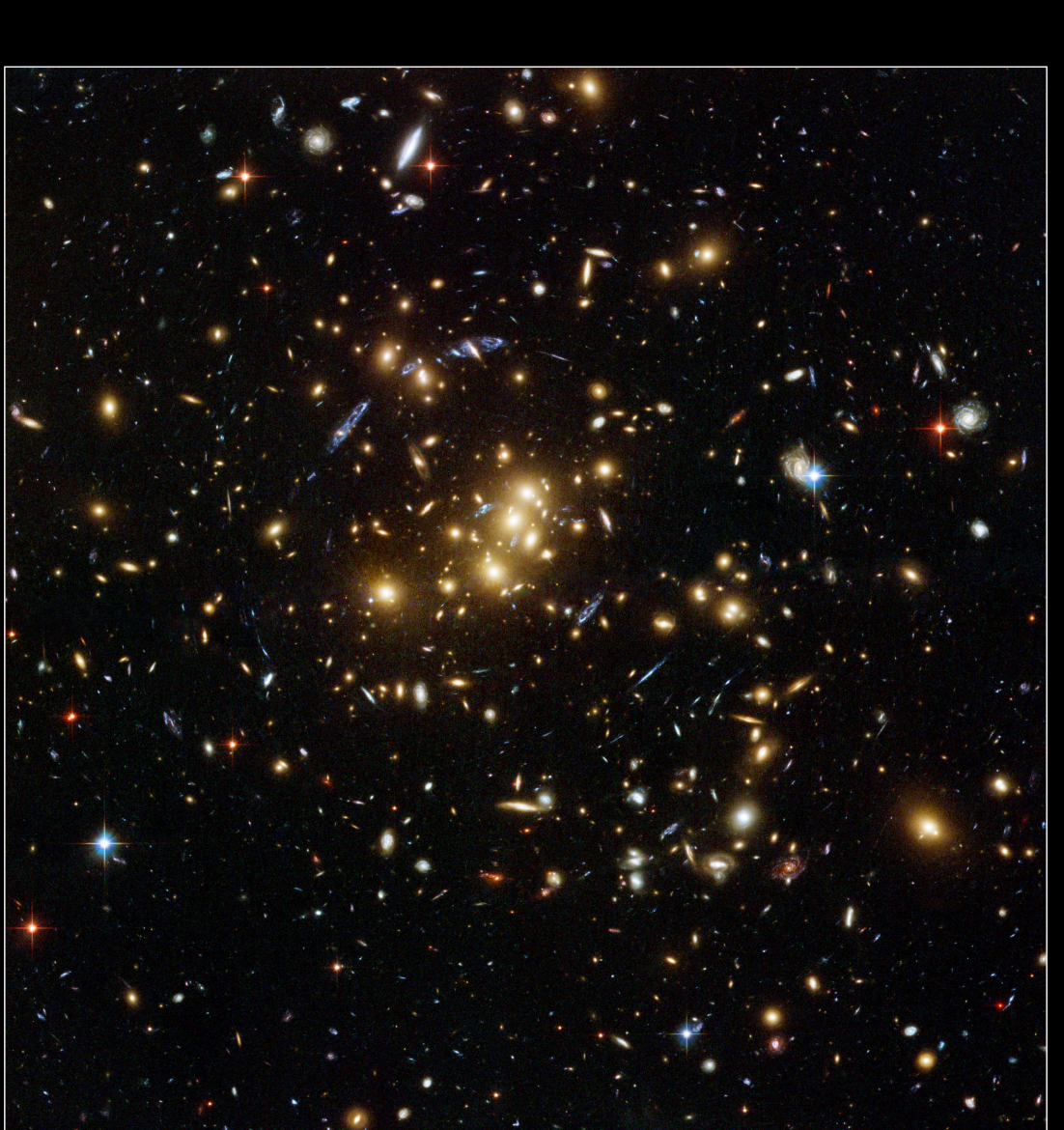
Depending on the mass of the deflecting body and impact parameter, the size of deflection can fall into three different regimes. The first of these is called strong lensing where the curving of space-time is so strong that light can travel multiple paths around the lens and still reach the observer. If the source is directly behind a circular lens, light travels around all sides of the lens and appears as an Einstein ring, while if the source is offset or the lens is non-circular, the source will instead appear in multiple locations as if viewed from slightly different angles. An example of strong lensing is shown in Figure 2-2.

The next regime is known as weak lensing, where the deflection is enough to distort the image of the source but not enough to result in multiple images. The shear of this distortion can be converted into a map of the projected mass distribution. True weak lensing results in circular “*E-mode*” patterns while sources of systematic uncertainty produce both “*E-mode*” and curl-like “*B-mode*” patterns. Thus, requiring a zero “*B-mode*” contribution assures that the measured mass distribution is accurate. Figure 2-3 shows the observed shear of half a million galaxies measured in the Hubble Space Telescope COSMOS survey.

The final regime is the microlensing that occurs when a lens moves relative to a luminous source. As the lens passes in front of the source, it will temporarily increase the apparent luminosity of the source, enabling a mass measurement of the lens. Microlensing results show that rocky exoplanets orbit other stars and that these planets cannot form the bulk of dark matter in the Milky Way.

#### 2.1.4 Cluster Collisions

Gravitational lensing measurements of galactic cluster collisions provide support for dark matter and help constrain its properties. Figure 2-4 shows the merging cluster 1E0657-558. By comparing the weak lensing reconstruction of the gravitational po-



**Galaxy Cluster Cl 0024+17 (ZwCl 0024+1652)**  
*Hubble Space Telescope • ACS/WFC*

NASA, ESA, and M.J. Jee (Johns Hopkins University)

STScI-PRC07-17b

Figure 2-2: Strong gravitational lensing around galaxy cluster CL0024+17, consisting of the gravitationally bound yellow, elliptical galaxies. The elongated blue objects are from much more distant galaxies behind the cluster which are distorted into arcs due to gravitational lensing from the dark matter halo surrounding the cluster. Figure credit: NASA, ESA, M.J. Jee and H. Ford (Johns Hopkins University)

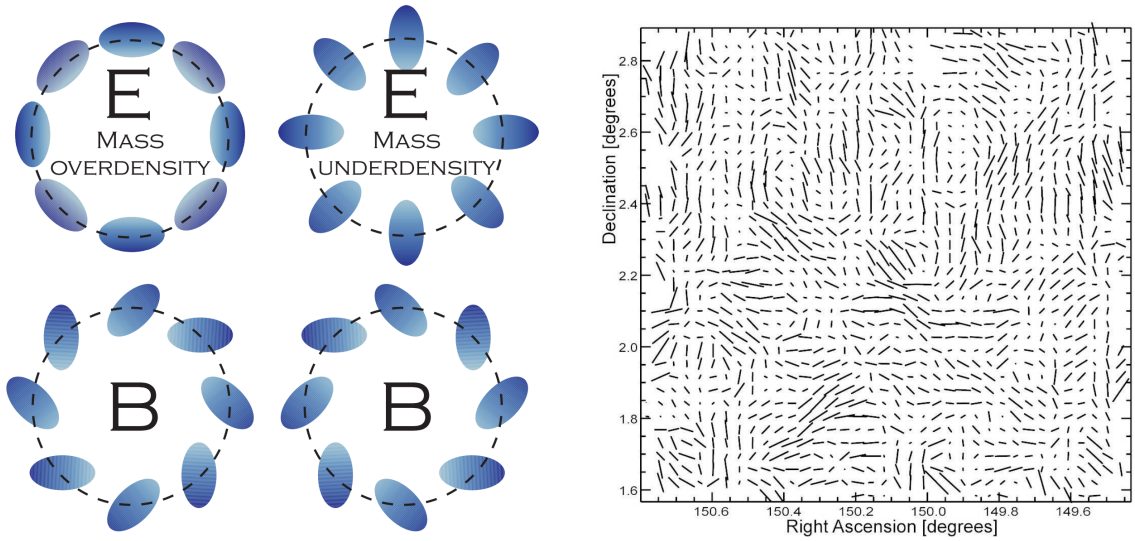


Figure 2-3: Left: Examples of circular “E-mode” and curl-like “B-mode” patterns. Right: The observed ellipticities of half a million distant galaxies within the 2 square degree Hubble Space Telescope COSMOS survey. Reprinted fom Reference [36].

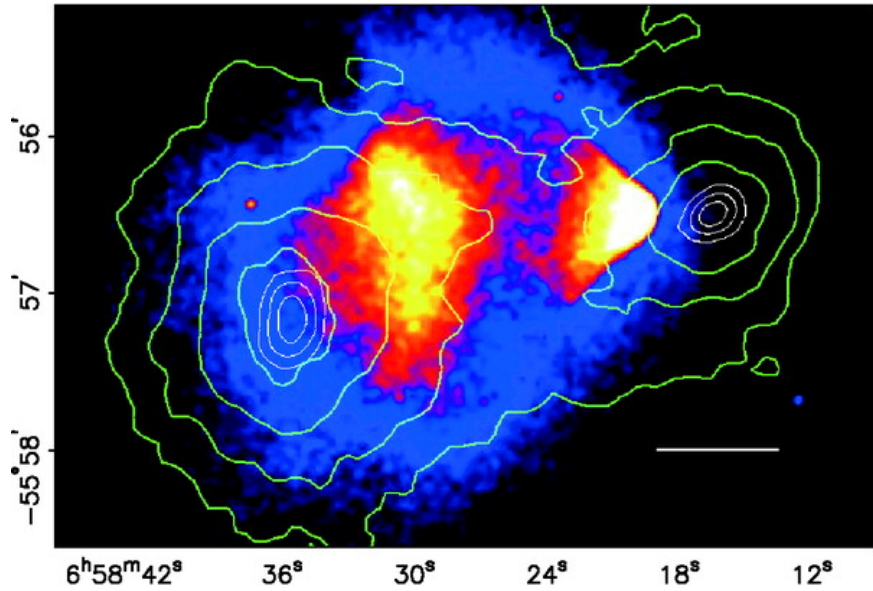


Figure 2-4: The merging cluster 1E0657-558. The green contours show the weak lensing reconstruction of the gravitational potential of the cluster. The colors indicate the X-ray temperature of the plasma, changing from blue to white as the plasma goes from coolest to hottest. The smaller “bullet” cluster on the right which traversed through the larger cluster on the left. Reprinted from Reference [37].

tential of the cluster shown in green contours against temperature color gradient of the X-ray emitting interstellar plasma, it was learned that the gravitational potential of the cluster does not track the dominant baryonic mass contribution coming from the plasma. Instead, the gravitational potential tracks the smaller stellar baryonic mass component. Dark matter must be the dominant gravitational source in the cluster since the center of total mass is offset from the center of baryonic mass. Furthermore, the observation of two gravitational mass centers places strong constraints on the self-interaction of dark matter requiring that the observed mass must have a self-interaction collisional cross section  $\sigma/m < 1.25 \text{ cm}^2 \text{g}^{-1}$  at a 68% confidence level [37].

## 2.2 Relic Density

During the early universe, dark matter (DM) was in thermal equilibrium with the rest of the SM particles with a number density  $n_\chi$  given by

$$n_\chi^{\text{eq}} = \frac{g}{(2\pi)^3} \int f(\vec{p}) d^3\vec{p}, \quad (2.6)$$

where  $g$  is the number of internal degrees of freedom of the DM particle  $\chi$  and  $f(\vec{p})$  is either the Fermi-Dirac or Bose-Einstein distribution, depending on the quantum statistics of the DM particle [38]. At very high temperatures relative to the mass  $m_\chi$  of the DM particle, dark matter and SM particles rapidly convert back and forth with a DM annihilation rate  $\Gamma = \langle \sigma_A v \rangle \cdot n_\chi$ , where  $\langle \sigma_A v \rangle$  is the thermally averaged product of the total cross section for annihilation  $\sigma_A$  and the relative velocity  $v$  of the dark matter particles. After the temperature drops below  $m_\chi$ , the DM annihilation rate  $\Gamma$  drops below the Hubble expansion rate  $H$  of the universe and the DM particles stop annihilating and freeze-out of equilibrium with the SM particles, leaving the DM relic density that we observe today. During the freeze-out process, the time dependence

of the number density  $n_\chi$  is described by the Boltzmann equation [38] as follows

$$\frac{dn_\chi}{dt} + 3Hn_\chi = -\langle\sigma_A v\rangle [(n_\chi)^2 - (n_\chi^{\text{eq}})^2]. \quad (2.7)$$

The term on the left-hand side accounts for the reduction in density due to the expansion of the universe. The two terms on the right-hand side account for the change in density due to annihilation and product of DM particles to and from SM particles, respectively.

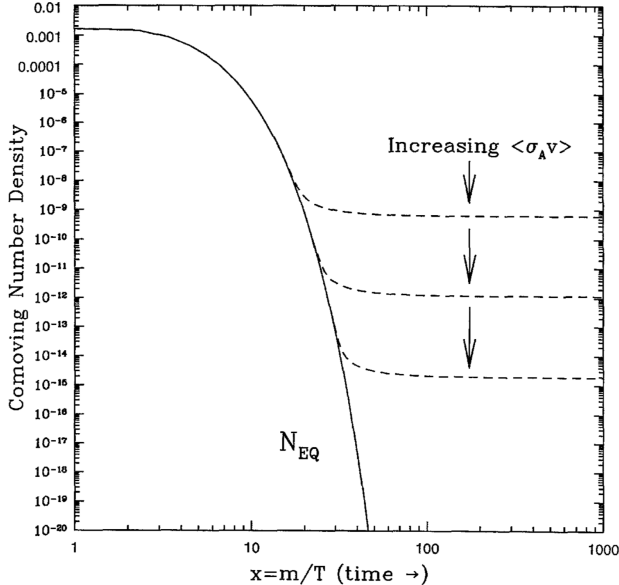


Figure 2-5: Number density of dark matter in the early universe as a function of time. The solid curves are the equilibrium abundance while the dashed curves are the actual abundance after freeze-out. Reprinted from Reference [38].

Figure 2-5 shows the calculated DM number density  $n_\chi$  as a function of time in the early universe. As the annihilation cross section increases, the relic density decreases as the dark matter particles stay in equilibrium longer. Assuming that  $\langle\sigma_A v\rangle$  is independent of energy, an order-of-magnitude estimate of the relic density is given by

$$\Omega_\chi \cdot h^2 = \frac{m_\chi n_\chi}{\rho_c} \simeq \frac{10^{-27} \text{ cm}^3 \text{ s}^{-1}}{\langle\sigma_A v\rangle}, \quad (2.8)$$

where  $h = H_0/(100 \text{ km s}^{-1} \text{ Mpc}^{-1})$  is the reduced Hubble constant and  $\rho_c = 3H^2/(8\pi G)$

is the critical density of the universe [38]. Thus, to first order the DM relic density depends only on two things: the total DM annihilation cross section  $\sigma_A$  and the mass  $m_\chi$  of the DM candidate, as after freeze-out  $T \ll m_\chi$  and the velocity  $v$  is strictly proportional to  $m_\chi$ . The latest Planck results measure that  $\Omega_\chi \cdot h^2 = 0.1200 \pm 0.0012$  [39], providing strong constraints on the possible values of  $\sigma_A$  and  $m_\chi$ .

## 2.3 Dark Matter Candidates

Dark matter has not been directly observed so far. In the previous sections, we collected all known facts about dark matter to restrict the pool of potential candidates. Any serious dark matter candidate must satisfy the following criteria:

- No or extremely weak interactions with photons, e.g. be **dark**
- Weak baryonic interactions to preserve the DM halos
- Weak self-interactions
- The observed relic density

These four criteria place stringent requirements on dark matter candidates. The light neutrinos, the only SM particles satisfying the first three conditions, are excluded as the total neutrino relic density has a bound of  $\Omega_\nu \cdot h^2 \leq 0.00067$  at 95% confidence level from analysis of the CMB anisotropies. Big Bang Nucleosynthesis and gravitational microlensing have mostly exclude non-luminous baryonic matter from forming the bulk of dark matter. Thus, most theories of dark matter propose a new fundamental particle as a dark matter candidate. The following sections discuss the most common dark matter candidates, namely weakly-interacting massive particles (WIMPs), axions, and sterile neutrinos.

### 2.3.1 Weakly-Interacting Massive Particles

The annihilation cross-section of new particle  $\chi$  with electroweak scale interactions is approximately

$$\langle \sigma_A v \rangle \approx \left( \frac{\alpha \cdot g_\chi^2}{m_\chi} \right)^2 = \left( \frac{e^2}{4\pi} \cdot \frac{(0.8)^2}{100 \text{ GeV}} \right)^2 \simeq 10^{-26} \text{ cm}^3 \text{ s}^{-1}, \quad (2.9)$$

where  $\alpha = e^2/4\pi$  is the fine-structure constant,  $m_\chi = 100 \text{ GeV}$  is the mass of the particle, and  $g_\chi \approx 0.8$  is the effective coupling for the four-point interaction  $\chi\bar{\chi} \rightarrow f\bar{f}$ . Plugging this into Equation 2.8, we obtain  $\Omega_\chi \cdot h^2 \sim 0.1$ , which is very close to the observed value. This numerical coincidence, known as the “WIMP miracle”, motivates a new weakly-interacting massive particle (WIMP) as a good DM candidate [38].

The only criteria to be a WIMP beyond the generic definition of dark matter is that the mass and interaction strength of the new particle must be approximately that of the EWK scale. Thus, a great many new physics models have WIMPs natively, such as the neutralino in supersymmetry and the lightest Kaluza-Klein particle in theories of universal extra dimensions. In this thesis, we shall focus on a set of simplified models that describe WIMP interactions in a relatively model-independent manner so that our results can be reinterpreted in as many theories as possible.

### 2.3.2 Axions

The hypothetical axion particle introduced in Section 1.1 is a dark matter candidate if the axion decay constant  $f_a$  is large enough as all axion-SM couplings are inversely proportional to it. Constraints from the observed duration of the neutrino burst from supernova SN 1987A require that  $f_a \gtrsim 10^9 \text{ GeV}$  [40], sufficiently high that the axion lifetime exceeds the age of the universe by many orders of magnitude. Thus, the axion is a viable DM candidate due to its long lifetime and weak couplings to SM particles.

After accounting for kinematic mixing with the  $\pi^0$  and  $\eta$  mesons, the axion mass is given by

$$m_a = \left( \frac{\sqrt{m_u m_d}}{m_u + m_d} \right) \left( \frac{f_\pi}{f_a} \right) m_\pi \simeq \left( \frac{10^7 \text{ GeV}}{f_a} \right) \text{ eV}, \quad (2.10)$$

where  $f_\pi$  is the pion decay constant and  $m_u$ ,  $m_d$ , and  $m_\pi$  are the masses of the up quark, the down quark, and the neutral pion, respectively. From this, we see that the axion mass is inversely proportional to  $f_a$ , leading to an upper limit of  $m_a \lesssim 10 \text{ meV}$ . The Planck measurements of the cosmic microwave background also provide a lower (upper) bound on the axion mass  $m_a \gtrsim 10 \mu\text{eV}$  (axion decay constant  $f_a \lesssim 10^{12} \text{ GeV}$ ), otherwise the axion abundance is too high.

The axion obtains a two-photon vertex through loops involving virtual quarks and gluons of the form

$$\mathcal{L}_{a\gamma\gamma} = \frac{1}{4} g_{a\gamma\gamma} \epsilon_{\mu\nu\rho\sigma} F^{\mu\nu} F^{\rho\sigma} a = -g_{a\gamma\gamma} (\vec{E} \cdot \vec{B}) a, \quad (2.11)$$

where  $F^{\mu\nu}$  is the electromagnetic field-strength tensor,  $\vec{E}$  and  $\vec{B}$  are the electric and magnetic fields, respectively, and the coupling constant is

$$g_{a\gamma\gamma} = -\frac{\alpha}{3\pi f_a} \left( \frac{m_u + 4m_d}{m_u + m_d} \right). \quad (2.12)$$

From this, we can see that the axion's coupling to the photon is incredibly small unless in the presence of a strong electromagnetic field. Thus, astrophysical axions are **dark** unless they enter a region with such a field. Searches for axions such as CAST[41] and ADMX[42, 43] exploit this to try to observe axion-to-photon conversions.

### 2.3.3 Sterile Neutrinos

In Section 1.5, we introduced mass for the SM fermions through the Higgs mechanism in order to preserve  $SU(2)_L$  gauge invariance. However, since the right-handed neutrinos are singlets under the full  $SU(3)_C \times SU(2)_L \times U(1)_Y$  gauge of the SM, it is possible to add explicit Majorana mass terms in addition to the Dirac mass terms in

the SM Lagrangian [44] as follows

$$\begin{aligned}
\mathcal{L}_{\nu_R} &= i\bar{\nu}_R \not{\partial} \nu_R - (\bar{\ell}_L Y_\nu \phi_c \nu_R + \bar{\nu}_R Y_\nu^\dagger \phi_c^\dagger \ell_L) - \frac{1}{2} \left( \bar{\nu}_R^c M_M \nu_R + \bar{\nu}_R M_M^\dagger \nu_R^c \right) \\
&= i\bar{\nu}_R \not{\partial} \nu_R - (\bar{\nu}_L M_\nu \nu_R + \bar{\nu}_R M_\nu^\dagger \nu_L) - \frac{1}{2} \left( \bar{\nu}_R^c M_M \nu_R + \bar{\nu}_R M_M^\dagger \nu_R^c \right) \\
&= i\bar{\nu}_R \not{\partial} \nu_R - \frac{1}{2} \left[ \begin{pmatrix} \bar{\nu}_L & \bar{\nu}_R^c \end{pmatrix} \begin{pmatrix} 0 & M_\nu \\ M_\nu^T & M_M \end{pmatrix} \begin{pmatrix} \nu_L^c \\ \nu_R \end{pmatrix} + h.c. \right], \tag{2.13}
\end{aligned}$$

where  $\nu_R^c$  are the charge conjugates of the right-handed neutrinos,  $h.c.$  stands for hermitian conjugate, and  $Y_\nu$ ,  $M_\nu$ , and  $M_M$  are the Yukawa, Dirac mass, and Majorana mass matrices for the neutrinos, respectively.

In the limit  $M_M \gg M_\nu$ , the combined mass matrix has two distinct sets of eigenvalues: the sterile neutrinos  $\nu_s$  with masses  $m_s \simeq M_M$  and the active neutrinos  $\nu_a$  with masses  $m_a \simeq M_\nu^2/M_M$ . The active and sterile neutrinos are related to the left- and right-handed neutrinos by the active-sterile mixing matrix  $\theta = M_\nu M_M^{-1}$  as follows

$$\begin{aligned}
|\nu_a\rangle &= \cos \theta |\nu_L\rangle + \sin \theta |\nu_R\rangle \\
|\nu_s\rangle &= -\sin \theta |\nu_L\rangle + \cos \theta |\nu_R\rangle. \tag{2.14}
\end{aligned}$$

In this formulation, the active neutrinos are the observed neutrinos of the SM while the sterile neutrino states are a promising dark matter candidate as they only interact with the SM through neutrino oscillations. Furthermore, the sterile neutrinos must have  $m_s \simeq$  keV or else they cannot account for the observed masses of DM-dominated objects without violating the Pauli exclusion principle [45]. Fortunately, this constraint also means that the oscillation rate into active neutrinos is low enough that the sterile neutrino lifetime is longer than the age of the universe. The Majorana mass term also allows for additional CP-violating phases beyond the Dirac phases. Astrophysical detection, accelerator production, and neutrinoless double  $\beta$  decay experiments all place constraints on sterile neutrino properties [46].

## 2.4 Simplified Models for LHC

Without loss of generality, we assume that dark matter consists of a single Dirac fermion WIMP species  $\chi$  with mass  $m_{\text{DM}}$  [47]. We are able to do this because collider searches are only minimally sensitive to the details of the dark matter candidate. Instead, collider searches are mainly sensitive to a new mediator particle with mass  $M_{\text{med}}$  that connects the dark sector to the Standard Model through couplings  $g_q$  and  $g_{\text{DM}}$  to the SM quarks and  $\chi$ , respectively. In general, this mediator can have any spin structure; for purposes of simplicity, we limit ourselves to the observed mediators in the SM: a spin-0 scalar  $S$ , a spin-0 pseudoscalar  $P$ , a spin-1 vector  $V_\mu$ , and a spin-1 axial-vector  $A_\mu$  (not to be confused with SM photon) [48]. The Lagrangians for these possible mediators are

$$\mathcal{L}_S = \frac{1}{2} M_{\text{med}}^2 S^2 + g_{\text{DM}} \bar{\chi} S \chi + g_q \sum_q \bar{q} Y_q S q \quad (2.15)$$

$$\mathcal{L}_P = \frac{1}{2} M_{\text{med}}^2 P^2 + g_{\text{DM}} \bar{\chi} \gamma^5 P \chi + i g_q \sum_q \bar{q} Y_q \gamma^5 P q \quad (2.16)$$

$$\mathcal{L}_V = \frac{1}{2} M_{\text{med}}^2 V_\mu V^\mu + g_{\text{DM}} \bar{\chi} \not{V} \chi + g_q \sum_q \bar{q} \not{V} q \quad (2.17)$$

$$\mathcal{L}_A = \frac{1}{2} M_{\text{med}}^2 A_\mu A^\mu + g_{\text{DM}} \bar{\chi} \gamma^5 \not{A} \chi + g_q \sum_q \bar{q} \gamma^5 \not{A} q, \quad (2.18)$$

where  $\{q\}$  and  $\{Y_q\}$  are the SM quarks and their associated Yukawa couplings and we have assumed that the coupling  $g_q$  is universal to all quarks without any loss of generality. The width of the mediators is determined by the coupling constants and mass of the mediator. Thus, these four models are described by only four parameters in addition to the spin structure of their couplings:  $\{g_q, g_{\text{DM}}, m_{\text{DM}}, M_{\text{med}}\}$ . For the results shown in this thesis, we fix  $g_q = 0.25$  and  $g_{\text{DM}} = 1$  to satisfy the narrow width approximation, provide complementarity to dijet and dilepton searches for new mediators, and enable easy comparison between other dark matter searches from ATLAS and CMS. Meanwhile, we scan the mass parameters  $m_{\text{DM}}$  and  $M_{\text{med}}$  between 1-1000 GeV and 10-2000 GeV, respectively [47].

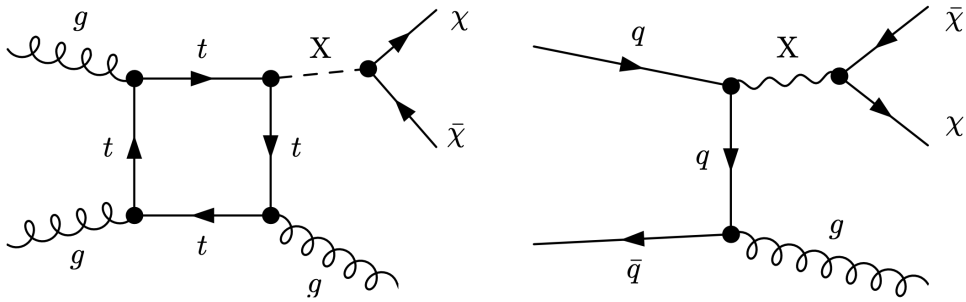


Figure 2-6: Feynmann diagrams for possible dark matter production modes at the LHC, with  $X$  denoting the mediator and  $\chi$  the dark matter particle. The left diagram is most common for scalar and pseudoscalar mediators, while the right diagram is most common for vector and axial mediators. For the right diagram, the gluon can be replaced with any of the EWK gauge boson whereas for the left diagram, other production modes dominate for the EWK gauge bosons. Reprinted from Reference [48].

As the CMS detector is focused on observing particles through electromagnetic and strong interactions, the production of DM particles alone does not result in an observable signature in the detector. Instead, we look for events where they are produced in association with a visible SM particle with the resulting signature of the SM particle recoiling against an invisible state. The standard mechanism for producing this final state is for one of the incoming partons to radiate the visible SM particle, usually a quark or a gauge boson, as shown in Figure 2-6. The possible final states split into the categories shown in Table 2.1 with unique final states and interaction strengths.

Name	Strength	Final State
Monojet	$\mathcal{O}(\alpha_s)$	$j + \chi\bar{\chi}$
Monophoton	$\mathcal{O}(\alpha)$	$\gamma + \chi\bar{\chi}$
Mono- $Z$	$\mathcal{O}(\alpha)/M_Z^2$	$\ell\ell + \chi\bar{\chi}$

Table 2.1: Final states of DM production with approximate interaction strength.

The monojet final state has the highest production rate but also the largest amount of background from SM processes. The Mono- $Z$  final state is the cleanest signature but also ahhs a substantially suppressed production rate due to the mass of the  $Z$  boson and the small branching ratio to leptons. The monophoton final state lands in the

middle on both metrics: the production rate is  $\sim 1/10$  that of the monojet final state but also has fewer backgrounds from SM processes. Additionally, the monophoton state has the “advantage” of being able to distinguish between the spin-0 and spin-1 mediators by the “virtue” of the  $gg \rightarrow S\gamma$  and  $gg \rightarrow P\gamma$  processes being forbidden by Furry’s theorem [49].

## 2.5 Non-collider Searches

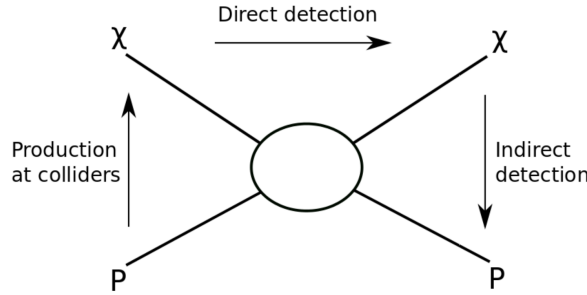


Figure 2-7: Possible dark matter detection channels. Reprinted from Reference [50].

The goal of a collider-based search for dark matter is to create pairs of DM candidates through quark-antiquark annihilation, i.e.  $q\bar{q} \rightarrow \chi\bar{\chi}$ . However, there are other ways you can look at this interaction when attempting to find dark matter, as shown in Figure 2-7. The longest running searches for DM particles have been direct detection searches, where one attempts to observe the scattering of a DM particle off of a heavy nucleus, i.e.  $q\chi \rightarrow q\chi$ . Another method involves the inverse process utilized at hadron colliders, the observation of SM particles produced in the annihilation of astrophysical DM pairs, i.e.  $\chi\bar{\chi} \rightarrow q\bar{q}$ . In this section, we shall give a brief overview of the leading experiments for these two approaches.

### 2.5.1 Direct Detection

Direct detection experiments aim to observe a collision between a DM particle  $\chi$  and an atomic nucleus  $N$ . Current experiments target nuclear recoils in the  $1 - 100$  keV

range and there are various different technologies that are used to identify the recoiling nucleus, as shown in Figure 2-8. The three main signals are light from a scintillating material, charge from an ionization reaction, and phonons from thermal excitations [50]. Many detectors utilize multiple signals in order to enhance background rejection.

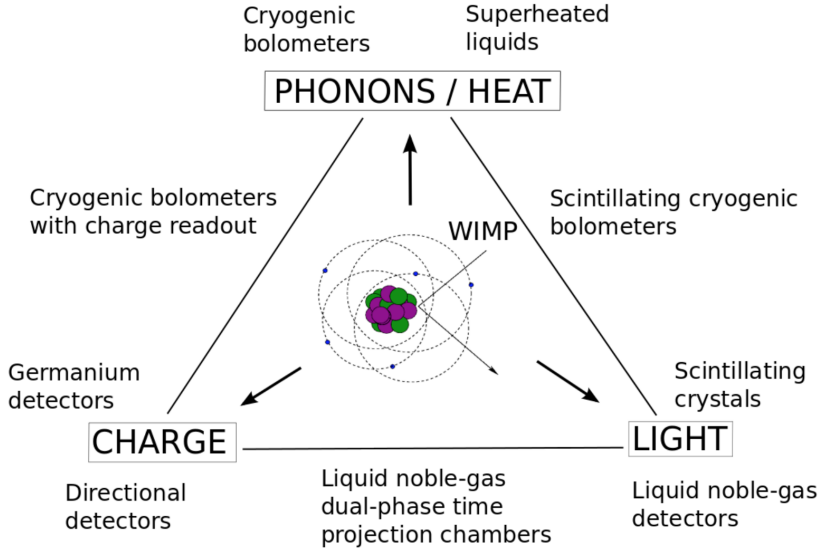


Figure 2-8: Possible signals measured and technologies used in direct detection experiments. Reprinted from Reference [50].

Another consideration is whether the interaction is spin-independent (SI) or spin-dependent (SD), corresponding to a vector/scalar or axial/pseudoscalar mediator, respectively. The SI DM-nucleus cross-section scales as the number of nucleons squared and thus experiments focusing on SI interactions use materials with a large atomic number. Conversely, the spin-dependent DM-nucleus cross-section depends on the total nuclear spin and experiments focusing on SD interactions use materials with an odd number of nucleons, particularly those with unpaired protons and neutrons. The remainder of this section will discuss three proto-typical direct detection experiments.

The Large Underground Xenon (LUX) experiment [51] is a dual-phase xenon time projection chamber that utilizes both scintillation light and free electrons from ionization to detect nuclear recoils. The active detector volume has 250 kg of ultrapure

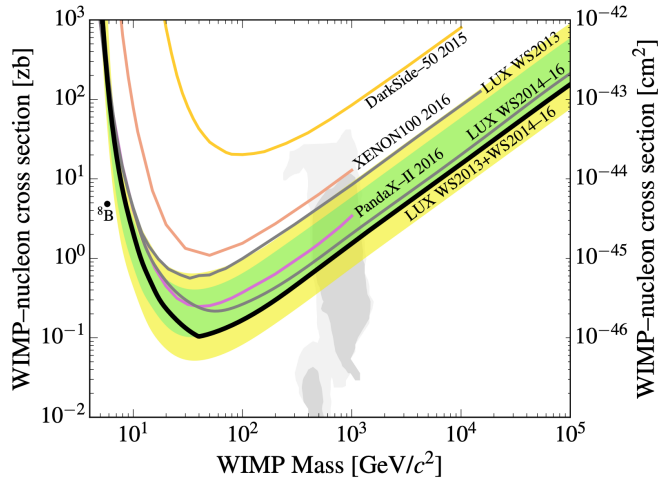


Figure 2-9: Latest SI independent results from the LUX experiment (brazilian flag bands). Reprinted from Reference [51].

liquid xenon, a large enough volume that the detector is self-shielding. Measurements of spin-dependent interactions are possible with an effective volume of approximately half the active detector because odd isotopes make up 47% of naturally occurring xenon, The latest LUX results are shown in Figure 2-9.

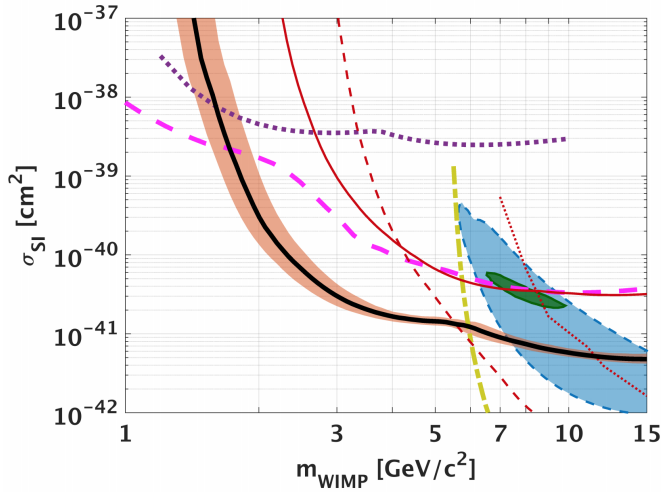


Figure 2-10: Latest SI independent results from the CDMSlite experiment (black line with salmon-colored band). Reprinted from Reference [52].

The CDMSlite experiment [52] uses a cryogenic germanium bolometer that detects phonons and ionization from nuclear recoils. The presence of both signals allows for

particle identification, but the most sensitive results only use the phonon signals. CDMSlite is most sensitive to dark matter with masses between 1-10 GeV as shown in Figure 2-10.

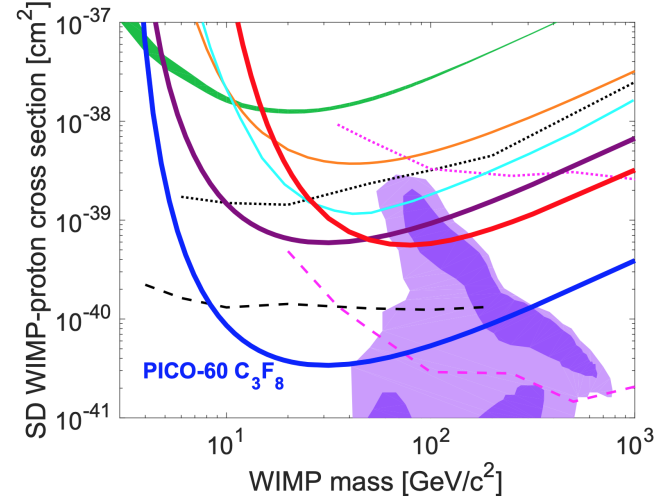


Figure 2-11: Latest SD independent results from the PICO-60 experiment (thick blue line). Reprinted from Reference [53].

The PICO-60 experiment [53] uses a bubble chamber filled with  $\text{C}_3\text{F}_8$  to observe nuclear recoils with a threshold of 13.6 keV. This threshold is high enough to reject backgrounds from minimum ionizing particles while still having sufficient signal efficiency. Flourine has exactly one unpaired proton and no unpaired neutrons which greatly enhances the sensitivity to the proton-coupling SD interactions. The latest results from PICO-60 are shown in Figure 2-11.

### 2.5.2 Indirect Detection

We discussed the process of dark matter annihilation in the early universe and found that the relic density  $\Omega_\chi \cdot h^2$  depended on the average annihilation cross section  $\langle \sigma_A v \rangle$ . We found that a 100 GeV WIMP particle must have  $\langle \sigma_A v \rangle \sim 10^{-26} \text{ cm}^3 \text{ s}^{-1}$  in order to produce the observed relic density. While our calculation assumed that the DM number density did not change appreciably after freezeout, there is still a non-zero annihilation rate of  $n_\chi^2 \langle \sigma_A v \rangle / 2$  for dark matter to SM particles. With this decay rate and the observed relic density, there should be  $\mathcal{O}(10)$  particles from DM annihilation

reaching Earth per year per square meter [54]. Thus, it is possible to learn about dark matter by observing the particle flux near Earth.

While dark matter can decay to a pair of any SM particles, the only ones that live long enough to reach Earth are photons, neutrinos, electrons, positrons, protons, and anti-protons, whether produced directly or from decays of short-lived particles. While it is possible to measure the flux of all of these particles, it is only possible to observe the energy spectrum and source locations of photons and neutrinos because galactic magnetic fields obscure these for the charge particles. Thus, experiments such as the Alpha Magnetic Spectrometer (AMS-02) [55] look for a rise in the positron and anti-proton fractions of the cosmic ray flux to find signs of WIMP annihilation. Similarly, gamma ray telescopes such as the Fermi Large Area Telescope (Fermi-LAT) [56] search for high-energy photons originating from dwarf spheroidal galaxies as they have especially high ratios of dark matter to luminous matter. Both experiments have tentative signals that are yet to be confirmed.

The neutrino channel differs from the other two because it is the only channel sensitive to the annihilation of WIMPs that have been gravitationally captured by the sun because only neutrinos escape the sun with their original energy spectrum intact [57]. Since solar WIMPs are in equilibrium, the annihilation flux depends only on the DM-nucleon cross-section instead of the annihilation cross-section, and since the sun consists primarily of hydrogen, observations of neutrinos from solar WIMPs are especially sensitive to spin-dependent processes. Thus, because astrophysical uncertainties are very small for neutrinos originating from the sun versus galactic sources, results from solar neutrino observatories are competitive with those from direct detection experiments.

The IceCube neutrino observatory [58] is a Cherenkov light detector consisting of a cubic kilometer of Antarctic ice instrumented with 79 strings of photomultiplier tubes. Figure 2-12 shows the latest results from IceCube, with each curves assuming annihilation into a different SM particle pair.

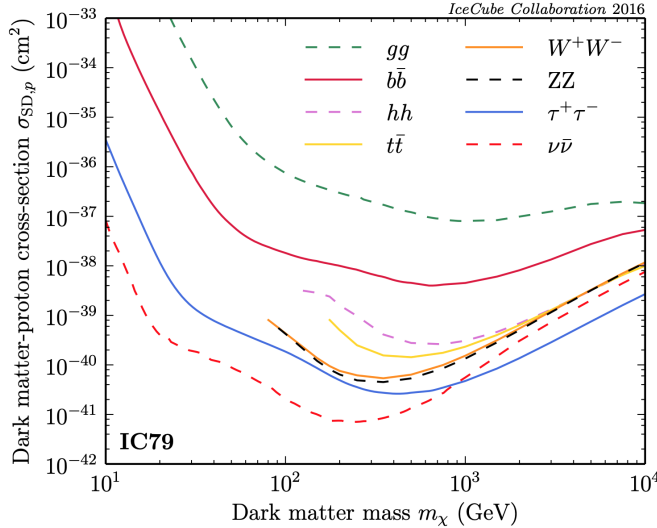


Figure 2-12: Latest SD independent results from the IceCube experiment. Reprinted from Reference [58].

## 2.6 Summary

Copious astrophysical evidence exists for a non-relativistic non-baryonic type of matter referred to as dark matter that constitutes  $\sim 27\%$  of the energy of the universe. An attractive candidate for dark matter is a new beyond the Standard Model particle that has weak interactions with photons, baryons, and itself and a relic density of  $\Omega_\chi \cdot h^2 = 0.1200 \pm 0.0012$ . While other candidates exist, a new weakly-interacting massive particle is a dark matter candidate found in many theories of new physics. Collider, direct detection, and indirect detection searches can all be interpreted in the context of simplified models, which feature a new Dirac fermion DM particle and a massive mediator. The remainder of this thesis focuses on a search for dark matter produced in conjunction with a single photon at the Large Hadron Collider using the Compact Muon Solenoid detector.



# Chapter 3

## The Large Hadron Collider

### 3.1 Experimental Apparatus

The Large Hadron Collider (LHC) is a circular proton-proton collider, 27 km in circumference and between 40 and 175 m below the surface, located at the European Organization for Nuclear Research (CERN) on the French-Swiss border near the city of Geneva [59]. Designed to collide protons at a maximum center-of-mass energy  $\sqrt{s} = 14$  TeV, the LHC has delivered collisions at  $\sqrt{s} = 7, 8$  TeV during Run 1 (2010-2012) and at  $\sqrt{s} = 13$  TeV during Run 2 (2015-2018). While the LHC is primarily a proton-proton collider, lead (Pb) ion beams of energy of up to 2.8 TeV per nucleon are used to produce lead-lead and proton-lead collisions. In this thesis, we focus exclusively on data recorded from proton-proton collisions during Run 2.

The LHC is the final stage of the CERN accelerator complex [60] depicted in Figure 3-1. Hydrogen atoms are stripped of their electrons and accelerated to an energy of 50 MeV by the LINAC2 linear acceleration. Following this, they are injected into the Booster ring, the Proton Synchrotron (PS), and the Super Proton Synchrotron (SPS) and accelerated to 1.4, 26, and 450 GeV, respectively. After the SPS, the protons are injected into the two counter-circulating rings of the LHC in up to 2808 discrete bunches with a bunch spacing of 25 ns. The two beams intersect in eight places along the LHC with detector experiments CMS, ATLAS, LHCb, and ALICE each located at an intersection point.

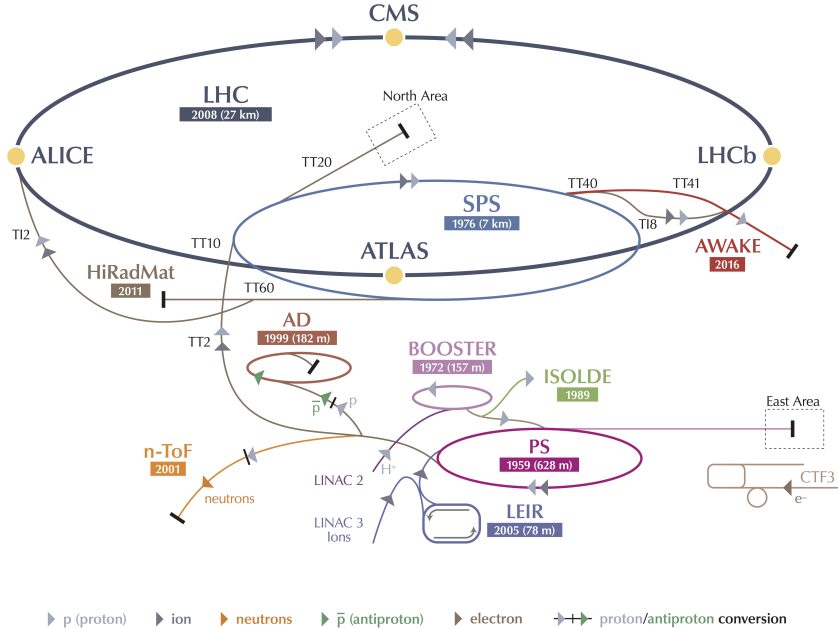


Figure 3-1: A schematic representation of the CERN accelerator complex. The LHC (dark blue) is fed protons by a chain of intermediate accelerators, beginning with LINAC2 (light pink). Reprinted from the CERN Document Server [61].

The LHC is a synchrotron containing 1232 superconducting NbTi dipole magnets measuring 15 m in length, each with a peak dipole field of 8.33 T. There are an additional 492 quadrupole magnets measuring 5-7 m in length which focus the beams in between the dipole magnets. Due to space limitations in the tunnels, the beam pipes are magnetically coupled and the magnets share the same superfluid liquid helium cryostatic system required to achieve the 1.9 K temperature required to achieve the desired magnetic field strength and cool sufficient amount of power out of the system.

The number of events produced at the LHC is given by

$$N(pp \rightarrow X) = \int dt L(t) \sigma(pp \rightarrow X), \quad (3.1)$$

where  $\sigma$  is the cross section of the process and  $L$  is the instantaneous luminosity of

the machine given by

$$L = \frac{N_b^2 n_b f_{\text{rev}} \gamma}{4\pi \epsilon \beta^*} \times F, \quad (3.2)$$

where  $N_b$  is the number of particles per bunch ( $\mathcal{O}(10^{11})$ ),  $n_b$  is the number of bunches per beam,  $f_{\text{rev}}$  is frequency of revolution,  $\gamma$  is the Lorentz factor of the beam,  $\epsilon$  is transverse emittance of the beam,  $\beta^*$  is beta function of the beam at the collision point, and  $F$  is the geometric luminosity reduction factor due to the crossing angle at the interaction point. The instantaneous luminosity decreases exponentially as a function of time due to  $N_b$  and  $n_b$  being reduced by collisions. The LHC is designed to deliver an initial instantaneous luminosity of  $\mathcal{O}(10^{34}) \text{ cm}^{-2} \text{ s}^{-1}$ , achieved by having multiple inelastic proton-proton interactions per bunch crossing known as pileup.

As all known cross sections are time-independent, the total number of events is directly proportional to the integrated luminosity given by

$$L_{\text{int}} = \int_0^T dt L(t) = L(0) \tau_L (1 - e^{-T/\tau_L}), \quad (3.3)$$

where  $T$  is the time since starting collisions,  $L(0)$  is the initial instantaneous luminosity, and  $\tau_L \approx 15 \text{ h}$  the characteristic beam loss timescale for the LHC. The total luminosity delivered by the LHC and recorded by CMS during the 2016 is shown in Figure 3-2.

## 3.2 Collider Phenomenology

The proton is a composite particle consisting of valence quarks, sea quarks, and gluons, collectively referred to as partons. When colliding protons at the LHC, we are actually interested in the inelastic scattering of a pair of partons from the incident protons. Each parton  $a, b$  carries a fraction of the momentum of the incoming proton  $x_{a,b}$  following the particle-dependent parton distribution functions (PDFs)  $f_{a,b}$ . The differential cross section for  $2 \rightarrow N$  parton scattering process [63] is given by

$$d\sigma(ab \rightarrow \{c_i\}) = \frac{(2\pi)^4}{2s} \left( \prod_i \frac{d^3 p_i}{(2\pi)^3} \right) \cdot \delta^4 \left( k_a + k_b - \sum_i p_i \right) \cdot |\mathcal{M}(ab \rightarrow \{c_i\})|^2 \quad (3.4)$$

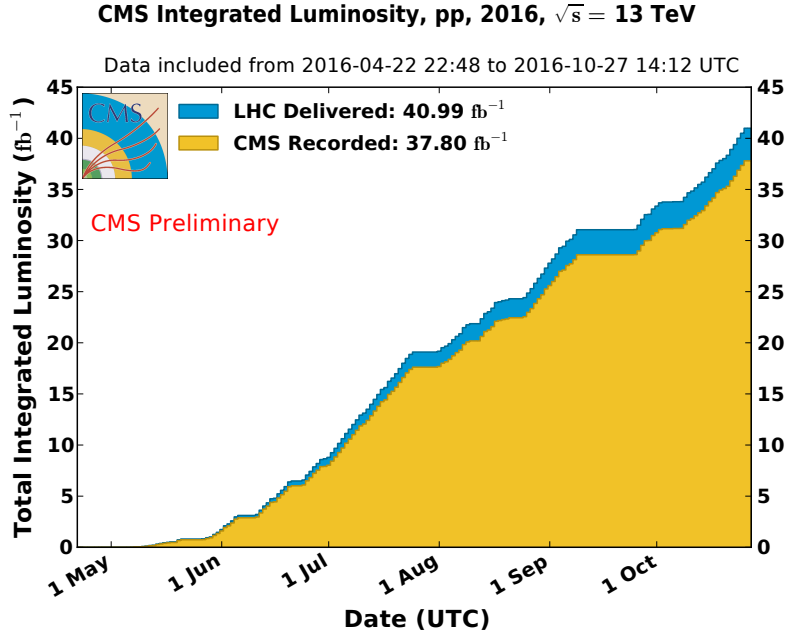


Figure 3-2: The total integrated luminosity of the LHC during proton-proton collisions during 2016 [62]. While a total luminosity of  $41 \text{ fb}^{-1}$  was collected, only a subset during which the detector operated well enough is used in this thesis. This corresponds to  $36 \text{ fb}^{-1}$  of data.

where  $k_{a,b} = x_{a,b}\sqrt{s}$  are the momenta of the incoming partons,  $\{p_i\}$  are the momenta of the outgoing partons  $\{c_i\}$ , and  $\mathcal{M}$  is the matrix element of the process.

This parton level scattering, called the hard scattering process, is perturbatively calculable through standard QFT methods. However, the hard scattering does not include any effects related to the PDFs of the incoming partons or the decay and hadronization of the outgoing partons into the final state particles (called the parton shower), both of which involve non-perturbative aspects of QCD. Fortunately, the collinear factorization theorem [64] states that the probability of obtaining the final state  $X(\Theta)$  from a hadron collision can be calculated as the product of the probability that specific partons  $a, b$  are involved in the interaction, the probability for the hard scattering to produce outgoing partons  $\{c_i\}$ , and the formation of final state hadrons from these outgoing partons. The factorization process is not unique and requires the choice of an arbitrary energy scale  $\mu_F$ , which defines a lower bound for interactions to be considered part of the hard scattering.

Including the effects from PDFs and parton showering (PS), the general cross section for  $pp \rightarrow X(\Theta)$  is

$$\begin{aligned} \frac{d\sigma}{d\Theta}(pp \rightarrow X(\Theta)) &= \sum_{a,b} \int dx_a f_a(x_a, \mu_F) \cdot dx_b f_b(x_b, \mu_F) \\ &\times d\sigma(ab \rightarrow \{c_i\}) \times D(\{c_i\} \rightarrow X(\Theta)), \end{aligned} \quad (3.5)$$

where the sum is over the initial state partons and  $D$  is the fragmentation function that describes parton shower process resulting in the observed final state. The following sections discuss the simulation of the three main elements of Equation 3.5: the parton distribution functions  $f_a$ , the hard scattering cross section  $d\sigma$ , and the parton shower and hadronization processes that contribute to the fragmentation function  $D$ .

### 3.2.1 Parton Distribution Functions

Due to soft collinear emissions from the partons, the behavior of the parton distribution functions depends on the factorization scale. Denoting the gluon PDF as  $g(x, \mu_F)$  and the PDF for quark flavor  $i$  as  $q_i(x, \mu_F)$ , the analytic behavior of the PDFs is given by the DGLAP [65–67] evolution equations

$$\mu_F \frac{d}{d\mu_F} \begin{pmatrix} q_i(x, \mu_F) \\ g(x, \mu_F) \end{pmatrix} = \frac{\alpha_s}{2\pi} \int_x^1 \frac{dy}{y} \begin{pmatrix} P_{qq}(x/y) & P_{qg}(x/y) \\ P_{gq}(x/y) & P_{gg}(x/y) \end{pmatrix} \begin{pmatrix} q_i(y, \mu_F) \\ g(y, \mu_F) \end{pmatrix} \quad (3.6)$$

where  $y$  is the fraction of momentum carried by initial parton and the  $P$  matrix elements are the splitting kernels defined by

$$\left. \begin{array}{l} P_{qq}(z) = \frac{4}{3} \left( \frac{1+z^2}{1-z} \right) \\ P_{gq}(z) = \frac{1}{2} (z^2 + (1+z)^2) \end{array} \right| \left. \begin{array}{l} P_{qg}(z) = \frac{4}{3} \left( \frac{1+(1-z)^2}{z} \right) \\ P_{gg}(z) = 6 \left( \frac{1-z}{z} + \frac{z}{1-z} + z(1-z) \right). \end{array} \right. \quad (3.7)$$

The DGLAP equations cannot be solved analytically at a fixed scale. Instead, parameterized functional forms are fitted to data from many experiments. The results

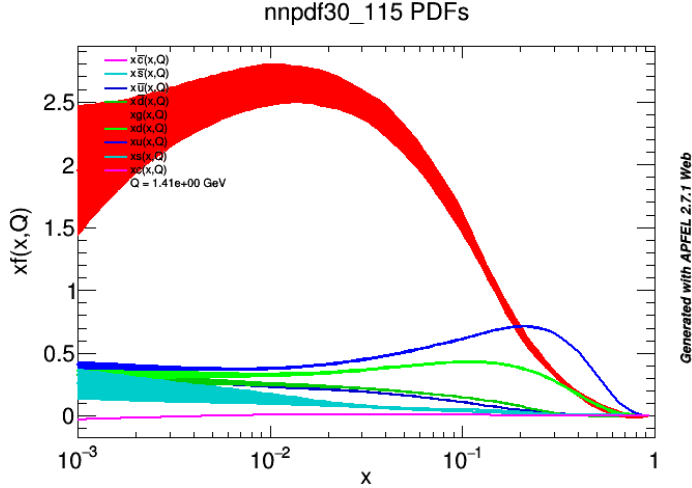


Figure 3-3: The various quark and gluon PDFs for the proton, as a function of momentum fraction  $x$ . The specific PDF set is the NNPDF3.0 118 NLO PDF set.

presented in this thesis use the NNPDF3.0 PDF set provided by the NNPDF collaboration [68]. Figure 3-3 shows the quark and gluon PDFs for the proton. As  $x \rightarrow 0$ , the gluon fraction dominates while near  $x \approx 0.3$ , the up-quark fraction  $u(x, \mu_F)$  approaches  $\frac{2}{3}$ , the down-quark fraction  $d(x, \mu_F)$  approaches  $\frac{1}{3}$ , and the gluon and sea quark fractions approach zero.

### 3.2.2 Hard Scattering

The hard scattering process is simulated using Monte Carlo generators that sample events with probability proportional to the phase space and matrix element. For the results contained in this thesis, the primary hard interaction is simulated using the MADGRAPH5 aMC@NLO generator [69, 70], which can simulate to leading order (LO) in EW vertices and up to next-to-leading order (NLO) in QCD vertices.

### 3.2.3 Parton Shower

The parton shower is a sequence of splittings where one outgoing parton  $c_i$  emits a second soft and/or collinear particle  $j$  [71]. Each splitting has an associated splitting kernel  $P_{c_i \rightarrow c_i j}(z)$ , where  $z$  is the momentum fraction carried by the initial parton. The allowed QCD splittings are  $q \rightarrow qg$ ,  $g \rightarrow q\bar{q}$ , and  $g \rightarrow gg$  and the allowed QED

splittings are  $f \rightarrow f\gamma$  and  $\gamma \rightarrow f\bar{f}$ . The kernels associated with these splittings are

$$\left. \begin{array}{l} P_{q \rightarrow qg}(z) = \frac{4}{3} \left( \frac{1+z^2}{1-z} \right) \\ P_{g \rightarrow q\bar{q}}(z) = \frac{1}{2} (z^2 + (1-z)^2) \\ P_{g \rightarrow gg}(z) = 3 \left( \frac{(1-z)(1-z)^2}{z(1-z)} \right) \end{array} \right| \begin{array}{l} P_{f \rightarrow f\gamma}(z) = Q_f^2 \left( \frac{1+z^2}{1-z} \right) \\ P_{\gamma \rightarrow f\bar{f}}(z) = N_C Q_f^2 (z^2 + (1-z)^2) \end{array} \quad (3.8)$$

where  $Q_f$  is the charge of the fermion and  $N_C$  is the number of color states the fermion can occupy (3 for quarks and 1 for leptons). The cross section of a splitting is given by

$$\frac{d\sigma(ab \rightarrow \{c_i\}j)}{d\sigma(ab \rightarrow \{c_i\})} = P_{c_i \rightarrow c_ij}(z) \cdot \frac{\alpha_s}{2\pi} \cdot \frac{d\theta}{\theta} \cdot dz \quad (3.9)$$

where  $\theta$  is the opening angle between  $c_i$  and  $j$ . These cross sections diverge as  $\theta \rightarrow 0$  and  $z \rightarrow 1$ , meaning bare quarks producing many soft and collinear gluons. Then, these gluons further split to  $gg$  and  $q\bar{q}$  pairs, which in turn emit even more soft and collinear gluons and photons. This process continues until the energy of the outgoing partons reaches  $\Lambda_{\text{QCD}}$  at which point hadronization occurs. The final state particles from the shower of a single parton are often collimated into a narrow cone that is reconstructed as a single physics object called a jet.

### 3.2.4 Hadronization

The QCD potential between two quarks can be approximated as  $V(\vec{r}) \approx \kappa r$ , where  $\kappa$  has been measured to be approximately 1 GeV/fm. The linear behavior of the potential is due to the attractive interactions between the gluons mediating the quark-quark interaction which confine the color field between the quarks into a tube 1 fm in diameter. As the quarks separate, the energy contained in this gluon tube increases linearly until it exceeds the mass of a  $q\bar{q}$  pair. At this point, a new  $q\bar{q}$  pair pops into existence through a quantum mechanical tunneling process, splitting the tube in two. Due to the difference in quark masses, only up, down, and strange quarks are produced, in a 10:10:3 ratio. This process continues until the energy of all the quarks have low enough energy to combine into stable hadrons.

The above procedure is a qualitative description of the Lund string model [72]. The Pythia event generator models hadronization using the Lund string model as well as the parton shower effects described in the previous section. All results in this thesis use the Pythia 8.2 program [71] to simulation the parton shower and hadronization processes.

# Chapter 4

## The CMS Detector

The Compact Muon Solenoid (CMS) detector [73] is one of two hermetic, general purpose detectors at the Large Hadron Collider. The primary motivation for the experiment was the discovery of the Higgs boson by observing its decays to photons, electrons, and muons. Towards this end, the detector was built to fulfill the following goals:

- Unambiguous charge identification of muons with momenta up to 1 TeV
- 1 GeV mass resolution on 100 GeV pairs of muons, electrons, and photons
- Efficient triggering and tagging of  $\tau$  lepton and  $b$  quark decays
- Good resolution on the hadronic energy and missing transverse energy
- Sufficient time resolution to deal with 40 MHz of collisions

The CMS detector consists of four main subdetectors: the inner trackers, the electromagnetic calorimeter (ECAL), the hadronic calorimeter (HCAL), and the muon chambers. The first three are within the field volume of the eponymous 3.8 T superconducting NbTi solenoid magnet while the muon chambers are embedded in the return yoke of the magnet. Additionally, there is an online triggering system to reduce readout by over four orders of magnitude from 40 MHz to  $\mathcal{O}(1)$  kHz for prompt reconstruction.

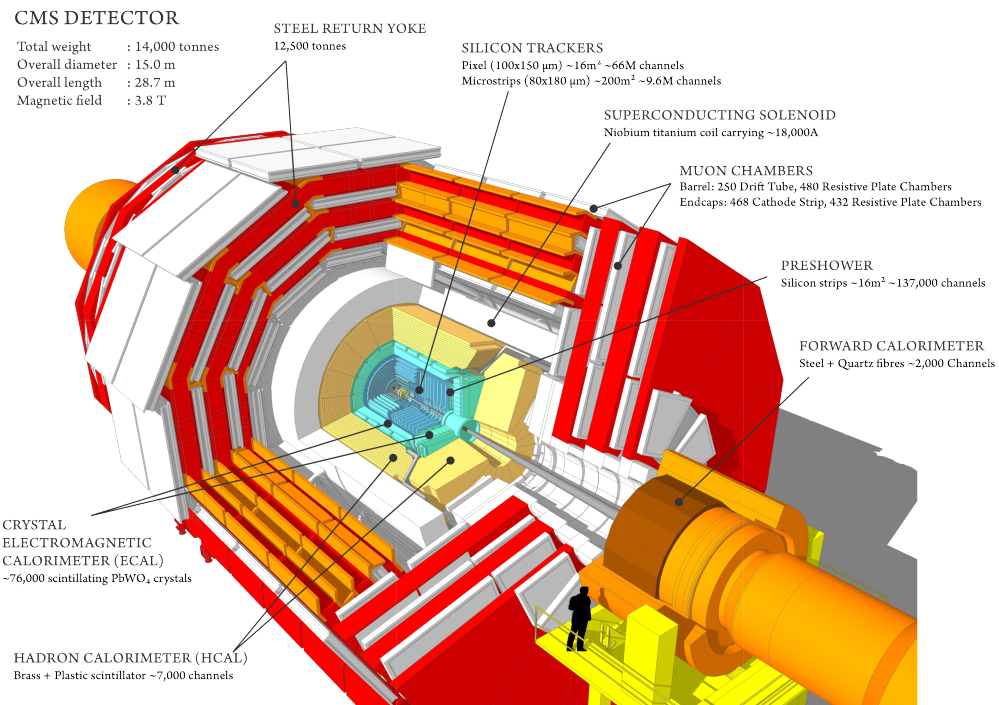


Figure 4-1: A cutaway view of the CMS detector. The labels identify the solenoid as well as the different subdetectors and their components. Reprinted from Reference [74].

The overall layout of the CMS detector is shown in Figure 4-1. The CMS detector has a cylindrical geometry with concentric barrel shaped detectors in the central region and disc shaped detectors in the forward region and a total weight of 12500 tons, a length of 22 m, and a diameter of 15 m. We define a right-handed cartesian coordinate system with the origin at the nominal center of the detector. The  $z$  coordinate is along the beam axis, with the positive  $z$ -axis pointing counter-clockwise as seen from the sky, and the  $x$  and  $y$  coordinates are perpendicular to it, with the positive  $x$ -axis pointing from the center of the detector to the center of the LHC ring and the positive  $y$ -axis pointing upwards. However, we more commonly use the following cylindrical coordinate system when working with the CMS detector:

- distance  $z$  along the beam axis
- distance  $r$  from the beam axis
- polar angle  $\theta$  measured with respects to the positive  $z$ -axis
- azimuthal angle  $\phi$  in the plane orthogonal to the beam axis with zero at the positive  $x$ -axis.

The four-momentum of a particle is  $p = (p_x, p_y, p_z, E)$  in the cartesian basis and a particle of mass  $m$  produced at rest in the center of the detector has  $p = (0, 0, 0, m)$ . While the momenta along the beam axis of the two incoming protons are equal, the momenta of the incoming partons involved in the hard scattering often are not as discussed in Section 3.2. Thus, we define two kinematic quantities that are Lorentz-invariant with respect to a boost along the beam axis: the tranverse momentum  $\vec{p}_T = p_x \hat{x} + p_y \hat{y}$  with magnitude  $p_T = \sqrt{p_x^2 + p_y^2}$  and the pseudorapidity  $\eta = -\ln \tan \theta/2$ .

In terms of  $p_T$ ,  $\eta$ , and  $\phi$ , we have the following expressions for our cartesian variables:  $p_x = p_T \cos \phi$ ,  $p_y = p_T \sin \phi$ ,  $p_z = p_T \sinh \eta$ , and  $E = p_T \cosh \eta$ , with the last equality assuming the mass of the particle is negligible compared to its momentum. In terms of our Lorentz-invariant coordinates, the four-momentum of a given particle is  $p = (p_T, \eta, \phi, E)$ . Additionally, the spatial separation of two particles is given by

$\Delta R = \sqrt{(\Delta\phi)^2 + (\Delta\eta)^2}$  and the fiducial acceptance of the CMS detector is from  $0 \leq \phi < 2\pi$  and  $-5 \leq \eta \leq 5$ .

## 4.1 Inner Trackers

Closest to the interaction point, the inner trackers identify charged particles and measures their momenta [73]. Additionally, high resolution tracks are used to identify primary and secondary vertices. The magnetic field in the tracker volume is uniform with strength 3.8 T and field lines parallel to the beam direction. The tracker volume extends to 1.2 m in  $r$  and 2.9 m in  $z$ , providing coverage for  $|\eta| < 2.5$ , and is instrumented with silicon pixels and strips. Each silicon sensor is a  $p$ - $n$  semiconductor junction with a bias voltage applied. When a charged particle passes through the depletion region of the junction, electron-hole pairs are produced and collected by the readout electronics. A schematic of the inner tracker system is shown in Figure 4-2.

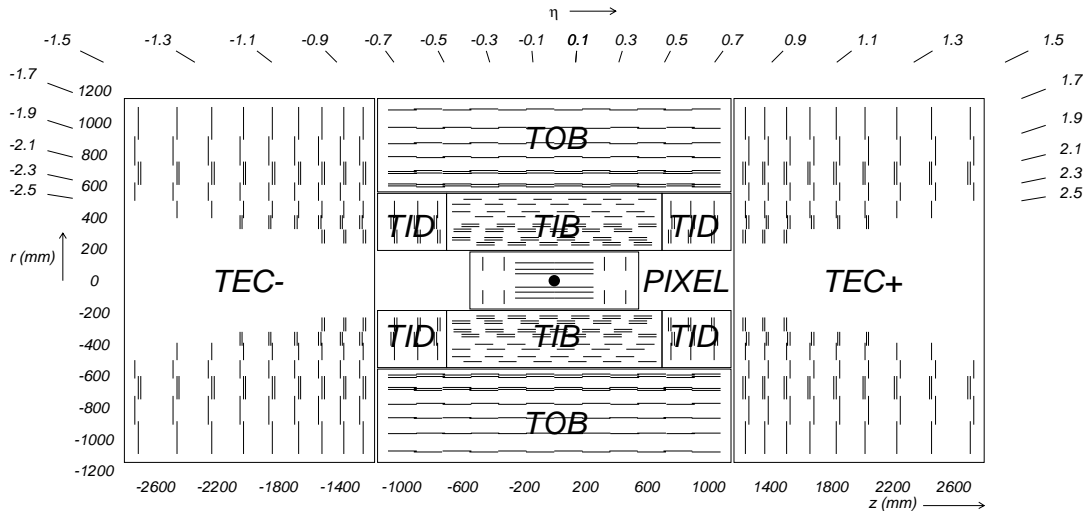


Figure 4-2: A schematic view of the CMS inner tracker system. Silicon pixel and strip detectors are shown. The volumes labeled TIB, TID, TOB, and TEC are all strip trackers. The double lines indicate back-to-back modules that deliver stereo hits. Reprinted from Reference [73].

The 66 million individual pixel sensors, each measuring  $285 \mu\text{m} \times 100 \mu\text{m} \times 150 \mu\text{m}$  in  $r \times r\phi \times z$ , are arranged into seven layers: three cylindrical barrels at  $r =$

4.4, 7.3, 10.2 cm and two bi-layer endcap annuli at  $z = \pm 34.5, \pm 46.5$  cm. Due to the geometry of the pixel detector, tracks typically cross the sensor at a  $20^\circ$  angle, leading to the charge deposit from a single track to be shared among multiple pixels in the same layer. The exact position of a particle in each layer is determined by interpolating the signals from multiple adjacent pixels with an analog pulse height greater than a tuneable read-out threshold. Thus, each pixel hit is localized to an area of  $\sim 15\text{ }\mu\text{m} \times 20\text{ }\mu\text{m}$  in  $r\phi \times z$ , providing a much higher spacial resolution than the raw pixel spacing.

The pixels are surrounded 9.3 million silicon strips measuring  $10\text{ cm} \times 80\text{ }\mu\text{m}$  arranged in ten cylindrical layers in the barrel and twelve disks in each endcap. The Tracker Inner Barrel (TIB) consists of the first four layers and extends from 20 cm to 55 cm in the radial direction while out six layers constitute the Tracker Outer Barrel (TOB) with an outer radius of 116 cm and extent in  $|z|$  of 118 cm. The remaining area in the barrel is covered by the Tracker Inner Disk (TID), consisting of the three disks located from 80 to 90 cm in  $|z|$ . The Tracker EndCaps (TEC) have nine disks each and cover the region  $124\text{ cm} < |z| < 282\text{ cm}$ .

The majority of the strips are oriented perpendicular to the  $\phi$  direction: parallel to the beam pipe in the barrel region and radially aligned in the endcap region. The strip pitch varies from 80 to  $184\text{ }\mu\text{m}$  with the smallest pitch in the innermost layer. This detector geometry provides good resolution in the  $r\text{-}\phi$  plane for barrel and the  $z\text{-}\phi$  plane for the endcap but little information on the orthogonal directions. To compensate for this, one third of the strips are double-layered with a stereo angle of 100 mrad between the layers. Matching hits between adjacent layers enables a measurement of the  $z$  and  $r$  coordinates in the barrel and endcap, respectively. The final spacial resolution is  $10\text{-}50\text{ }\mu\text{m}$  in the direction perpendicular to the strips and  $100\text{-}530\text{ }\mu\text{m}$  in the parallel direction on the stereo modules.

## 4.2 Electromagnetic Calorimeter

The electromagnetic calorimeter (ECAL) is a homogeneous, hermetic calorimeter composed of 76,000 lead tungstate ( $\text{PbWO}_4$ ) crystals [73]. High density ( $8.3 \text{ g/cm}^3$ ) lead tungstate was chosen due to its radiation hardness, fast scintillation decay time constant of 25 ns, small Moliere radius  $r_M = 21.9 \text{ mm}$ , and short radiation length  $X_0 = 8.9 \text{ mm}$ . All of these factors combine to enable the construction of a compact calorimeter with high granularity and excellent energy resolution.

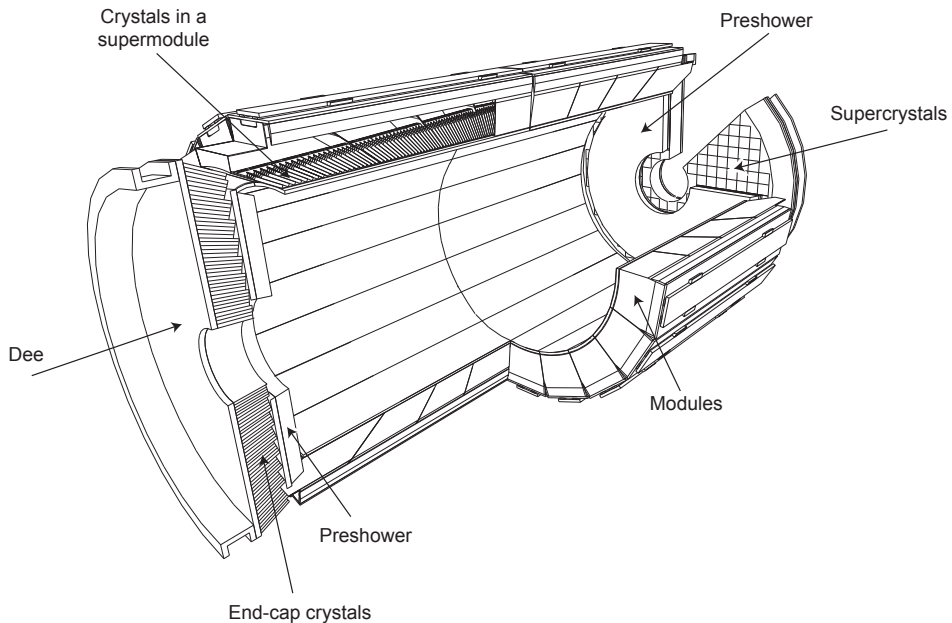


Figure 4-3: The layout of the CMS electromagnetic calorimeter. The barrel and endcap calorimeters are shown. The pre-shower detector sits in front of the endcaps. Reprinted from Reference [73].

Figure 4-3 shows the layout of the ECAL. The central barrel region (EB) has 61200 crystals arranged in a  $170 \times 360 \eta\phi$  grid ( $0.0174 \times 0.0174$  granularity) with a coverage up to  $|\eta| = 1.44$  while the two endcap annuli (EE) each have 7324 crystals organized in a  $x-y$  grid with coverage in the range  $1.479 < |\eta| < 3.0$ . Each crystal in the EB has a truncated pyramidal shape with a length of 230 mm, a 22 mm  $\times$  22 mm front-face cross-section, and a 26 mm  $\times$  26 mm rear-face cross-section while a crystal in the EE has a cuboid-like shape with a length of 220 mm, a 28.6 mm  $\times$  28.6 mm front-

face cross-section, and a  $30\text{ mm} \times 30\text{ mm}$  rear-face cross-section. The cross-sectional area of approximately one Moliere radius and length of approximately 25 radiation lengths allows just a few crystals to contain the entire transverse and longitudinal development of the shower. To reduce the likelihood of the primary photon or electron emerging from the hard scattering depositing most of its energy in passive material, the crystals do not point directly to the interaction region.

The interactions between the  $3.8\text{ T}$  magnetic field and the geometries of the ECAL lead to the selection of different photosensors in the barrel and endcaps. In the endcaps, the magnetic field is parallel to the path of the photoelectrons and has a negligible effect on the gain, while in the barrel, the magnetic field is perpendicular and reduces the gain by a factor proportional to the distance traveled by the photoelectrons. Thus, in the barrel, solid-state reverse-structure avalanche photodiodes (APDs) with a depletion layer of  $6.0 \pm 0.5\text{ }\mu\text{m}$  are used, while photomultiplier tubes with a single gain stage and a very fine copper mesh anode called vacuum phototriodes (VPTs) are used in the endcaps. Two APDs with an active area of  $25\text{ mm}^2$  are glued to the rear of each crystal in the barrel while only one VPT with an active area of  $280\text{ mm}^2$  is needed per crystal in the endcap. The APDs and VPTs amplify the initial signal of approximately 4.5 photoelectrons per MeV of energy deposit per crystal by a factor of 50 and 10, respectively.

The small signals from the photodetectors are shaped and amplified in the Multi-Gain Preamplifier (MGPA) and a 12-bit analog-to-digital converter (ADC) samples the pulse every 25 ns. Each output voltage pulse has a length of approximately 300 ns, with the maximum at approximately 75 ns and a slow decay afterwards. The MGPA has multiple gain modes of 12, 6, and 1, and the gain chosen for the output decreases once the signal has saturated the previous gain setting. After the pulse falls below the saturation threshold, the lower gain setting is maintained for the next five samples. This mechanism provides a dynamic signal range from a few MeV to a maximum of  $1.5\text{ TeV}$  in the barrel and  $3.1\text{ TeV}$  in the endcaps.

The energy resolution of the ECAL was measured using an electron beam to be

$$\frac{\sigma_E}{E} = \frac{2.8\%}{\sqrt{E/\text{GeV}}} \oplus \frac{12\%}{E/\text{GeV}} \oplus 0.3\%, \quad (4.1)$$

where  $E$  is the energy of the incident particle and the three terms on the RHS are the stochastic, noise, and constant terms, respectively. The stochastic term is dominated by event-to-event fluctuations in the lateral shower containment and a photo-statistics contribution of 2.1%. Electronic and digitization noise drive the noise term while the constant term comes from a non-uniform longitudinal light collection and intercalibration errors.

#### 4.2.1 Preshower Detector

At high momenta and high  $|\eta|$ , the two photons from a  $\pi^0$  decay can merge into a single ECAL crystal due to the large boost in the  $z$ -direction of the initial state. By forcing the initiation of an electromagnetic shower in a region with high spacial resolution in front of the ECAL endcaps, the preshower detector can differentiate between one- and two-photon deposits in the region  $1.6 < |\eta| < 2.5$ . The preshower detector consists of two alternating layers of passive lead absorbers and active silicon strip sensors. The first (second) lead layer is two (one) radiation lengths thick and the subsequent sensor plane has vertical (horizontal) strips of 6 cm length and 1.9 mm pitch. The silicon strips resolve the shower with a resolution of  $\mathcal{O}(1-10)$  mm, enabling the disambiguation of two nearly collinear photons and the identification of  $\pi^0$  decays.

### 4.3 Hadronic Calorimeter

The hadronic calorimeter (HCAL) is a set of four heterogenous calorimeters that provide hermetic coverage when combined [73]: the barrel calorimeter (HB) covering  $|\eta| < 1.3$ , the endcap calorimeter (HE) covering  $1.3 < |\eta| < 3$ , the outer calorimeter (HO) covering  $|\eta| < 1.3$ , and the forward calorimeter (HF) covering  $3 < |\eta| < 5$ . The region covering  $|\eta| < 3$  shall be referred to as the central HCAL. The granularity of

the HCAL in  $\eta\phi$  is  $0.087 \times 0.087$  for  $|\eta| < 1.6$ ,  $0.17 \times 0.17$  for  $1.6 < |\eta| < 3.0$ , and  $0.175 \times 0.175$  for  $3 < |\eta| < 5$ . The layout of the HCAL is shown in Figure 4-4.

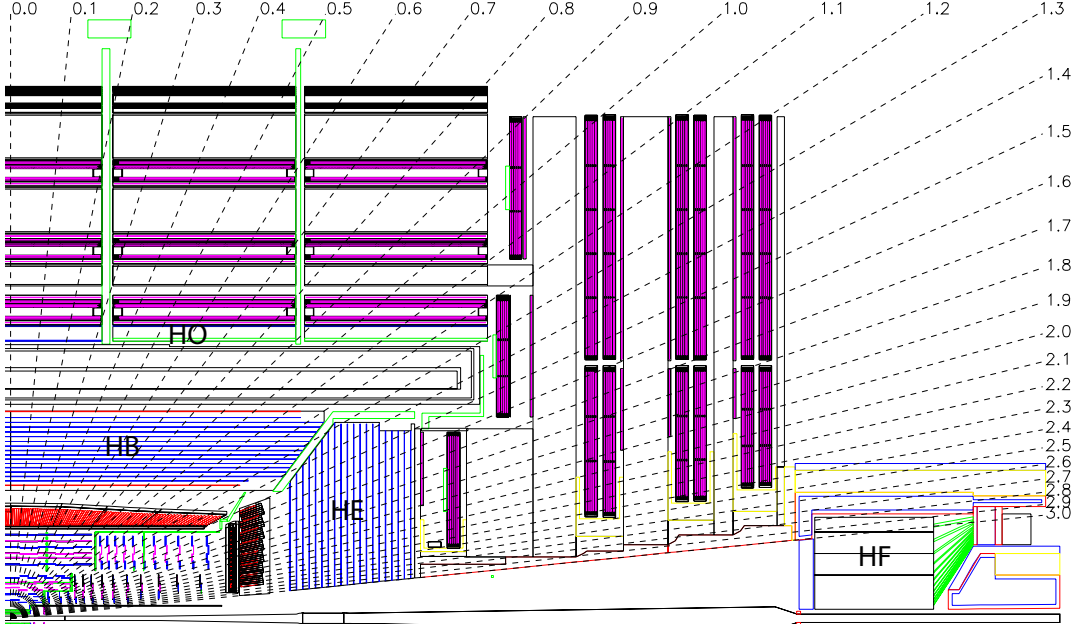


Figure 4-4: The layout of the CMS hadronic calorimeter. The barrel, endcap, outer, and forward calorimeters are shown and labeled. The muon chambers are shown but not labeled. The dashed lines denote different values of pseudorapidity. Reprinted from Reference [73].

The HB and HE are sampling calorimeters with 16 and 17 thin plastic scintillator layers, respectively, interleaved with thick absorber layers made of a non-magnetic brass alloy with an interaction length  $\lambda_I = 1.5$  cm. The layers range in thickness from 40 to 75 mm providing a total absorber depth ranging from a minimum of  $5.82\lambda_I$  at  $|\eta| = 0$  to a maximum of  $10.6\lambda_I$  at  $|\eta| = 1.3$  in the barrel and approximately nine interaction lengths throughout the endcaps, with the ECAL contributing another interaction length worth of material. The dimensions of the HB and HE are determined by the requirement that they reside between the ECAL and the solenoid. To circumvent this constraint, an additional layer of scintillator located in the return yoke of the magnet, the HO, utilizes the solenoid material as an additional interaction length of absorber. Hybrid photodiodes (HPDs) are used to read out the scintillator

light in the HB and HE while silicon photomultipliers (SiPMs) are used in the HO.

Located 11 meters from the interaction point, the HF is a sampling calorimeter covering the region of phase-space with high pseudorapidity. Since the particle flux here is much higher than in the central region, the HF uses radiation-hard steel absorber instrumented with two sets of scintillating quartz fibers. Charged particles produced by showers in the steel traverse the quartz fibers and emit Cherenkov radiation that is recorded by photomultiplier tubes. To distinguish hadrons from photons and electrons, the second set of fibers starts at a depth of 22 cm.

Since hadrons interact with the ECAL as well as the HCAL, the energy resolution of the detectors must be considered in tandem in the central region. Using a charged particle test beam, the combined ECAL+HCAL energy resolution was measured to be

$$\frac{\sigma_E}{E} = \frac{0.847}{\sqrt{E/\text{GeV}}} \oplus 0.074 \quad (4.2)$$

and the standalone HF energy resolution is

$$\frac{\sigma_E}{E} = \frac{1.98}{\sqrt{E/\text{GeV}}} \oplus 0.09. \quad (4.3)$$

## 4.4 Muon Chambers

The outer most components of CMS are the muon triggering, identification, and detection chambers [73]. These muon detectors are interleaved with the steel return yoke of the magnet resulting in a characteristic *S*-shape for the muon trajectories due to the reversal of magnetic field direction across the solenoid. Signal purity in the muon detectors is high as hadrons, electrons, and photons are stopped by the calorimeters while muons are minimum ionizing particles (MIPs) that lose little energy while traversing the detector. Taking advantage of the large detector volumes required by the outer solenoid radius of 3.5 m, three types of gas ionization chambers are used: drift tubes (DTs) in the barrel covering  $|\eta| < 1.2$ , cathode strip chambers (CSCs) in the endcaps coering  $0.9 < |\eta| < 2.4$ , and resistive plate chambers (RPCs) in both covering  $|\eta| < 2.1$ . The layout of the muon detectors is shown in Figure 4-5.

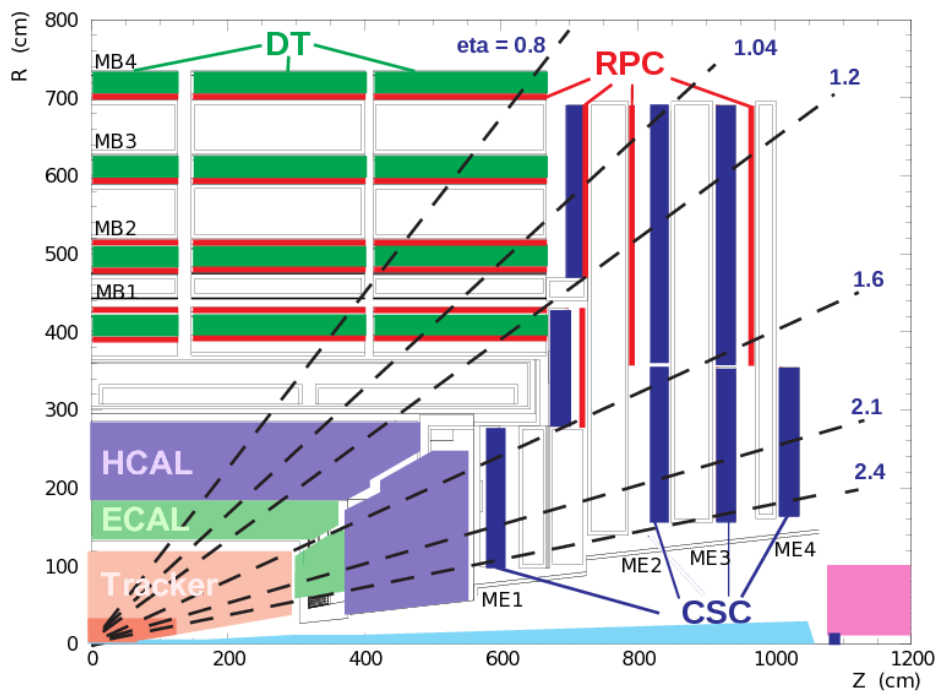


Figure 4-5: The layout of the CMS muon chambers. The four DT stations are labeled MB1-MB4, the four CSC stations are labeled ME1-ME4, and the RPC stations are shown in red. The dashed lines denote different values of pseudorapidity. Reprinted from Reference [73].

The DT chambers consist of rectangular drift cells with transverse dimensions of  $42\text{ mm} \times 13\text{ mm}$  filled with a 85:15 Ar/CO<sub>2</sub> mix and a gold/steel anode wire held at a voltage of 3.6 kV. The maximum drift time per cell of 400 ns provides a spatial resolution of approximately  $250\text{ }\mu\text{m}$ . A single chamber is made out of superlayers which are in turn made out of four individual cells for a combined resolution of  $100\text{ }\mu\text{m}$ . The chambers are arranged into four 2.4 m thick dodecagonal rings called the muon barrel stations. All four stations have two superlayers per chamber that measure position in the  $r\text{-}\phi$  plane while the chambers in the inner three stations have an additional superlayer that measures position in the  $r\text{-}z$  plane. Together, the four muon stations and iron yokes form a wheel with one between the solenoid and the first iron layer, two in between the yokes, and one outside. The outer barrel is composed of five wheels in total.

Due to their faster response time and better spatial resolution, CSCs are used to handle the higher muon and background fluxes in the endcap region. Each CSC is filled with a 50:40:10 CO<sub>2</sub>/Ar/CF<sub>4</sub> mix and instrumented with 80 cathode strips held at voltages of 2.9–3.6 kV relative to the gold-plated tungsten anode wires. The strips run radially outward to measure position in the  $r\text{-}\phi$  plane while the wires run perpendicular measure the  $\eta$  and beam-crossing time of the muons. The four muon stations in each endcap are made of CSCs arranged into annuli oriented perpendicular to the beam axis and interspersed between the flux return plates. The three inner stations have multiple annuli with smaller ones fitting inside the larger ones while the fourth station only has one close to the beamline.

An RPC is a parallel-plate double-gap chamber with a time resolution of one nanosecond and a poor spatial resolution. The RPCs are interspersed throughout the DT and CSCs to provide an independent muon trigger system that can identify the correct bunch crossing time.

## 4.5 Online Trigger System

To achieve an instantaneous luminosity of  $\mathcal{O}(10^{34}) \text{ cm}^{-2} \text{ s}^{-1}$ , the LHC has bunch crossings every 25 ns for a total data rate of 40 MHz, much higher than the 100 kHz readout rate for the detector and the  $\mathcal{O}(1)$  kHz data reconstruction and tape writing rates. Fortunately, uninteresting elastic scattering and QCD inelastic scattering events dominate the approximately  $100 \mu\text{b}$  total proton-proton cross-section at the LHC. Meanwhile, most new physics processes have a predicted on the order of picobarns or femtobarns and even the highest rate SM EWK cross-sections are  $\mathcal{O}(10)$  nb, so not every event needs to be readout, reconstructed, and written to tape.

A two-stage trigger system selects the events to keep for permanent storage and analysis [73]. The Level 1 hardware-based trigger (L1) selects interesting events based on incomplete detector information to reduce readout and computation times. Events selected by the L1 trigger are fully readout and passed to the high level software-based trigger (HLT) where the full event is reconstructed using the data acquisition system (DAQ), a computing farm with over 20k CPU cores. Events selected by the HLT are sent to the offline computing resources for full reconstruction followed by storage on disk and tape.

The L1 trigger uses field programmable gate arrays (FPGAs) and application specific integrated circuits (ASICs) to make decisions within  $4 \mu\text{s}$  of each collision. Each subdetector module has a hardware trigger that reconstructs objects called trigger primitives (TPs). In the two calorimeters, clustered energy deposits from each tower are sent to a regional calorimeter trigger (RCT) which correlates the information from adjacent towers and between the ECAL and HCAL into electron, photon, and jet candidates. The outputs from the RCT are passed to the global calorimeter trigger (GCT) which computes global event variables such as the total transverse energy, the hadronic transverse energy, and the momentum imbalance. Muon track candidates are produced from a simple segment-finding and tracking algorithm in each of the three types of muon chambers. The global muon trigger (GMT) receives the candidates and combines them with information from the GCT

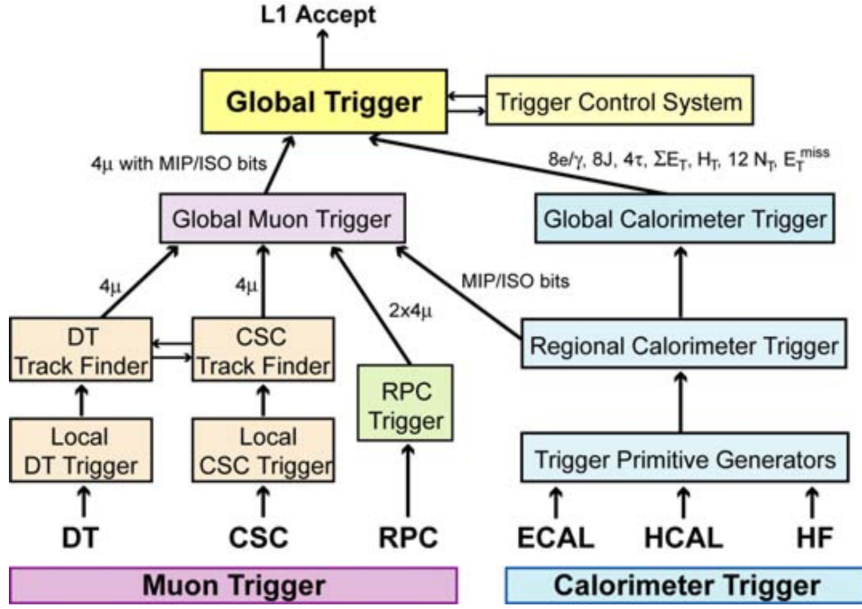


Figure 4-6: The Level-1 trigger architecture with components labeled and information flow indicated. Reprinted from Reference [73].

to produce the final set of muon candidates. The global trigger (GT) decides if an event should be sent to the HLT based on the information it receives from the GCT, the GMT, and the Timing, Trigger, and Control (TTC) system that monitors the readiness of the sub-detectors and the DAQ. The inner tracker is not included because the detector readout and reconstruction process take longer than the time allotted. Figure 4-6 shows a schematic description of the full L1 trigger process.

The HLT uses a version of the offline reconstruction software optimized to process a single event within 200 ms at the cost of some precision. The reconstruction is split into a series of filters that make decisions within regions of interested defined by the L1 trigger information. The HLT implements the desired trigger logic by constructing trigger paths out of these filters. For example, three filters relevant for dark matter searches are (1) a single photon, (2) large momentum imbalance, and (3) large hadronic energy. Combining the first two yields a trigger path targetting the monophoton channel while combining the latter two yields one for the monojet channel. To reduce CPU usage, simple decisions such as those using only the calorimeters or muon information are computed before complex decisions such as tracking.

An event must pass all the filters in a given path to be recorded in an output primary dataset (PD). Trigger paths are organized into PDs such that each PD contains events with similar topologies. Some examples are the SinglePhoton, DoubleMuon, and Jet/HT datasets. A single event that exhibits multiple different physics signatures can pass multiple trigger paths and end up in multiple PDs. These overlaps must be considered in the offline analysis.

## 4.6 Detector Simulation

The Geant4 program [75, 76] is used to simulate the detector response to the particles produced in collisions. Starting with the output of the particle-level MC described in Section 3.2, final state particles are propagated through the solenoid’s magnetic field into the passive and active elements of the detector where energy deposition, decay, and showering are simulated. Additional inelastic proton-proton collision are overlaid into an event to simulate the effects of pileup. As the particles interact with the detector, the response of the readout electronics is simulated, including the effects of noise. In order to minimize differences between simulated events and those from collisions, the reconstruction software and output format are the same for both up to the retention of additional truth information from the generators.



# Chapter 5

## Global Event Reconstruction

In the previous chapter, we discussed the interactions of particles with the individual subdetectors and how these generate electrical signals. Now, we shall discuss the reverse process, namely reconstructing the individual particles or physics objects from the electrical signals recorded by the subdetectors.

Traditionally, each class of physics object is reconstructed using information from a single subdetector: muons from the muon chambers, isolated photons and electrons from the ECAL, jets and missing transverse energy from the HCAL, and secondary vertices from  $\tau$  lepton and  $b$  hadron decays from the tracker. However, as depicted in Figure 5-1, each type of particle interacts with multiple different subdetectors and this information is lost unless the information from all the subdetectors is combined into a single global event description.

The particle flow (PF) algorithm [77] leverages the fine angular granularity of the calorimeters and the excellent momentum resolution of the inner tracker and muon chambers to greatly improve the reconstruction of physics objects and include soft particles that would otherwise be ignored. This is especially advantageous for jet energy measurements as roughly 62% of the jet energy is carried by charged hadrons, approximately 27% by photons, around 10% by neutral hadrons, and about 1.5% by neutrinos.

The distinguishing feature of the PF algorithm is to combine multiple detector signals together into a single PF candidate. The input detector signals are the tracks,

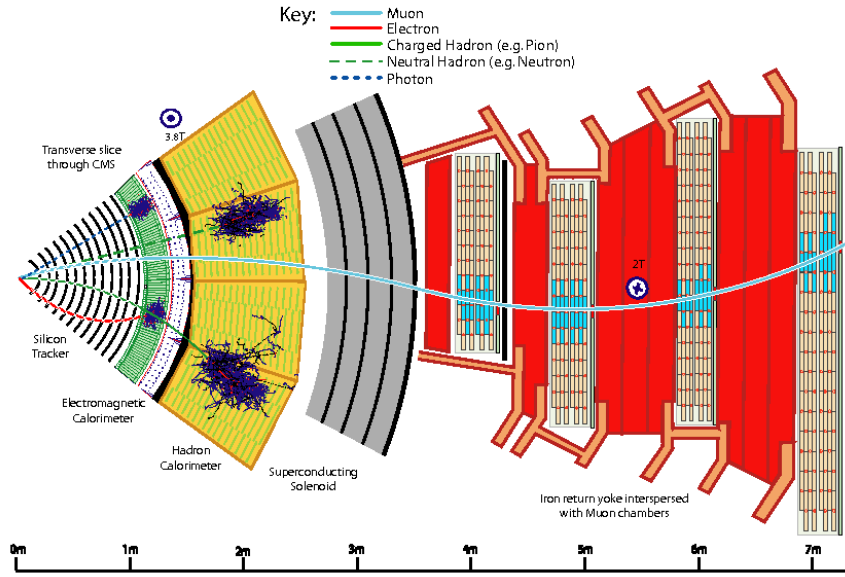


Figure 5-1: A sketch of a transverse slice of the CMS detector showing particle interactions from the interaction point to the muon detector. Reprinted from Reference [77].

vertices, calorimeter clusters, and muon segments described in Section 5.1. Based on their proximity in the  $\eta$ - $\phi$ , these PF elements are combined into muons, electrons, photons, and hadrons. Muon segments are combined with inner tracks to produce muons, inner tracks are combined with calorimeter clusters to produce electrons and charged hadrons, and calorimeter clusters are correlated to produce photons and neutral hadrons.

The PF algorithm reconstructs particles in regions of the detectors called blocks following the steps described in Section 5.2. After each step any PF elements associated to a PF candidate are removed from the block. For example, clusters associated with photons will not be used when reconstructing neutral hadrons. After all PF candidates are identified, they can be combined into event-wide variables such as jets and the missing transverse energy as described in Sections 5.2.5 and 5.2.6, respectively.

## 5.1 Particle Flow Elements

### 5.1.1 Tracks

The Combinatorial Track Finder software [78] is used to reconstruct tracks in an iterative inside-out process. Initial iterations search for tracks that are easy to find, e.g. those with high  $p_T$ , and hits associated with these tracks are removed for later iterations, reducing the combinatorial complexity and simplifying the search for more difficult tracks, e.g. greatly displaced ones.

The first step is to form seeds based on pixel hits, double strip hits containing 3D information, and an estimate of the beam spot. Earlier iterations require three pixel hits while later iterations gradually loosen the requirements. The final iterations specifically target increased muon tracking efficiency by including information from the muon chambers.

Next, a Kalman filter is used to find additional hits consistant with the evolution of the track seeds through the rest of the tracker, accounting for the magnetic field, energy loss due to ionization, and multiple scattering. The five parameters used for the helical trajectory evolution are the curvature  $\rho$ , the azimuthal angle  $\phi_0$ , the transverse impact parameter  $d_0$ , the longitudinal impact parameter  $z_0$ , and  $\lambda = \cot \theta$ , where  $\theta$  is the polar angle.

After propagating the track through all layers of the detector and finding all associated hits, a Kalman fitter and smoother is used to refit the overall trajectory while a fourth-order Runge-Kutta method is used to extrapolate the trajectory between successive hits. To reduce the fraction of fake tracks, various quality requirements concerning the number of missing hits, the reduced  $\chi^2$  of the fit, and compatibility with a primary vertex are applied before proceeding to the next iteration.

Track reconstruction for electrons is more complicated as the Kalman filter is not a good description because of the high rate of non-Gaussian energy loss due to brehmsstrahlung these tracks experience within the tracker [77]. To improve the electron reconstruction efficiency, the electron seed collection is filled both by looking outside-in for ECAL superclusters consistant with track seeds and inside-out track

seeds consistent with superclusters. A Gaussian Sum Filter (GSF) defined to approximate the Bethe-Heitler energy-loss distribution is used to fit the trajectory of electron tracks.

### 5.1.2 Primary Vertexing

A deterministic annealing (DA) algorithm is used to associate tracks to primary vertices [78]. Tracks must pass additional requirements on the transverse impact parameter  $d_0$ , the number of strip and pixel hits, and the reduced  $\chi$  of the trajectory fit to be considered when finding primary vertices. The most probable vertex positions at an artifical temperature  $T$  are determined by the minimization of the “free energy”

$$F = -T \sum_i^{N_T} \ln \sum_j^{N_V} p_{ij} \rho_j \exp \left[ -\frac{1}{T} \left( \frac{z_i^T - z_j^V}{\sigma_i^z} \right)^2 \right] \quad (5.1)$$

where the  $z_j^V$  are the vertex positions with weights  $\rho_j$ , the  $z_i^T$  and  $\sigma_i^z$  are the longitudinal impact parameters and the corresponding uncertainties of the tracks, and the  $p_{ij}$  are the probabilities of assigning the track  $i$  of  $N_T$  to the vertex  $j$  of  $N_V$ .

The DA algorithm starts with a single vertex at a very high temperature that is gradually decreased. The free energy  $F$  is minimized with respects to  $z_j^K$  at each new temperature and a vertex is split in two whenever  $T$  falls below its criticial temperature

$$T_C^j = 2 \sum_i \frac{p_i p_{ij}}{(\sigma_i^z)^2} \left( \frac{z_i^T - z_j^V}{\sigma_i^z} \right)^2 \Bigg/ \sum_i \frac{p_i p_{ij}}{(\sigma_i^z)^2}. \quad (5.2)$$

The annealing procedure with vertex splitting continues down to  $T = 4$  and the final assignment of tracks to vertices is performed at  $T = 1$  without any further splitting. The vertex designated as *the* primary vertex (PV) of the hard scattering is the one which maximizes

$$S_T = \sum_i (p_T^i)^2 + (p_T^{\text{miss}})^2, \quad (5.3)$$

where  $p_T^i$  is the transverse momentum of a track assigned to the vertex and  $p_T^{\text{miss}}$  is the magnitude of the momentum imbalance in the transverse plane for the vertex.

### 5.1.3 Secondary Vertexing

Long-lived particles such as  $b$  hadrons and  $\tau$  leptons often produce charged particles in their decays. These charged particles are traced to a secondary vertex at the location of the decay, which is identified by the inclusive vertex fitter (IVF) algorithm [79].

The IVF procedure begins by selecting seed tracks with a 2D impact parameter significance  $\sigma_{d_0} \geq 1.2$  and a 3D impact parameter  $\sqrt{d_0^2 + z_0^2} \geq 50 \mu\text{m}$ . Tracks are assigned to a secondary vertex based on their opening angle with the seed track and distance at closest approach, with the additional stipulation that this distance be smaller for the secondary vertex than for the primary vertex.

To determine the precise position of the secondary vertices, the associated tracks are fitted with the adaptive vertex fitter and any vertices with a flight distance significance less than a certain threshold are discarded. At this point, a track is unassociated from a secondary vertex if the angular distance between the track and the secondary vertex flight direction is greater than 0.4 and if the track's distance at closest approach is larger than the magnitude of its impact parameter.

The secondary vertex position is refitted after track cleaning if there are still at least two tracks associated with the vertex. The last stage of cleaning removes a secondary vertex if it shares at least 20% of its tracks with another and the flight distance significance between the two is less than ten.

### 5.1.4 ECAL Superclusters

Due to the large amount of material in the tracker, electrons often emit bremsstrahlung photons, photons often convert to electron-positron pairs, and the brehmsstrahlung photons and converted electrons often undergo further conversion and brehmsstrahlung before reaching the ECAL. Because of the bending of electron trajectories in the magnetic field, the resulting electromagnetic (EM) shower is significantly spread in the  $\phi$ -direction and collimated in the  $\eta$ -direction. The ECAL reconstruction algorithm [80, 81] combines the basic cluster from each showered particle into a supercluster representing the initial electron or photon from the hard scattering.

The first step is the identification of a seed crystal with greater transverse energy than its immediate neighbors and above a predefined minimum threshold. The energy of each crystal is determined from calibration constants combined with the amplitude and peak time obtained by fitting the pulse shape of the ten time samples surrounding the triggering bunch crossing.

In the barrel, a supercluster starts with a  $5 \times 1$  array of crystals in the  $\eta\text{-}\phi$  plane centred on the seed crystal. The array is extended around the seed crystal in the  $\phi$ -direction up to  $|\Delta\phi| \leq 0.3$  if the energy of the additional crystals exceeds a certain threshold. The contiguous array is grouped into distinct basic clusters each containing a seed array with energy greater than another threshold. The supercluster is the collection of basic threshold found in the  $\eta\text{-}\phi$  region centered on the initial seed crystal. Since the crystals in the endcaps are arranged in an  $x\text{-}y$  grid, clustering here uses fixed  $5 \times 5$  matrices of crystals. After a seed cluster is identified, additional, partially overlapping  $5 \times 5$  matrices are added if their centroid lies within  $|\Delta\eta| \leq 0.07$  and  $|\Delta\phi| \leq 0.3$ . For unconverted photons, both methods produce superclusters that are simple  $5 \times 5$  matrices.

### 5.1.5 HCAL Clusters

The purpose of clustering in the HCAL is to measure the energy and direction of neutral hadrons, disentangle neutral hadrons from charged hadron energy deposits, and improve the energy measurement for charged hadrons with poorly reconstructed tracks [77]. Similar to the supercluster algorithm, a cluster in the HCAL is first identified by a seed cell with greater transverse energy than its immediate neighbors and above a predefined minimum threshold. This seed is then grown into a topological cluster by adding cells with at least a corner in common with a cell already in the cluster and energy above twice the noise threshold.

An iterative Gaussian mixture model is used to break each topological cluster of  $M$  individual cells is broken into  $N$  energy deposits corresponding to individual particles, where  $N$  is the number of seeds. Each energy deposit is modeled as a Gaussian distribution  $\mathcal{N}$  with amplitude  $A_i$ , mean  $\vec{\mu}_i$  in the  $\eta\text{-}\phi$  plane, and width

$\sigma$  fixed by the calorimeter resolution. The expected fraction  $f_{ji}$  of the energy  $E_j$  measured in the cell at position  $\vec{c}_j$  from the  $i$ th energy deposit is

$$f_{ji} = \frac{\mathcal{N}(\vec{c}_j|A_i, \vec{\mu}_i, \sigma)}{\sum_k^N \mathcal{N}(\vec{c}_j|A_k, \vec{\mu}_k, \sigma)}. \quad (5.4)$$

The amplitude and position of each energy deposit are determined by an analytical maximum-likelihood fit to be

$$A_i = \sum_j^M f_{ji} E_j \quad \left| \quad \vec{\mu}_i = \sum_j^M f_{ji} E_j \vec{c}_j \right. \quad (5.5)$$

where the initial values are the energy and position of the seeds. The process of calculating energy fractions  $f_{ji}$  and fitting for the amplitudes  $A_i$  and positions  $\vec{\mu}_i$  is repeated until convergence, at which point they are taken as the cluster parameters.

### 5.1.6 Muon Segments

Muon segments are reconstructed from the hits in the muon chambers using a Kalman filter in a similar manner to that described for the inner tracker in Section 5.1.1. A full track constructed in this way is referred to as a standalone muon [77].

### 5.1.7 Isolation

While not a physics object persay, isolation is a key concept of the PF algorithm that distinguishes prompt leptons and photons originating in the hard scattering from those originating in the decays of hardrons during the parton shower. The latter are surrounded by a large amount of additional hadrons while the former have little hadronic activity in their vicinity, originating mainly from the pileup vertices.

The isolation of a prompt object is the total amount of energy due to additional particles within an annulus of radius  $0.01 < \Delta R < 0.4$  around the prompt object, where the lower bound avoids including the prompt object and its radiation in the sum. The isolation is calculated using either the raw energy deposits in the subdetectors or the four-momenta of the PF candidates surrounding the prompt object

depending the stage of the PF algorithm. Prompt objects are required to have an isolation value below a certain threshold, rejecting hadrons misidentified as leptons and photons as well as non-prompt leptons and photons.

The isolation calculation is usually split into three different components based on the types of particles that contribute energy. The photon isolation  $I_\gamma$  is the  $E_T$  sum of the PF photons defined in Section 5.2.3 while the charged hadron and neutral hadron isolations  $I_{\text{CH}}$  and  $I_{\text{NH}}$  are the  $p_T$  sums of the PF charged and neutral hadrons defined in Section 5.2.4, with the additional stipulation that charged hadrons be associated with the primary vertex.

In events with very few tracks, such as one with a single high  $p_T$  photon and a large momentum imbalance, it is possible that the identified primary vertex does not correspond to the  $pp$  interaction from which the photon object originates because the photon does not figure into the primary vertex calculation from Section 5.1.2. In such cases, the photon object can be surrounded by charged hadrons and still appear isolated under the standard charged hadron isolation. A conservative measure to address such misidentification is to replace  $I_{\text{CH}}$  with the maximum of the PF charged hadron isolations computed over all reconstructed vertices, e.g. the maximum charged hadron isolation  $I_{\text{CH}}^{\max} = \max_{\text{vertices}} I_{\text{CH}}$ .

To reduce the pileup dependence of these variables, the median energy density  $\rho$  of the pileup interactions in the isolation cone is calculated using the effective areas given in Table 5.1 and subtracted from each isolation sum. Additionally, since the rate of the charged particles originating from pileup interactions is about twice as large as the corresponding rate of the neutral particles, the pileup isolation  $I_{\text{PU}}$  is defined as the half the  $p_T$  sum of the PF charged hadrons *not* associated with the primary vertex. Often selections are placed on the individual isolation components when selecting prompt photons, while the relative combined PF isolation

$$I_{\text{PF}}^{\text{rel.}} = \left( I_{\text{CH}} + \max \left\{ 0, I_{\text{NH}} + I_\gamma - I_{\text{PU}} \right\} \right) / p_T^\ell \quad (5.6)$$

is used when selecting prompt leptons.

Isolation	$ \eta  < 1.0$	$1.0 <  \eta  < 1.479$
$I_{\text{CH}}$	0.0360	0.0377
$I_{\text{NH}}$	0.0597	0.0807
$I_{\gamma}$	0.1210	0.1107
$I_{\text{CH}}^{\max}$	0.01064	0.1026

Table 5.1: Effective areas for isolations.

## 5.2 Particle Identification

### 5.2.1 Muons

The first step of the PF algorithm reconstructs three types of muon candidates: standalone muons, outside-in global muons, and inside-out tracker muons. To construct a global muon, the algorithm identifies an inner track consistent with the trajectory of a standalone muon evolved inwards using a Kalman filter similar to those discussed in Section 5.1.1. After finding a match, a global muon candidate is created by combining the inner track with the standalone track with a second Kalman filter. Conversely, to construct a tracker muon, the algorithm identifies a muon segment consistent with the trajectory of a inner track with  $p_T > 0.5 \text{ GeV}$ . Global and tracker muons sharing the same inner track are merged into a single candidate. For muons with  $p_T < 200 \text{ GeV}$ , the muon momentum is that of the inner track, while the momentum is determined from a global fit of the muon chambers and inner tracker for muons with momentum above this threshold.

Hadrons misidentified muons are rejected through two separate mechanisms. First, the isolation with respects to inner tracks and calorimeter deposits within  $\Delta R < 0.3$  is required to be less than 10% of the muon  $p_T$ . Non-isolated muons are kept only if certain selections on the reduced  $\chi^2$  of the track fit and the two impact parameters  $d_0$  and  $d_z$  are satisfied. Finally, misidentified or misreconstructed muons can lead to a spurious imbalance in the transverse momentum. The procedure used to identify and remove these muon candidates is described in Section 5.2.6. The total efficiency of muon reconstruction is 99%.

The work described in this thesis only considers global muons with  $p_T > 10 \text{ GeV}$

and  $|\eta| < 2.5$ . This minimum requirement is only used to reject events containing a muon and is referred to as the veto muon ID. The loose muon ID adds the requirement that the relative combined PF Isolation  $I_{\text{PF}}^{\text{rel}}$  must be less than 0.25. must be less than 0.25. In order for a muon to pass the tight ID, it must have  $p_T > 30 \text{ GeV}$  and  $I_{\text{PF}}^{\text{rel}} < 0.15$  as well as satisfying the additional requirements in Table 5.2.

Variable	Selection	Description
$\chi^2_{\text{track fit}}/N_{\text{dof}}$	$< 10$	quality of global-muon track fit
$N_{\text{hit}}^{\mu\text{on}}$	$> 1$	at least one muon-chamber hit
$N_{\text{station}}^{\mu\text{on}}$	$> 2$	segments in at least two muon stations
$d_0$	$< 2 \text{ mm}$	reject cosmic ray muons
$d_z$	$< 5 \text{ mm}$	reject muons from pileup
$N_{\text{hit}}^{\text{pixel}}$	$> 1$	at least one pixel hit
$N_{\text{hit}}^{\text{tracker}}$	$> 5$	more than five tracker layers with hits

Table 5.2: Selections for the tight muon ID.

### 5.2.2 Electrons

Electron candidates are seeded from the GSF tracks described in Section 5.1.1 as long as the corresponding ECAL clusters are not linked to three or more additional tracks. In each block, all ECAL clusters linked to either the supercluster (SC) or one of the GSF track tangents are associated with the candidate to ensure optimal energy containment. Additional tracks linked to these clusters are associated if the track momenta and energies of any linked HCAL clusters are compatible with the electron hypothesis. Any tracks and clusters belonging to identified photon conversions linked to the GSF track tangents are associated as well.

To recover any energy lost during the association process, the total energy of the collected clusters is corrected with analytical functions of  $E$  and  $\eta$ . For ECAL-based candidates, the sum of the energies measured in the HCAL cells within  $\Delta R < 0.15$  of the supercluster must be less than 10% of the supercluster energy. The final energy of an electron candidate is a weighted average of the corrected ECAL energy and the momentum of the GSF track and the electron direction is that of its GSF track.

The work described in this thesis only considers electrons with  $p_T > 10 \text{ GeV}$  and  $|\eta| < 2.5$ . Additionally, electrons must pass further cuts on the observables listed in Table 5.3. The exact values of the cuts are tuned based on whether the electron is in the barrel or the endcap and to give desired signal efficiencies and background acceptance. The loose ID is tuned to 90% signal efficiency and 0.5% background acceptance, while the tight ID is tuned to 70% signal efficiency and 0.1% background acceptance.

Variable	Description
$\sigma_{inj\eta}$	energy-weighted cell width in the $\eta$ -direction of the SC
$\Delta\eta$ and $\Delta\phi$	angular separation between the SC seed and the GSF track
$H/E$	energy ratio of the corresponding ECAL and HCAL towers
$I_{\text{PF}}^{\text{rel.}}$	relative combined PF Isolation
$ 1/E - 1/p $	difference between calorimeter energy and tracker momentum
$N_{\text{hit}}^{\text{miss}}$	number of missing hits in the inner tracker
Conversion veto	presence of tracks originating from a converted photon

Table 5.3: Variables used in selecting electrons.

### 5.2.3 Isolated Photons

Photon candidates are seeded from the ECAL superclusters (SCs) described in Section 5.1.4 as long as they have no links to GSF tracks and  $E_T > 10 \text{ GeV}$ . The same cluster and track association process described for electrons in Section 5.2.2 is used for photons, with the photon energy and direction being that of the final supercluster. This is motivated by the observation that the additional energy corrections used to improve the photon energy resolution cause photon candidates with large cluster width to exhibit unphysical energies. Figure 5-2 is a profile of the magnitude of the energy correction in bins of  $\sigma_{inj\eta}$ , the energy-weighted cell width in the  $\eta$ -direction.

As an illustration, an unphysically large correction is causing the transverse momentum of the photon object in the event shown in Fig. 5-3 to be nearly twice as large as the transverse momentum imbalance, which is supposed to balance the visible, i.e., photon momentum. Photon candidates with wide showers are used to estimate the hadron-to-photon misidentification background, while the photon energy resolution

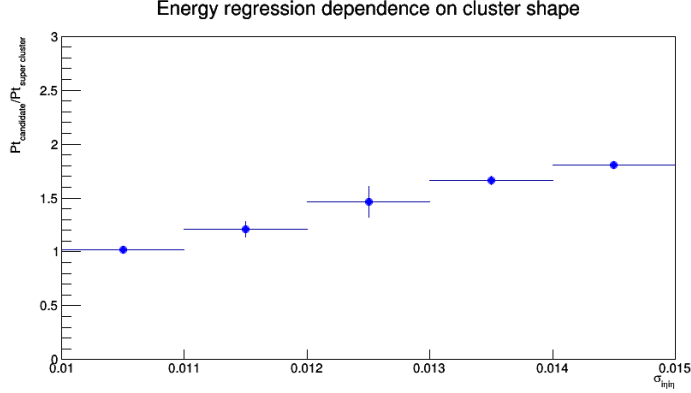


Figure 5-2: Magnitude of the energy correction on the photon object in bins of  $\sigma_{inj}$ .

has an insignificant effect. Therefore, the unbiased supercluster energy was chosen over the corrected photon energy.

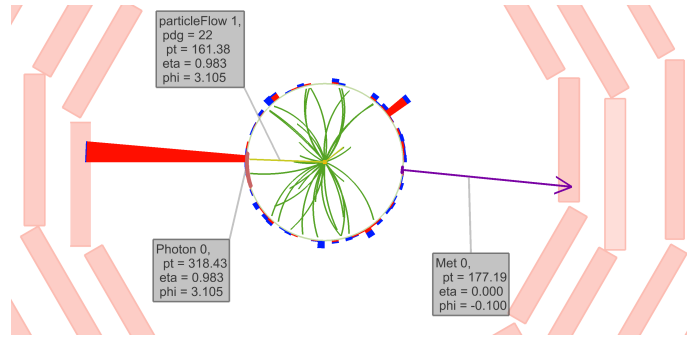


Figure 5-3: An example event where a photon with a wide shower receives a large energy correction.

For the work shown in this thesis, we are only concerned with high- $E_T$  photons from the ECAL Barrel that have a supercluster with  $E_T > 175$  GeV and  $|\eta| < 1.4442$ . To reduce hadron-to-photon misidentification rate, we apply the collection of isolation and shower shape selections in Table 5.4, which will hereby be referred to as the  $e/\gamma$  ID. To reject electrons from the candidate sample, no electron track seeds in the pixel detector can be associated to the supercluster. This is known as the pixel seed veto. To clean the candidate sample from photon objects originating from non-collision sources, we apply the collection of cuts shown in Table 5.5, which combined with the pixel seed veto constitutes the  $\gamma$ -specific ID. The beam halo tagger  $E_{MIP}$  is the total

energy deposited in ECAL by a hypothetical beam halo muon that passes through the photon cluster. See Section ?? for more detail on beam halo processes. The lower bounds on  $\sigma_{in\eta\eta}$  and  $\sigma_{i\phi i\phi}$  as well as the requirement on the cluster seed time  $|t_{\text{seed}}|$  are employed to reject spurious photon objects arising from the “ECAL spikes” discussed in Section ??.

Variable	Maximum Value
$H/E$	0.0260
$\sigma_{in\eta\eta}$	0.01040
$\rho$ -corrected $I_{\text{CH}}^{\max}$	1.146
$\rho$ -corrected $I_{\text{NH}}$	$2.792 + 0.0112 \times E_{\text{T}}^{\gamma} + 0.000028 \times (E_{\text{T}}^{\gamma})^2$
$\rho$ -corrected $I_{\gamma}$	$2.176 + 0.0043 \times E_{\text{T}}^{\gamma}$

Table 5.4: Selections for the  $e/\gamma$  portion of the photon ID. Isolation values and  $E_{\text{T}}^{\gamma}$  are all in units of GeV.

Variable	Selection	Description
$E_{\text{MIP}}$	$< 4.9 \text{ GeV}$	ECAL energy from a hypothetical beam halo muon
$\sigma_{in\eta\eta}$	$> 0.001$	non-trivial shower width in the $\eta$ -direction
$\sigma_{i\phi i\phi}$	$> 0.001$	non-trivial shower width in the $\phi$ -direction
$ t_{\text{seed}} $	$< 3 \text{ ns}$	timing of the cluster seed relative to bunch crossing

Table 5.5: Additional selections beyond the pixel seed veto for the  $\gamma$ -specific portion of the photon ID.

### 5.2.4 Hadrons

The last candidates reconstructed in a given block are the charged and neutral hadrons from fragmentation and hadronization, as well as the non-isolated muons and photons produced from their respective decays.

Inside the tracker acceptance of  $|\eta| < 2.5$ , all trackless HCAL clusters are reconstructed as neutral hadrons while all trackless ECAL clusters are reconstructed as photons. The preference towards photons is motivated because photons carry 25% of the jet energy and neutral hadrons do not interact strongly with the ECAL. Conversely, outside of the tracker acceptance, it is no longer possible to distinguish

charged and neutral hadrons, so any ECAL clusters linked to HCAL clusters are assumed to arise from unidentified charged hadrons. Thus, only unlinked ECAL clusters are reconstructed as photons and linked ECAL and HCAL clusters are reconstructed as neutral hadrons.

Afterwards, the only remaining PF elements are HCAL clusters linked to one or more tracks and ECAL clusters linked to one of these tracks. A single charged hadron is constructed for each remaining HCAL cluster, with energy equal to the sum of the ECAL and HCAL clusters and momentum equal to the sum of the individual track momenta.

If the energy of the charged hadron exceeds its momentum by an amount larger than the calometric energy resolution, neutral hadrons and photons are added. For excesses greater than 500 MeV, a photon with energy equal to the excess is created. If this photon cannot explain the entire excess, e.g. the excess is larger than the ECAL energy by at least 1 GeV, the remainder is identified as a neutral hadron. After photons and neutral hadrons consume the excess calometric energy, charged hadrons are constructed from the linked tracks with their energy and momentum determined by the track momenta under the charged-pion hypothesis.

If energy and momentum of the charged hadron are compatible, no neutral particles are identified. A charged hadron candidate is created for each track linked to the HCAL cluster, with momenta determined by a  $\chi^2$  fit of the tracker and calorimeter measurements. This combination ensures a smooth transition between the tracker-dominated low-energy regime and the calorimeter-dominated high-energy regime while always improving the final energy resolution.

If the momentum of the charged hadron exceeds its energy by three standard deviations, new PF muons are made from any non-isolated global muons failing the cleaning described in Section 5.2.1 with momentum resolution better than 25%. If, after masking the tracks from these muons, the track momentum sum still greatly exceeds the calorimeter energy, all remaining tracks with a  $p_T$  uncertainty greater than 1 GeV are identified, sorted in decreasing order of this uncertainty, and sequentially masked until no such tracks remain or the momentum excess disappears, whichever

comes first. At this point, the HCAL cluster is reconstructed according to one of the procedures defined in the preceding paragraphs.

When three or more charged particle candidates are linked to a secondary vertex identified as described in Section 5.1.3, a single primary charged hadron with energy equal to the sum of their energies replaces them in the reconstructed particle list. If an incoming track is associated with the vertex, it determines the direction of the primary charged hadron, which is otherwise determined by the vectorial sum of momenta of the secondary particles. If the momentum of the incoming track is well measured, the energy of undetected secondary particles is estimated and added to the energy of the primary charged particle.

### 5.2.5 Jets

As discussed in Section 3.2, jets are produced during the fragmentation and hadronization of colored particles produced in the hard scattering. After all PF candidates have been identified, a sequential recombination algorithm is used in an attempt to cluster these jets. Given an object  $i$  in the event  $E$ , we define the distance to the beam and the distance to another object  $j$  to be

$$d_{iB} = (p_T^i)^{2q} \quad \left| \quad d_{ij} = \min \left\{ (p_T^i)^{2q}, (p_T^j)^{2q} \right\} \frac{(\Delta R_{ij})^2}{R^2}, \right. \quad (5.7)$$

respectively, where  $q$  and  $R$  are tunable parameters and  $\Delta R_{ij}$  is the angular distance between the two particles. The distance parameter  $R$  is an approximate measure of the cone size  $\Delta R$  of the jet, while the power of the energy scale  $q$  defines the relationship between the relationship between the momentum and angular factors. Jets clustered with  $q = -1$  are referred to as anti- $k_T$  jets, those with  $q = 0$  as Cambridge-Aachen jets, and those with  $q = 1$  as  $k_T$  jets. Negative values of  $q$  force the clustering of circular jets around hard seeds ensuring that the resulting jet boundaries are resilient with respect to soft radiation. Within CMS, anti- $k_T$  jets with  $R = 0.4$  are used to cluster the parton shower from single partons.

The implementation in the FastJet library reduces the computational complex-

ity of clustering from  $\mathcal{O}(N^2)$  to  $\mathcal{O}(N \log N)$  for jets with hundreds or thousands of constituent particles. First, the two objects  $i$  and  $j$  with the smallest distance  $d_{ij}$  between them are found. If  $d_{ij}$  is less than both  $d_{iB}$  and  $d_{jB}$ , they are removed from  $E$  and a single object  $k$  with four-momentum  $p_\mu^k = p_\mu^i + p_\mu^j$  which is added in their place. Otherwise if  $d_{iB} < d_{jB}$ , object  $i$  is removed from  $E$  and added to the set of jet candidates  $J$  while object  $j$  is kept, and vice versa if  $d_{jB} < d_{iB}$ . This procedure continues until all objects are removed from  $E$  and  $J$  contains all possible jet candidates.

### 5.2.6 Missing Tranverse Energy

The production of neutrinos and dark matter candidates produces a momentum imbalance in the transverse plane. The missing transverse momentum  $\vec{p}_T^{\text{miss}}$  is defined as the negative vectorial sum of all the PF candidates in the event  $E$  such that

$$\vec{p}_T^{\text{miss}} = - \sum_{i \in E} \left( \hat{x} \cdot p_T^i \cos \phi + \hat{y} \cdot p_T^i \sin \phi \right), \quad (5.8)$$

and its magnitude is the missing transverse energy  $E_T^{\text{miss}} = |\vec{p}_T^{\text{miss}}|$ . In a perfectly reconstructed event, non-zero  $E_T^{\text{miss}}$  implies the presence of neutrinos or DM candidates; however, the failure to properly reconstruct energy deposits or the reconstruction of PF candidates with incorrect energy results in events with large amount of fake  $E_T^{\text{miss}}$ .

One last cleaning of the PF candidates is conducted in an attempt to fix these events. To remove muons from cosmic rays, muon candidates with trajectories more than 1 cm away from the beam axis are removed if the measured  $E_T^{\text{miss}}$  is consequently reduced by half. For muons with  $p_T > 20 \text{ GeV}$ , the choice of subdetector used to estimate momemtum is reviewed and the smallest available estimate used if it reduces the measured  $E_T^{\text{miss}}$  by half. Additionally, the assignment of charged hadrons and neutral hadrons is reconsidered to ensure a charged hadron is not reconstructed as a muon and neutral hadron and vice versa.

Fake  $E_T^{\text{miss}}$  can persist in an event even after the final cleaning of PF candidates. At this point, events are checked against a known set of filters identifying possible sources of fake  $E_T^{\text{miss}}$  not captured by the PF algorithm. One set of filters is the HCAL

and ECAL filters that identify events with calorimeter clusters caused by noise from the shape and timing of the energy distribution. Another such filter is the beam halo filter that identifies energy deposits from muons produced from interactions between the beam and the machine that travel parallel to the beam. These muons are identified by their localization in  $\phi$  and a longitudinal track left in the ECAL endcaps and the CSCs. Applying these filters removes essentially all remaining events with fake  $E_T^{\text{miss}}$  while rejecting less than 1% of events with real  $E_T^{\text{miss}}$ .

### 5.2.7 ECAL gain-switch effect

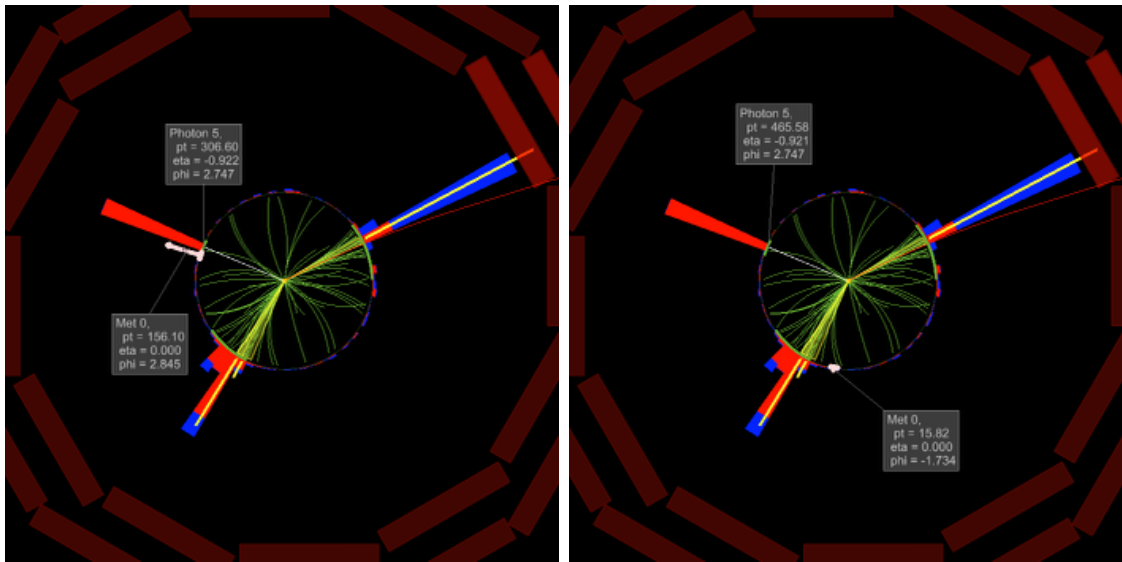


Figure 5-4: Two event displays comparing the same event, reconstructed without (left) and with (right) the fix for ECAL gain-switch effect.

The “multi-fit” algorithm for ECAL hit reconstruction was found to have an unexpected behavior when there is a large energy deposit onto a single ECAL crystal, such that the electronic signal converted at the frontend electronics is sourced partially from channels of the preamplifier with lower gains (6 or 1) than the default (12) channel. In the most dramatic cases, pulse misreconstruction would result in underestimation by hundreds of GeV of photon  $p_T$ . This effect is mitigated in the reprocessed data set used for this analysis by identifying ECAL clusters whose seed crystal hit had a switch of gains, and performing an alternative pulse reconstruction

when possible.

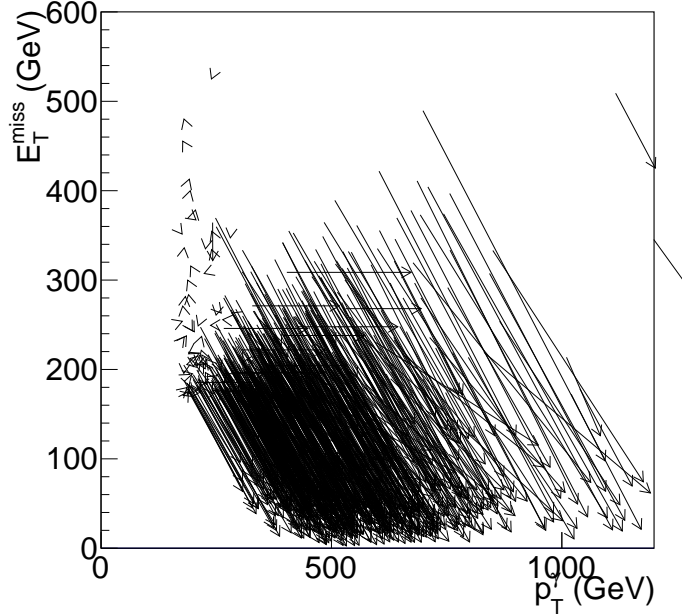


Figure 5-5: The change in reconstructed photon  $p_T$  and  $E_T^{\text{miss}}$  for events in the bin  $\Delta\phi(\gamma, p_T^{\text{miss}}) < 0.05$  of the distribution in Figure ???. Each arrow represents a single event, the tail (head) of the arrow corresponding to  $(E_T^\gamma, E_T^{\text{miss}})$  coordinates in the datasets without (with) the fix for the gain-switch problem.

The gain-switch problem affected the analyses documented in this thesis, since large underestimation of the energy of a photon in an otherwise typical  $\gamma+\text{jets}$  event would introduce large missing transverse momentum to the event, typical collinear to the affected photon. Figures 5-4 and 5-5 are the visualization of how the new dataset changes the reconstructed photon energy and  $E_T^{\text{miss}}$ .

# Chapter 6

## The Monophoton Analysis

In this chapter, we discuss the search for dark matter produced in association with a single high- $p_{\mathrm{T}}$  photon. Our benchmark signal models are the vector and axial dark matter mediators discussed previously. However, many Standard Model (SM) processes are also capable of producing events with a single high- $p_{\mathrm{T}}$  photon and large  $E_{\mathrm{T}}^{\mathrm{miss}}$ , whether with real photons, other particles misidentified as photons, or unphysical photon signatures from various machine and detector processes.

The most significant are the irreducible backgrounds, where the underlying physics process produces the exact same signature as the signal with only real and properly identified physics objects. In this case, the irreducible backgrounds are the associated production of a high-energy  $\gamma$  with either a  $Z$  boson that subsequently decays to a pair of neutrinos or a  $W$  boson that decays to a charged lepton and a neutrino, with the charged lepton outside of the detector acceptance. These two processes are denoted as  $Z(\rightarrow \nu\bar{\nu})+\gamma$  and  $W(\rightarrow \ell\nu)+\gamma$ , respectively, and together they account for approximately 70% of the SM background, with 50% from the former and 20% from the latter. The modeling of the irreducible backgrounds is explained in Section 6.6.

Additional backgrounds arise from events where the candidate photon object is a misidentified electron (Section 6.4) or an electromagnetic shower caused by hadrons (Section 6.5). The background events from electron misidentification are mostly  $W$  boson production ( $W \rightarrow e\nu$ ), whereas those from hadron misidentification are due to multiple sources such as  $Z(\rightarrow \nu\nu) + \text{jets}$  and QCD multijets with grossly mismea-

sured jet energy. Misidentification itself is rare, but because these processes have high cross sections, the amount of background is substantial, approximately 15% and 5% respectively. Since object misidentification rates depend on subtle details of the detector, the MC simulation often fails to accurately describe them. Therefore, the contributions from these background processes are estimated by employing data-driven techniques, where the misidentification rates are measured in data and applied to proxy samples with well-identified electrons or hadrons.

Finally, apparent large energy deposits in ECAL from non-collision processes mimic  $\gamma+E_T^{\text{miss}}$  events and therefore need to be controlled. Known sources of such background include bremsstrahlung of beam halo or cosmic ray muons and anomalous ECAL energy deposits resulting from the interaction of particles in the ECAL photodetectors referred to as “ECAL spikes”. These methods used to estimate contributes from these processes are described in detail in Sections 6.7 and 6.8, respectively.

The estimates of the contributions from  $Z(\rightarrow \nu\bar{\nu})+\gamma$ ,  $W(\rightarrow \ell\nu)+\gamma$ , and beam halo processes are allowed to float in the fits to data performed to extract the potential signal contribution and set limits on new physics models. Meanwhile, for all other background processes, the yields in the fits are fixed to the estimates from data-driven methods or MC cross section calculation.

## 6.1 Dataset

The data sample was collected with a single-photon trigger: `HLT_Photon165_HE10`. This high-level trigger algorithm is relatively simple, only requiring at least one photon candidate with  $E_T > 165 \text{ GeV}$  reconstructed with a corresponding L1 seed. The photon candidate must also have  $H/E < 0.1$  to discriminate against jets, where  $H/E$  is the ratio of HCAL to ECAL energy deposits in the central calorimeter tower corresponding to the candidate. The photon energy reconstructed at the HLT is less precise relative to that derived later in the offline reconstruction. Therefore, the online thresholds in the trigger on both  $H/E$  and  $E_T^\gamma$  are less restrictive than their offline counterparts.

The trigger efficiency is measured to be about 98% for events passing the analysis selection with  $E_T^\gamma > 175$  GeV and the integrated luminosity of the analyzed data sample is  $(35.9 \pm 0.9) \text{ fb}^{-1}$  [82].

### 6.1.1 Trigger Efficiency

We measure the trigger efficiency by looking for trigger objects that match the candidate photon object in an appropriate data set because the trigger decisions are based on the existence of a single photon object in the event. A trigger object is the four-momenta of an object reconstructed at the trigger level that is used for making trigger decisions. A trigger object is matched to the candidate when their angular separation  $\Delta R = \sqrt{\Delta\eta^2 + \Delta\phi^2}$  is less than a certain threshold. For the photon candidate object, a line that connects the detector origin and the cluster position was used to define its direction because photons leave no tracks and do not bend in the magnetic field.

The trigger efficiency measurement is performed on the SingleMuon data set, exploiting events mostly from leptonic  $t\bar{t}$  ( $e\mu$ ) topology. Events with a candidate-quality photon without the pixel seed veto requirement and a muon object that passes the “tight” identification requirement and matches the trigger object of the HLT\_IsoMu24 or HLT\_IsoTkMu24 triggers are used. The matching rate of the photon object and the trigger object is the trigger efficiency. Figure 6-1 shows the L1+HLT combined efficiency as a function of the photon  $E_T$ . It can be seen that the trigger is fully efficient for  $E_T > 175$  GeV.

For the first period of data taking, the HLT\_Photon165\_HE10 trigger was seeded only by an isolated  $e/\gamma$  L1 trigger. This L1 seed becomes inefficient at high  $E_T$  due to a misconfiguration in the  $H/E$  computation algorithm as indicated by the drop in efficiency at high- $E_T$  shown in the left side of Figure 6-2. To mitigate the effect, in the later periods, the trigger was seeded by the logical **OR** of SingleEG40 and SingleJet L1 triggers, combining multiple with various  $p_T$  thresholds.

Even with this addition, the measured trigger efficiency is not 100% at the plateau, but it is flat with respect to  $E_T$  as shown on the right of Figure 6-2. In principle,

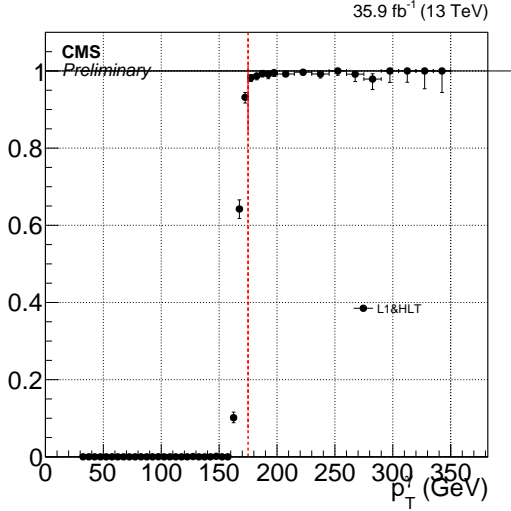


Figure 6-1: The efficiency turn-on of the `HLT_Photon165_HE10` trigger for photons passing the candidate selection, measured using  $\mu + e/\gamma$  events from the SingleMuon data set. Red vertical line corresponds to  $E_T = 175$  GeV.

the efficiency should be applied to all simulation-based background estimates whose normalization is fixed by theoretical calculation of the cross section. However, the only simulation-based background processes with absolute normalization are those that contribute at  $\mathcal{O}(1)\%$ , with large systematic uncertainties. Therefore we deem the slight discrepancy of the trigger efficiency from unity as irrelevant.

### 6.1.2 Pileup Reweighting

The distribution of the number of pileup interactions inserted into MC events differ from the true pileup distribution, estimated from the measurement of instantaneous luminosity, beam intensity of each proton bunch, and the total cross section of proton inelastic scattering ( $69.2 \text{ mb}^{-1}$ ).

Figure 6-3 shows the pileup distributions in data and MC and their ratio. Each simulation event has its weight multiplied by the value of the ratio evaluated at the number of true pileup interaction injected into the event.

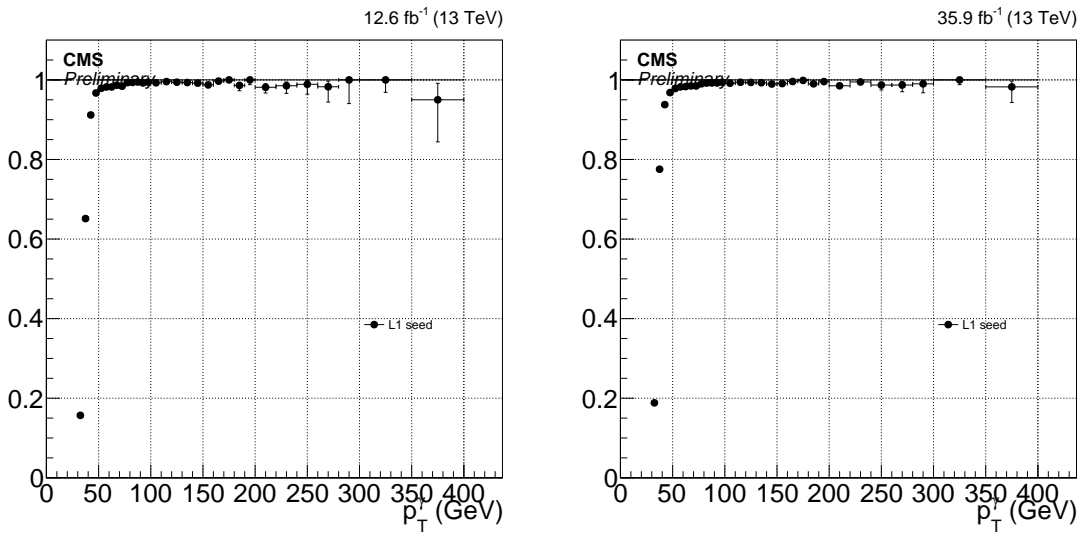


Figure 6-2: The efficiency of the L1 seed for the signal trigger in periods B and C (left) and the full data set (right). The drop in efficiency at high- $E_T$  in the earlier period is fixed by the addition of SingleJet L1 seeds during the remainder of data-taking.

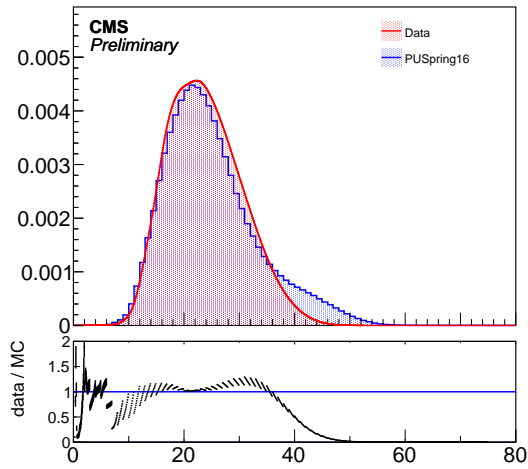


Figure 6-3: The pileup distributions in data and MC.

## 6.2 Event Selection

From the recorded data, events are selected by requiring  $E_T^{\text{miss}} > 170 \text{ GeV}$  and at least one photon with  $E_T^\gamma > 175 \text{ GeV}$  in the fiducial region of the ECAL barrel ( $|\eta| < 1.44$ ). Events with photons in the endcaps are not considered because the estimate of backgrounds due to beam halo and misidentified hadron are greatly complicated due to the  $x$ - $y$  grid of the crystals in the endcaps.

Events with a high- $p_T$  photon and large  $E_T^{\text{miss}}$  are subjected to further requirements to suppress SM background processes that feature a genuine high-energy photon, but not a significant amount of  $E_T^{\text{miss}}$ . One such SM process is  $\gamma + \text{jets}$ , where an apparently large  $E_T^{\text{miss}}$  is often the result of mismeasuring the energy of a jet. In contrast to signal-like processes, the  $E_T^{\text{miss}}$  is typically smaller than  $E_T^\gamma$  in these events, so requiring the ratio of  $E_T^\gamma$  to  $E_T^{\text{miss}}$  to be less than 1.4 rejects this background effectively with little effect on signal efficiency. Events are also rejected if the minimum opening angle between  $\vec{p}_T^{\text{miss}}$  and the directions of the four highest  $p_T$  jets,  $\min\Delta\phi(\vec{p}_T^{\text{jet}}, \vec{p}_T^{\text{miss}})$ , is less than 0.5. Only jets with  $p_T > 30 \text{ GeV}$  and  $|\eta| < 5$  are considered in the  $\min\Delta\phi(\vec{p}_T^{\text{jet}}, \vec{p}_T^{\text{miss}})$  calculation. In the  $\gamma + \text{jets}$  process, rare pathological mismeasurements of  $E_T^\gamma$  also lead to large  $E_T^{\text{miss}}$ . For this reason, the candidate photon  $\vec{p}_T$  and  $\vec{p}_T^{\text{miss}}$  must be separated by more than 0.5 radians.

Variable	Selection	Motivation
$E_T^\gamma$	$> 175 \text{ GeV}$	high- $p_T$ photon passing trigger
$ \eta $	$< 1.44$	region with best background estimates
$E_T^{\text{miss}}$	$> 170 \text{ GeV}$	characteristic signature of dark matter
$E_T^\gamma/E_T^{\text{miss}}$	$< 1.4$	reduce jet mismeasurement backgrounds
$\min\Delta\phi(\vec{p}_T^{\text{jet}}, \vec{p}_T^{\text{miss}})$	$< 0.5$	reduce jet mismeasurement backgrounds
$\Delta\Phi(\vec{p}_T^\gamma, \vec{p}_T^{\text{miss}})$	$> 0.5$	reduce photon mismeasurement backgrounds

Table 6.1: Baseline selections for all events considered in the analysis.

The above selections, summarized in Table 6.1, constitute the baseline selections common to all regions. To improve the purity of the signal region, we require a more stringent photon identification as well as additional object vetos. The contributions from the  $Z(\rightarrow \nu\bar{\nu}) + \gamma$  and  $W(\rightarrow \ell\nu) + \gamma$  processes to the signal region are modeled by fitting to observed data in control regions where one or two leptons (electrons

or muons) are identified in addition to the photon candidate while the contributions from misidentified electrons and hadrons are modeled by proxy regions where some of the selections in the photon identification have been inverted. The additional requirements for the various signal, control, and proxy regions used in the analysis are described in the following sections.

### 6.2.1 Signal Regions

The defining feature of the signal region is the application of both the  $e/\gamma$  and  $\gamma$ -specific portions of the photon ID, given in Tables 5.4 and 5.5 respectively. The former reduces the hadron misidentification rate with a collection of isolation and shower shape selections while the latter reduces the electron misidentification rate with the pixel seed veto and rejects non-collisions backgrounds with specifically tailored selections.

In the signal region, events are vetoed if they contain an electron or a muon with  $p_T > 10 \text{ GeV}$  that is separated from the photon by  $\Delta R > 0.5$ . This lepton veto rejects SM processes that produce a high- $p_T$  photon,  $E_T^{\text{miss}}$ , and leptons such as  $W(\rightarrow \ell\nu) + \gamma$ ,  $t\bar{t}\gamma$ , and  $VV\gamma$ .

Furthermore, to constrain the beam halo normalization, the signal region is split into two parts according to the variable  $\phi'$  introduced in Equation 6.9. The region defined by  $|\phi'| < 0.5$  is called the horizontal region, its complement  $0.5 < |\phi'| < \pi/2$  is called the vertical region, and the two together are referred to as the combined signal regions.

### 6.2.2 Control Regions

The single-electron (single-muon) control region is defined by requiring exactly one tight electron (muon) with  $p_T > 30 \text{ GeV}$  and  $|\eta| < 2.5$  ( $2.4$ ) in addition to requiring the same photon ID as in the signal regions. To suppress the contributions from large- $E_T^{\text{miss}}$  processes other than  $W(\rightarrow \ell\nu) + \gamma$ , the transverse mass  $m_T = \sqrt{2E_T^{\text{miss}} p_T^\ell [1 - \cos \Delta\phi(\vec{p}_T^{\text{miss}}, \vec{p}_T^\ell)]}$  must be less than  $160 \text{ GeV}$ . Additionally, for the

single-electron control region,  $E_T^{\text{miss}}$  must be greater than 50 GeV to limit the contribution from the  $\gamma + \text{jets}$  process, where a jet is misidentified as an electron.

The dielectron (dimuon) control region is defined by exactly two electrons (muons) in addition to the photon, with  $60 < m_{\ell\ell} < 120$  GeV, where  $m_{\ell\ell}$  is the mass of the dilepton system. The leading lepton must pass the tight ID requirements, while the trailing lepton only needs to pass the loose ID requirements.

Finally, in the control regions, the recoil vector  $\vec{U} = \vec{p}_T^{\text{miss}} + \sum_{\ell} \vec{p}_T^{\ell}$  serves as an analogue for the  $\vec{p}_T^{\text{miss}}$  in the signal region. In the signal region, the  $\vec{p}_T^{\text{miss}}$  is a proxy for the vector boson  $p_T$  while in the control regions, the recoil vector is used instead. Thus, the recoil  $\vec{U}$  must satisfy identical requirements to those for the  $\vec{p}_T^{\text{miss}}$  in the signal region to keep the control region kinematics as similar as possible to the signal region kinematics.

### 6.2.3 Proxy Samples

To estimate the background due to misidentified electrons, an electron proxy sample is used. This proxy sample is obtained by identical event selection as that of the signal region but with the pixel-seed veto inverted on the photon candidate object. Such a photon candidate is referred to as an electron proxy object. This yields a sample of events with similar kinematics to the signal region and well-identified electron candidates, differing only from the misidentified electron events in that a pixel hit was associated with the photon object. Thus, these exact events are used to estimate the misidentified electron background after scaling them by the electron-to-photon misidentification rate.

To estimate the background due to misidentified hadrons, a hadron proxy sample is used. This proxy sample is obtained by identical event selection as that of the signal region but where the photon candidate passes the  $e/\gamma$  and  $\gamma$ -specific IDs with exception for at least one of the following cuts:  $\sigma_{inj} < 0.01022$  and  $I_{\text{CH}} < 0.441$  GeV. Such a photon candidate is referred to as a hadron proxy object. This yields a sample of events with similar kinematics to the signal region and well-identified proxies for misidentified hadrons. Thus, these exact events are used to estimate the misidentified

hadron background after scaling them by the hadron-to-photon misidentification rate.

Additional tight and loose hadron proxy objects and samples are made by tightening and loosening the constant term in the  $I_{\text{NH}}$  and  $I_{\gamma}$  requirements on the proxy object. The specific values for each proxy object are shown in Table 6.2.

	$I_{\text{NH}}$ (GeV)	$I_{\gamma}$ (GeV)
Nominal	2.792	2.176
Loose	10.910	3.630
Tight	0.264	2.362

Table 6.2: Constant terms in the  $I_{\text{NH}}$  and  $I_{\gamma}$  selections for the hadron proxy objects.

#### 6.2.4 Measurement Samples

To measure the photon purity and part of the photon efficiency, an EM object+jet measurement sample is formed by requiring an EM object with  $E_{\text{T}} > 175 \text{ GeV}$  and  $|\eta| < 1.44$  plus at least one jet with  $p_{\text{T}} > 100 \text{ GeV}$  and  $|\eta| < 2.5$  which passes the loose jet ID. An EM object is a photon candidate that passes the  $e/\gamma$  ID with the exception of the following relaxed cuts:  $\sigma_{i\eta i\eta} < 0.015$  and  $I_{\text{CH}} < 11.0 \text{ GeV}$ . Additionally, we apply an  $E_{\text{T}}^{\text{miss}} < 60 \text{ GeV}$  cut to make this region orthogonal to the signal region.

To measure the hadron misidentification rate, a hadron proxy+jet measurement sample is formed by replacing the the EM object in the EM object+jet sample with a hadron proxy object, one for each type of hadron proxy. These are exactly the same as the hadron proxy samples, except that a high- $p_{\text{T}}$  jet has replaced the high- $E_{\text{T}}^{\text{miss}}$ , minimizing the kinematic differences between the two.

### 6.3 Efficiencies and Scale Factors

While we try to model the CMS detector as accurately as possible with our MC simulations, there are still differences between the behavior of physics objects within the simulations and those from data taken with the detector. Most importantly, this results in different efficiencies for photons and leptons in data and MC, which we

must measure. To improve our MC, we reweight it by the ratio of the efficiency in data to that in MC, known as the scale factor.

When measuring the scale factor for photons, we factorize the photon ID into the  $e/\gamma$  portion and the  $\gamma$ -specific portion. The  $e/\gamma$  portion of the ID consists of a collection of isolation and shower shape selections designed to reduce the hadron misidentification rate. We measure the efficiency of the  $e/\gamma$  portion using the “tag-and-probe” (TP) method with  $Z \rightarrow ee$  events as these variables have similar efficiencies for physical electrons and photons. The  $\gamma$ -specific portion of the ID consists of the pixel seed veto and non-collision rejection cuts. We measure the efficiency of  $\gamma$ -specific portion on a sample of physical photons in the EM object+jet measurement sample using a  $\sigma_{i\eta i\eta}$  template fit method.

We perform both efficiency estimates as a function of  $p_T$  with the binning [175,200], [200,250], [250,300], [300,350], [350,400] and [400,∞). This binning was chosen based on the number of available events in data for the failing probes fit in the TP method and the background template for the  $\sigma_{i\eta i\eta}$  fits, as these samples are the smallest and drive the uncertainty of the methods.

### 6.3.1 $e/\gamma$ ID Efficiency

The efficiency corresponding to the  $e/\gamma$  part of the photon ID is estimated by exploiting  $Z$  boson decays into pairs of electrons and positrons. Using the TP method, a high-quality electron object (tag) is identified in a single photon data sample, and the accompanying electron is sought for in the pool of electromagnetic objects (probes) in the event. The area under the peak in the mass distribution of the tag-probe system around the  $Z$  boson mass (between 81 GeV and 101 GeV) is then measured once applying the  $e\gamma$  ID requirements on the probe and once inverting all of the requirements simultaneously. Denoting the two areas under the peaks in the passing and failing samples  $N_{\text{pass}}$  and  $N_{\text{fail}}$ , respectively, the resulting efficiency  $\epsilon_{e/\gamma}$  is given by

$$\epsilon_{e/\gamma} = \frac{N_{\text{pass}}}{N_{\text{pass}} + N_{\text{fail}}}. \quad (6.1)$$

The TP measurement is performed on a subset of the single photon triggered events where there is an electron object (tag) passing the “tight” identification criteria in addition to the triggering photon (probe). All possible tag-probe combinations are considered; if the tag object can also serve as a probe and the probe object as a tag, which is a common occurrence in the case when the probe is electron-like (passes the  $e\gamma$  ID), then the two combinations are considered independently to avoid the bias caused by preferring to use one object over another as the probe.

The tag-probe mass distributions are then fit to extract  $N_{\text{pass}}$  and  $N_{\text{fail}}$ . The fit model is composed of two templates, where one template describes a pure  $Z \rightarrow ee$  line shape and the other describes the background contributions. The backgrounds to the fits include  $W+\text{jets}$ , diboson, and  $t\bar{t}$  productions, which are all negligible and estimated to contribute by less than 1%. Minor contributions from processes that do not involve true electrons, such as diphoton production with a strongly asymmetric conversion on one of the photons and misidentification of a QCD jet as an electron, are predicted to be negligible from MC studies.

The  $Z \rightarrow ee$  template shape is an analytic convolution of the Breit-Wigner distribution and the Crystal Ball function. The mass and width parameters of the Breit-Wigner distribution are fixed to PDG values while the Crystal Ball parameters are allowed to float in the fit. We are able to use the analytic Breit-Wigner distribution instead of a template taken from MC because at this high probe  $p_T$  scale the selected events are mostly of the  $Z+\text{jets}$  topology with a boosted  $Z$  boson. This makes the selection rather inclusive in terms of the tag-probe invariant mass and ensures that the Breit-Wigner distribution accurately models the mass distribution even through the tag and probe are under kinematically exclusive selections.

The background template is taken from events collected by the single photon trigger where an additional muon object is present, making use of the fact that the most of the background processes in both fits are symmetric in lepton flavor. In order to mitigate statistical fluctuations in the background sample, the actual template is constructed by a Gaussian kernel estimation of the mass distribution of this muon-probe sample.

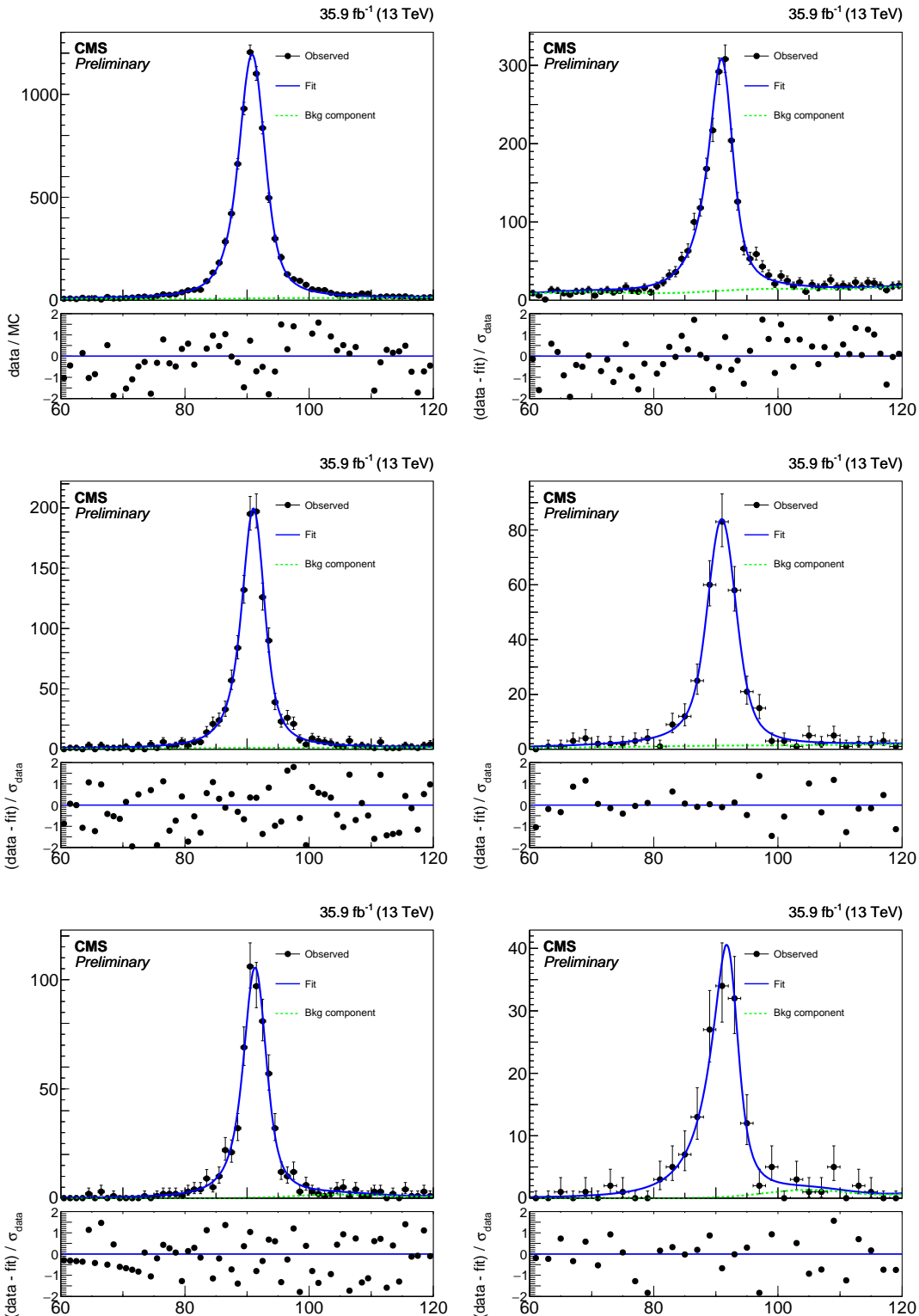


Figure 6-4: Fits to the mass distributions for pass (left) and fail (right) selections, in bins of probe  $p_T$ :  $175 < p_T < 200 \text{ GeV}$  (top),  $300 < p_T < 350 \text{ GeV}$  (middle),  $p_T > 400 \text{ GeV}$  (bottom). The blue solid line represents the full fit model, and the green dashed line its background component.

The floating parameters of the fits are therefore the normalizations of the  $Z \rightarrow ee$  and background templates and the Crystal Ball smearing parameters. Selected example fits are shown in Figure 6-4.

The statistical uncertainty of the fits is estimated by generating toy data from the nominal fit result with the same number of entries as the fit target distribution. The mass distribution of the toy data is then fit with the same model with the parameters floating. This procedure is repeated 100 times to obtain a distribution of the  $Z \rightarrow ee$  event yields, and its standard deviation is taken as the statistical uncertainty of the fit. Relative statistical uncertainty on the efficiency is 10%.

To estimate the effect of potential mismodeling in the fits, alternative fits varying the background and signal templates are performed first. In the alternative-background fit, a simple linear function is tested. In the alternative-signal fit, no Crystal Ball convolution is performed to the signal template and the mass and width of the Breit-Wigner function are allowed to vary. Resulting best-fit distributions of these alternative models are then used to generate a large number of toy distributions, which are fit by the nominal model. The average shift of the fit result from the nominal value is then taken as the uncertainty. The relative uncertainty on the efficiency varies from 2 to 4% depending on the probe  $p_T$  bin.

The MC efficiency is taken from counting the number truth-matched electrons passing and failing the  $e/\gamma$  part of the ID from a  $Z \rightarrow ee$  sample. Additionally, the MC efficiency is computed using the same procedure as in data as a cross-check. The efficiencies obtained from these two methods are consistent within their uncertainties.

$p_T^{\text{probe}}$ (GeV)	MC Fit	Truth
(175, 200)	$1.014 \pm 0.008$	$1.009 \pm 0.016$
(200, 250)	$1.003 \pm 0.008$	$0.999 \pm 0.014$
(250, 300)	$1.014 \pm 0.010$	$1.016 \pm 0.019$
(300, 350)	$1.002 \pm 0.014$	$0.997 \pm 0.022$
(350, 400)	$0.986 \pm 0.012$	$0.987 \pm 0.022$
(400, 6500)	$0.988 \pm 0.011$	$0.999 \pm 0.016$

Table 6.3:  $e/\gamma$  scale factors as a function of photon  $p_T$ .

The data efficiencies, MC efficiencies, and resulting scale factors as a function of

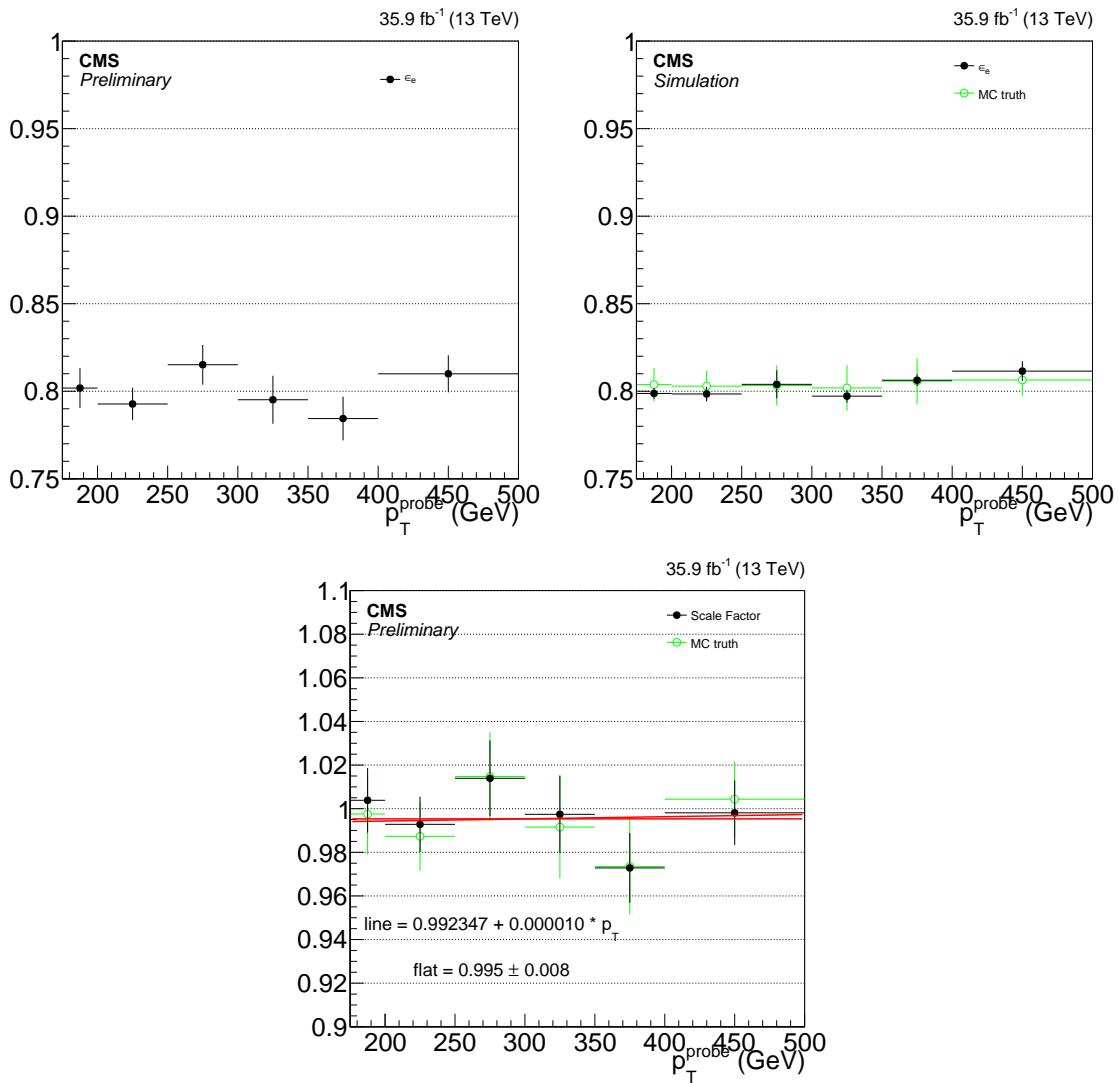


Figure 6-5:  $e/\gamma$  component of the photon identification efficiency for data (top-left) and MC (top-right) and corresponding scale factor (bottom) as a function of photon  $p_T$ .

$p_T$  are shown in Figure 6-5. The scalefactors are consistent with unity within the uncertainties. The numerical values are given in Table 6.3. We use the bin by bin scale factor corresponding to the truth values in the analysis.

### 6.3.2 $\gamma$ -specific ID Efficiency

To measure the efficiency of the  $\gamma$ -specific component of the photon ID, we use a  $\sigma_{i\eta i\eta}$  template fit to extract the number of true photons from a pool of photon objects passing the  $e/\gamma$  ID.

The measurement is performed using the EM object+jet measurement sample. We fit the  $\sigma_{i\eta i\eta}$  distribution of the EM object with a template describing the  $\sigma_{i\eta i\eta}$  shape of true photons and another describing the hadronic background. The real photon template is taken from  $\gamma$ +jets MC requiring the photon to pass the  $e/\gamma$  ID except for the  $\sigma_{i\eta i\eta}$  requirement. The fake photon template is taken from the same data control sample, requiring  $5 \text{ GeV} < I_{\text{CH}} < 7 \text{ GeV}$ . The number of true photons in the target sample is the integral of the post-fit real photon template below  $\sigma_{i\eta i\eta} = 0.0104$ , the same value as in our photon ID.

The fit is performed once for all EM objects and then once for EM objects passing the  $\gamma$ -specific ID criteria. The ratio of the numbers of true photons obtained in the two fits is the efficiency.

The  $\sigma_{i\eta i\eta}$  template fit method in its simplest form fits the observed distribution with the following fit function:

$$P(f; \sigma_{i\eta i\eta}) = f \cdot h_s(\sigma_{i\eta i\eta}) + (1 - f) \times h_b(\sigma_{i\eta i\eta}), \quad (6.2)$$

where  $h_s$  is the signal template,  $h_b$  is the background template, and  $f$  is the fraction of true photons in the target sample. Both the target template and the fit function are normalized to unity, removing the number of photon candidates in the target sample  $N$  as a fit parameter and leaving  $f$  as the only free parameter.

However, the hadronic background template, taken from the data control sample, has contributions from real photons with a  $I_{\text{CH}}$  value exceeding the ID requirements.

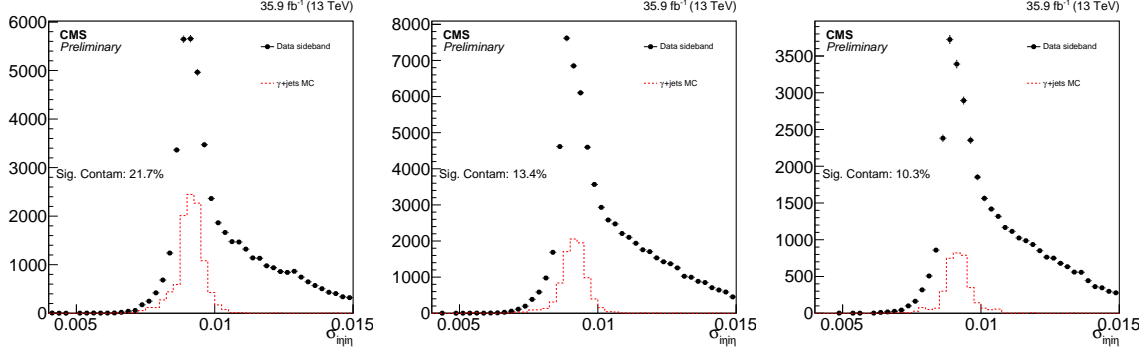


Figure 6-6: Signal contamination in the [3.5,5.0] (left), [5.0,7.5] (middle), and [7.5,9.0] (right) isolation sidebands.

The amount of this “photon contamination” depends on the sideband choice, but is non-zero even for a sideband with very large  $I_{\text{CH}}$ . As described below, we perform additional fits with the background templates from alternative sidebands  $3.5 \text{ GeV} < I_{\text{CH}} < 5 \text{ GeV}$  (“near”) and  $7.5 \text{ GeV} < I_{\text{CH}} < 9 \text{ GeV}$  (“far”) to assess the systematic uncertainty. The photon contamination of the nominal and far sideband is 10-15%, and in the near sideband, it can go up to approximately 20% (see Figure 6-6).

To remove the photon contamination from the background templates, we start with the true photon shape in the sideband  $h_{s'}$ , which differs from the signal template  $h_s$  in the  $I_{\text{CH}}$  selection applied to the photons. Then, we create a new background template  $h_b^{\text{sub}}$  from the original background template  $h_b$  by subtracting  $h_{s'}$ . After normalization to unity, we obtain the expression

$$h_b^{\text{sub}}(\sigma_{inj\eta}) = \frac{h_b(\sigma_{inj\eta}) - S'/B \cdot h_{s'}(\sigma_{inj\eta})}{1 - S'/B}, \quad (6.3)$$

where  $B$  is the number of photon candidates in the sideband and  $S'$  is the number of true photons in the sideband.

To determine  $S'$ , we start with the number of true photons in the target sample,  $f \cdot N$ . We then scale this by the ratio of the relative fractions of true MC photons in the  $I_{\text{CH}}$  sideband  $r_{\text{sb}}$  and in the signal region  $r_{\text{sig}}$ , giving us the expression

$$S' = f \cdot \frac{r_{\text{sb}}}{r_{\text{sig}}} \cdot N. \quad (6.4)$$

Going back to our original fit function and replacing  $h_b$  with  $h_b^{\text{sub}}$  gives us

$$P(f; \sigma_{i\eta i\eta}) = f \cdot h_s(\sigma_{i\eta i\eta}) + (1 - f) \times \frac{h_b(\sigma_{i\eta i\eta}) - S'(f)/B \cdot h_{s'}(\sigma_{i\eta i\eta})}{1 - S'(f)/B}, \quad (6.5)$$

which converges to the original fit function if  $S' = 0$ , i.e., if there is no photon contamination in the sideband. Note that  $f$  is still the only free parameter for this new function as  $S'$  only depends on  $f$  and  $r_{\text{sb}}/r_{\text{sig}}$  is set constant in the fit (see discussion of systematics for more detail).

There are four main sources of systematic uncertainty for this measurement. The first comes from the sideband choice, as the relative rates of different types of fake photons varies with  $I_{\text{CH}}$ . The second comes from the true photon  $I_{\text{CH}}$  shape, as this is used to determine the normalization of true photons in the sideband. Currently, this shape is taken from MC and thus there is the potential to mismodel the effects of the underlying event and pile-up. The third comes from the true photon  $\sigma_{i\eta i\eta}$  distribution. As we take this from MC as well, we can mismodel the signal template shape. Finally, at high  $p_T$ , we suffer from low yields in our  $I_{\text{CH}}$  sidebands, which leads fluctuations that negatively influence the fit.

The uncertainty due to sideband choice is the larger of the differences of the purities measured using the near and far sidebands versus the nominal sideband. Figure 6-7 shows fits using the three sidebands for the  $[175, 200]$   $p_T$  bin on the left and for the  $[400, \infty)$   $p_T$  bin on the right.

To measure the uncertainty due to the  $I_{\text{CH}}$  shape, we look at the  $I_{\text{CH}}$  for electrons in  $Z \rightarrow ee$  events in both data and MC. Using these distributions, we obtain a data/MC scale factor which we apply to the MC true photon  $I_{\text{CH}}$  distribution to obtain a scaled MC distribution. Then, we recount the photons using this new distribution and take the difference in the values obtained using the raw MC and scaled MC distributions as a systematic uncertainty.

To measure the uncertainty due to the signal template  $\sigma_{i\eta i\eta}$  shape, we look at the  $\sigma_{i\eta i\eta}$  distributions for electrons from  $Z \rightarrow ee$  events in both data and MC. Using these distributions, we obtain a data/MC scale factor which we apply to the MC true

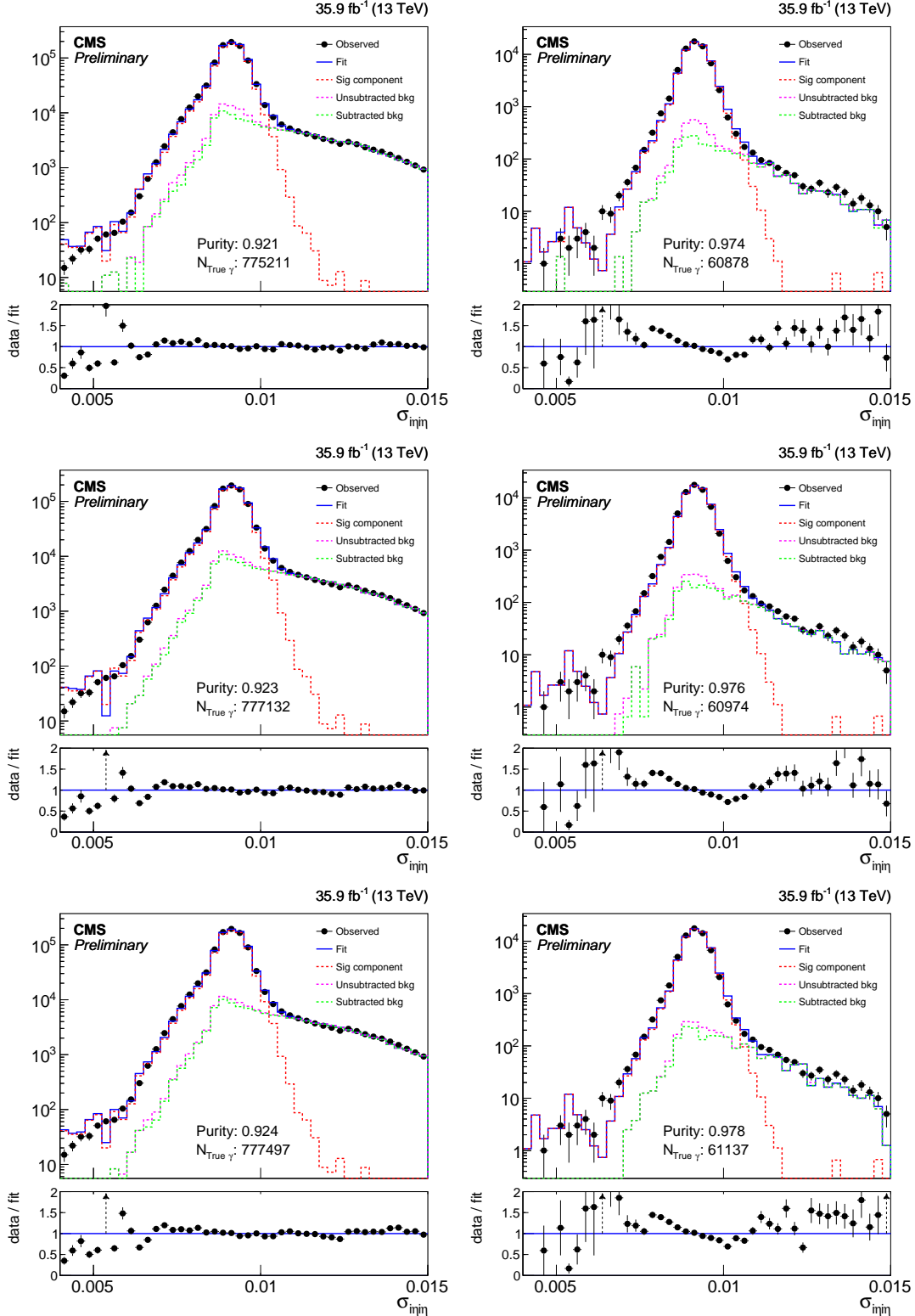


Figure 6-7: Fits to the  $\sigma_{\text{inn}}$  distributions for the  $[175, 200]$  (left) and  $[400, \infty)$  (right)  $p_T$  bins using the  $[3.5, 5.0]$  (top),  $[5.0, 7.5]$  (middle), and  $[7.5, 9.0]$  (bottom) isolation sidebands. The blue solid line represents the full fit model, the red dashed line its signal component, and the green dashed line its background component.

photon  $\sigma_{inj\eta}$  distribution to obtain a scaled MC distribution. Then, we recount the photons using this new distribution and take the difference in the values obtained using the raw MC and scaled MC distributions as a systematic uncertainty.

To estimate the uncertainty due to statistical fluctuations in our background templates, we generate toys from the background template from data. We then repeat the fit with each of these toys and plot the distribution of the difference between the purity value obtained from the toy templates versus the nominal template. We take the standard deviation of this distribution as a systematic uncertainty.

The values obtained for each systematic uncertainty on the true photon count of the denominator are shown in Table 6.4 in bins of  $p_T$ . The relative uncertainties on the numerator are similar, and in the efficiency, each uncertainty source is considered as fully correlated.

$p_T$ Range (GeV)	Sources of Systematic Uncertainty				
	Sideband	$I_{CH}$	Shape	Signal Shape	Bgkd. Stats
(175, 200)	0.09	0.18	0.05	0.04	
(200, 250)	0.01	0.16	0.06	0.03	
(250, 300)	0.14	0.16	0.06	0.05	
(300, 350)	0.12	0.16	0.07	0.08	
(350, 400)	0.23	0.11	0.05	0.10	
(400, $\infty$ )	0.27	0.09	0.05	0.05	

Table 6.4: Relative uncertainties on the estimated number of true photons in the denominator sample.

The MC efficiency of the  $\gamma$ -specific ID is determined by counting the number of truth-matched photons passing the  $e/\gamma$  part of the ID and the full ID. However, there is a complication, the  $\gamma+jets$  region in data has approximately 5% contamination from electrons before applying the pixel veto, as shown in Figure 6-8. To replicate this effect in the MC, we combine appropriately cross-section weighted  $\gamma+jets$ ,  $W+jets$ , and  $t\bar{t}$  samples and truth match to both electrons and photons. Additionally, to account for the NLO cross-section ratio uncertainties with respect to  $\gamma+jets$  at this  $p_T$  range, we apply a 14% uncertainty on the  $W+jets$  and  $t\bar{t}$  yields, where the specific value comes from the uncertainty on the  $\gamma+jets$  to  $W+jets$  ratio in the monojet analysis []. This uncertainty is uncorrelated between the numerator and denominator as a negligible

amount of electron events survive the pixel veto.

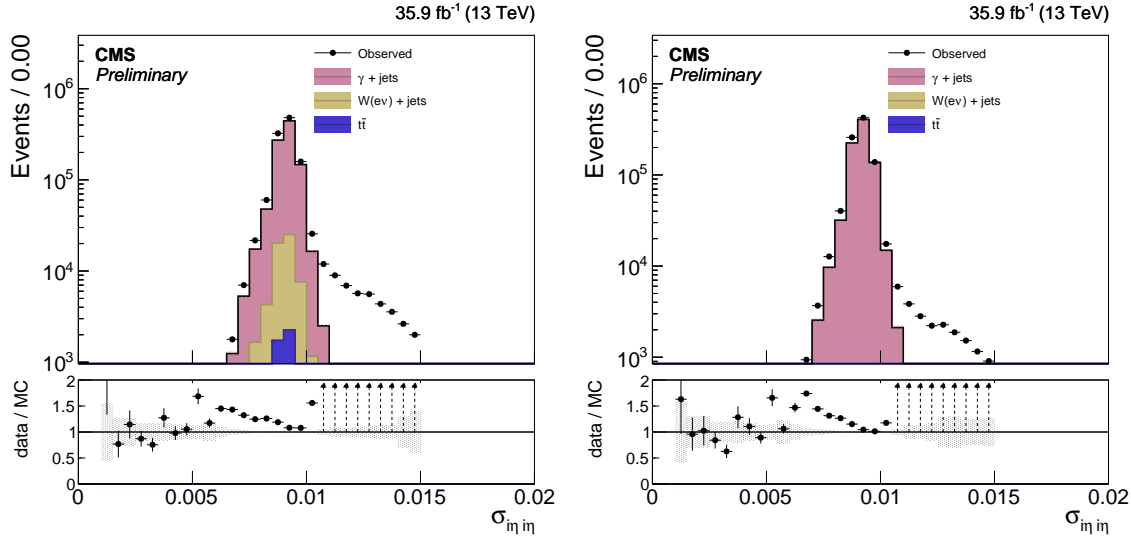


Figure 6-8: Electron contamination in  $\gamma$ +jets region before (left) and after (right) applying the pixel seed veto.

The data efficiency, MC efficiency, and the scale factor for the  $\gamma$ -specific ID as a function of  $p_T$  are shown in Figure 6-9. As there is no significant trend in the scale factor as a function of  $p_T$ , we apply a flat scale factor of  $0.9840 \pm 0.0090$  for all of the MC-based background and signal models in the analysis.

### 6.3.3 Lepton Veto Efficiency

The lepton veto requirement in the signal region has a non-unity efficiency over events that do not have genuine leptons, because particles such as pions and protons can mimic leptons to become “fake leptons” and cause the event to be rejected. To measure the possible difference between data and MC of this lepton veto efficiency, we compare dimuon events in data and MC. In a high-purity  $Z \rightarrow \mu\mu$  sample with the dimuon mass close to  $M_Z$ , events with a genuine third lepton is negligibly rare, and therefore the efficiency loss from rejecting events with a third lepton is dominantly due to fake leptons.

For this measurement, collision events are taken from the SingleMuon data set and the MC events from a mixture of Drell-Yan,  $t\bar{t}$ ,  $WW$ ,  $WZ$ , and  $ZZ$  samples.

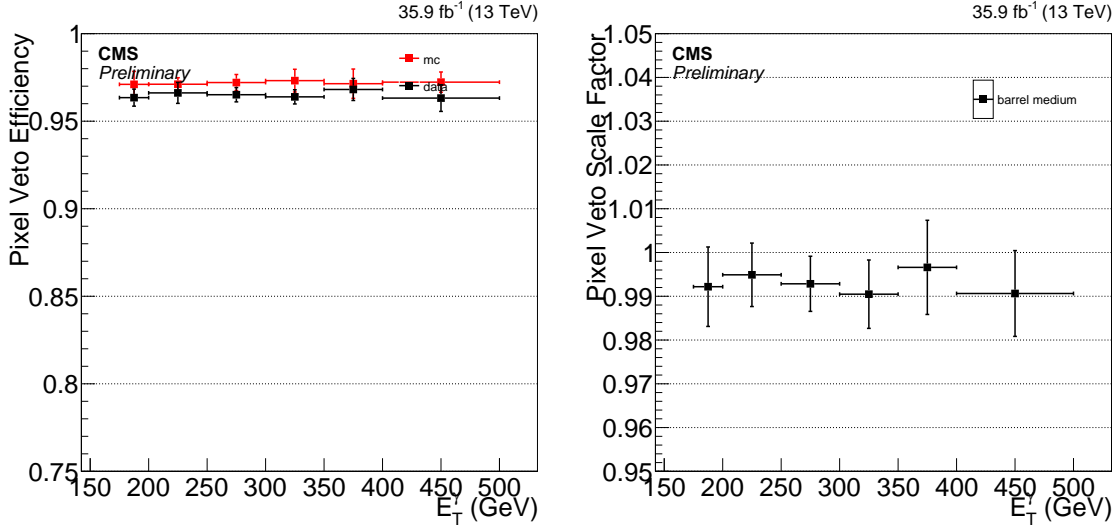


Figure 6-9: Photon pixel veto efficiencies (left) and corresponding scale factor (right) as a function of photon  $p_{\text{T}}$ .

We require two muons passing the “tight” identification working point defined with the mass between 61 and 121 GeV. The failing category consists of events containing an additional electron or muon object that passes the loose selection criteria while the passing category consists of those without an additional lepton. The efficiency is inspected as a function of number of vertices, number of jets, and  $H_{\text{T}}$  in the event, and in all cases data and MC are consistent as shown in Figure 6-10.

It should be noted, however, that the absolute lepton veto efficiency in MC dimuon sample is significantly different from that of the  $Z(\rightarrow \nu\bar{\nu})+\gamma$  sample, which more closely features the properties of the signal candidate sample. The full difference in the efficiencies between the dimuon and  $Z(\rightarrow \nu\bar{\nu})+\gamma$  samples is taken as the systematic uncertainty in the lepton veto scale factor, which is therefore  $1.00 \pm 0.02$ .

Additionally, a small fraction of events with real leptons pass the lepton veto due to the leptons failing the loose ID requirements. This effect is most relevant for  $W(\rightarrow \ell\nu)+\gamma$  events in the signal region and for  $Z(\rightarrow \ell\bar{\ell})+\gamma$  events in the single lepton control regions. We compute a scale factor  $\text{SF}_{\text{veto}} = (1. - \epsilon_{\text{data}})/(1. - \epsilon_{\text{MC}})$  using the data and MC efficiencies for the loose lepton IDs with a flat 1% uncertainty for the efficiencies. All scale factors are consistent with unity within the uncertainties.

This veto scale factor is applied to MC events with a reconstructed lepton that

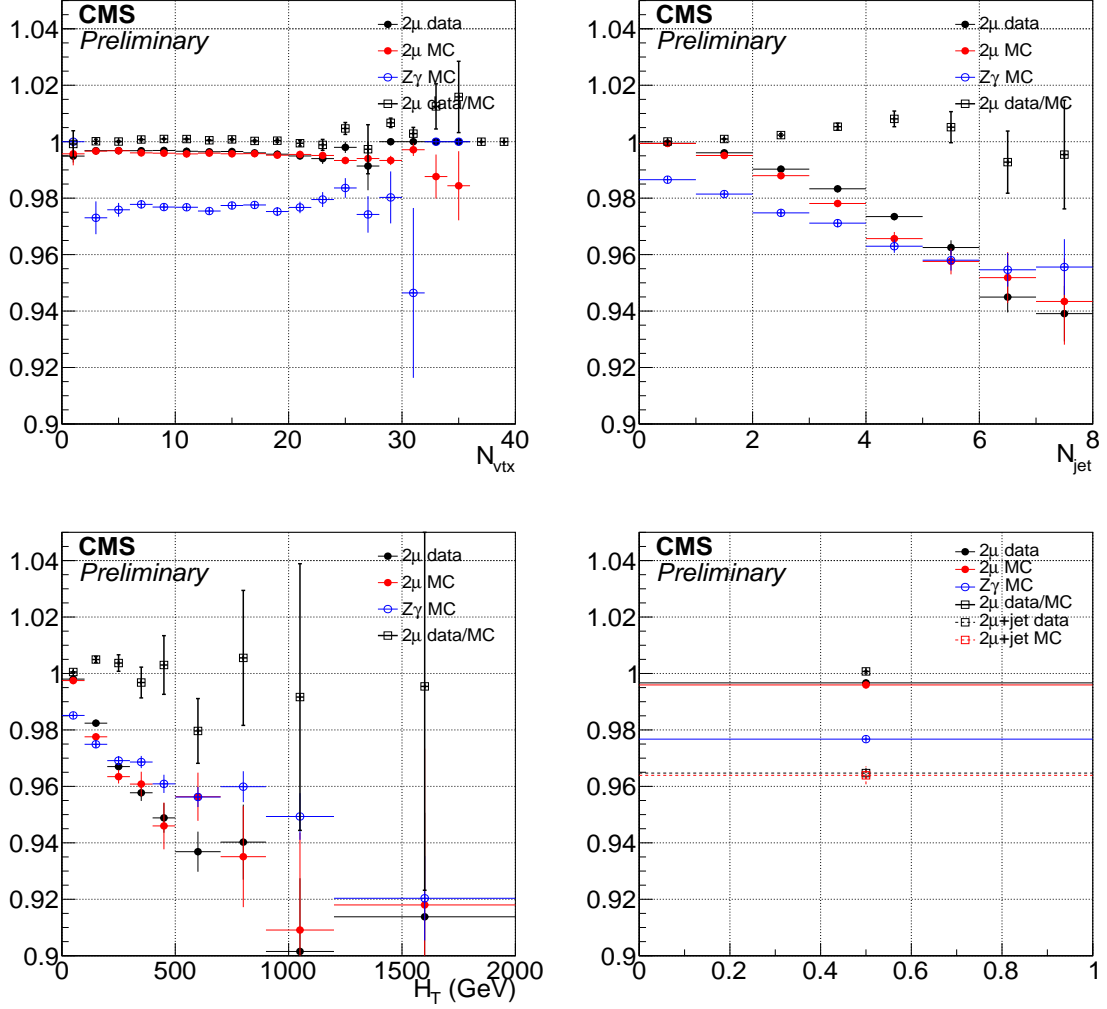


Figure 6-10: Lepton veto efficiencies and data/MC scale factors as functions of  $N_{\text{vtx}}$ ,  $N_{\text{jet}}$ , and  $H_T$ , and the corresponding inclusive values. While dimuon and  $Z(\rightarrow \nu\bar{\nu})+\gamma$  samples have significantly different efficiencies, data and MC agree well within dimuon samples, giving scale factors consistent with 1 almost everywhere. This is true even when additionally requiring a high- $p_T$  jet in the event, as seen in the inclusive efficiency plot. Thus, the difference between  $Z(\rightarrow \nu\bar{\nu})+\gamma$  and dimuon efficiencies itself is taken as the uncertainty.

fails the loose ID. If there are multiple such leptons in an event, we apply the scale factor only for the hardest muon and electron. After applying the scale factors, the final MC yields for  $W(\rightarrow \ell\nu)+\gamma$  in the signal region and  $Z(\rightarrow \ell\bar{\ell})+\gamma$  in the single lepton control regions change by less than 0.5%.

## 6.4 Misidentified electrons

An electron can be misidentified as a photon if the association of tracks or track seeds to the ECAL supercluster fails in the reconstruction step. The production of a single  $W$  boson decaying to an electron and a neutrino is a high-rate process, and it mimicks the photon plus  $E_T^{\text{miss}}$  signature if the electron is misidentified.

The rate at which this misidentification occurs is  $R_e = (1 - \epsilon_e^{\text{track}})/\epsilon_e^{\text{track}}$ , where  $\epsilon_e^{\text{track}}$  is the tracking efficiency of electrons passing the photon identification criteria except for the electron veto. After making the reasonable assumption that the kinematic and other critical properties of the electron plus  $E_T^{\text{miss}}$  events are unaffected by the electron misidentification, we model the electron misidentification background by taking the electron proxy sample and scaling it by  $R_e$ .

We measure the factor  $R_e$  in data using the TP method described in Section 6.3.1 with changed definitions for passing and failing probes and an adjustment to the background model. The  $ee$  category contains passing probes with a pixel seed while the  $e\gamma$  category contrains failing probes without a pixel seed. Probes in both categories must pass the remainder of the  $e/\gamma$  and  $\gamma$ -specific IDs. Denoting the area of the peak in each category  $N_{ee}$  and  $N_{e\gamma}$ , respectively, the ratio  $N_{e\gamma}/N_{ee}$  is equal to  $R_e$  up to minor systematic corrections.

Additionally, the backgrounds to the  $e\gamma$  fit consist of processes with an electron and an actual photon in the final state, such as  $W\gamma$  and  $Z \rightarrow ee$  with a hard radiation off one of the electrons. To account for the higher rate of bremsstrahlung experienced by electrons than by muons, we scale the mass distribution of the  $\mu + \gamma$  sample by the ratio of electron-probe to muon-probe events taken from MC. As an alternative template to assess the systematic effect introduced by the choice of the background

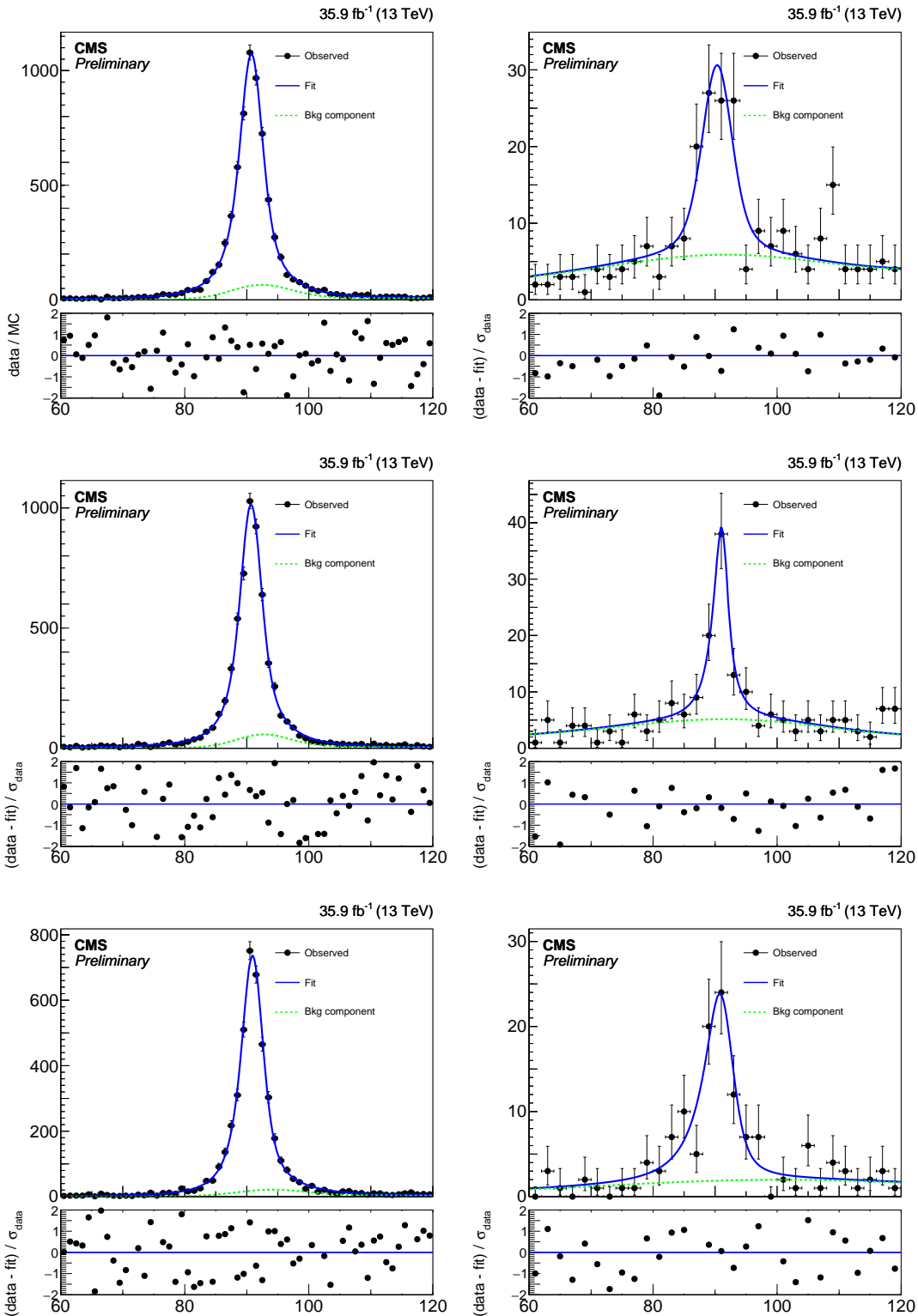


Figure 6-11: Fits to the mass distributions for  $ee$  (left) and  $e\gamma$  (right) selections, in bins of probe  $p_T$ :  $175 < p_T < 200 \text{ GeV}$  (top),  $200 < p_T < 250 \text{ GeV}$  (middle),  $p_T > 250 \text{ GeV}$  (bottom). The blue solid line represents the full fit model, and the green dashed line its background component.

template, the unscaled mass distribution is also tested.

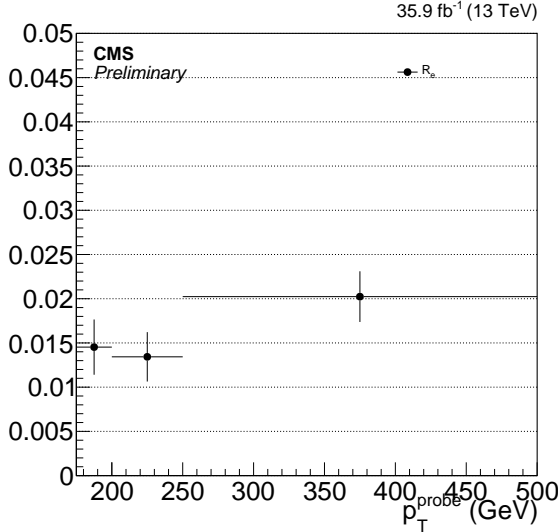


Figure 6-12: Electron to photon fake rate  $R_e$ .

Figure 6-11 shows the six fits performed on  $ee$  and  $e\gamma$  in bins of probe  $p_T$ , from which the  $R_e$  factor used for the estimation of the electron misidentification background is derived. Figure 6-12 shows the derived  $R_e$  factor as a function of  $E_T^\gamma$ . The electron proxy sample is reweighted by  $R_e$  depending on the  $p_T$  of the electron proxy object.

## 6.5 Misidentified hadrons

A hadron can be misidentified as a photon if fragmentation processes results in mainly neutral hadrons that subsequently decay to collimated pairs of photons. The production of  $Z + \text{jets}$  where the  $Z$  boson decays to neutrinos is a high-rate process, and it mimicks the photon plus  $E_T^{\text{miss}}$  signature if the hadrons from the jet are misidentified.

Without the presence of additional charged tracks or neutral hadron energy deposits, the only way to distinguish these EM-like hadrons from real photons is through the shower shape. Thus, we measure the fraction of hadronic objects within a pool of photon candidate objects in the EM object+jet measurement sample using the  $\sigma_{inj}$  template fit method from Section 6.3.2. Figure 6-13 and Table 6.5 show the final

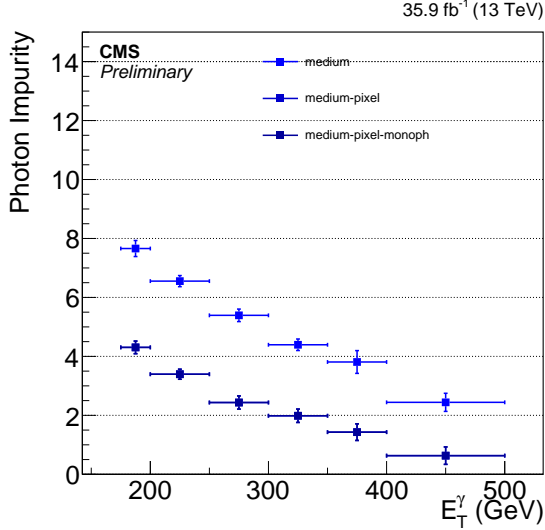


Figure 6-13: The percent impurity for photons as a function of  $p_{\text{T}}$ . The different bands show the effects of adding different stages of the full ID, starting with the  $e/\gamma$  portion of the ID and successively adding the pixel seed veto followed by the rest of the  $\gamma$ -specific portion of the ID. These last two curves overlap, as the non-collision rejection cuts do not effect the rate at which hadrons are misidentified as photons.

impurity and associated uncertainties as a function of  $p_{\text{T}}$ .

$p_{\text{T}}$ (GeV)	Nominal	Sources of Systematic Uncertainty				
		Sideband	CH	Iso	Shape	Bgkd. Stats
(175, 200)	$4.31 \pm 0.21$	0.09	0.18	0.05		0.04
(200, 250)	$3.39 \pm 0.17$	0.01	0.16	0.06		0.03
(250, 300)	$2.44 \pm 0.22$	0.14	0.16	0.06		0.05
(300, 350)	$1.99 \pm 0.23$	0.12	0.16	0.07		0.08
(350, 400)	$1.43 \pm 0.28$	0.23	0.11	0.05		0.10
(400, $\infty$ )	$0.63 \pm 0.30$	0.27	0.09	0.05		0.05

Table 6.5: Impurities for photons as a function of  $p_{\text{T}}$ .

The hadronic transfer factor  $R_h$  measures the rate at which hadronic proxy objects result in hadrons that are misidentified as candidate photons. The factor  $R_h$  is obtained by dividing the estimated number of misidentified hadrons in the EM object+jet measurement sample by the number of events in the hadron proxy+jet measurement sample as a function of  $p_{\text{T}}$ . Figure 6-14 shows the transfer factor  $R_h$  along with the various distributions used for its derivation.

Under the assumption that the  $R_h$  stays constant regardless of whether the event

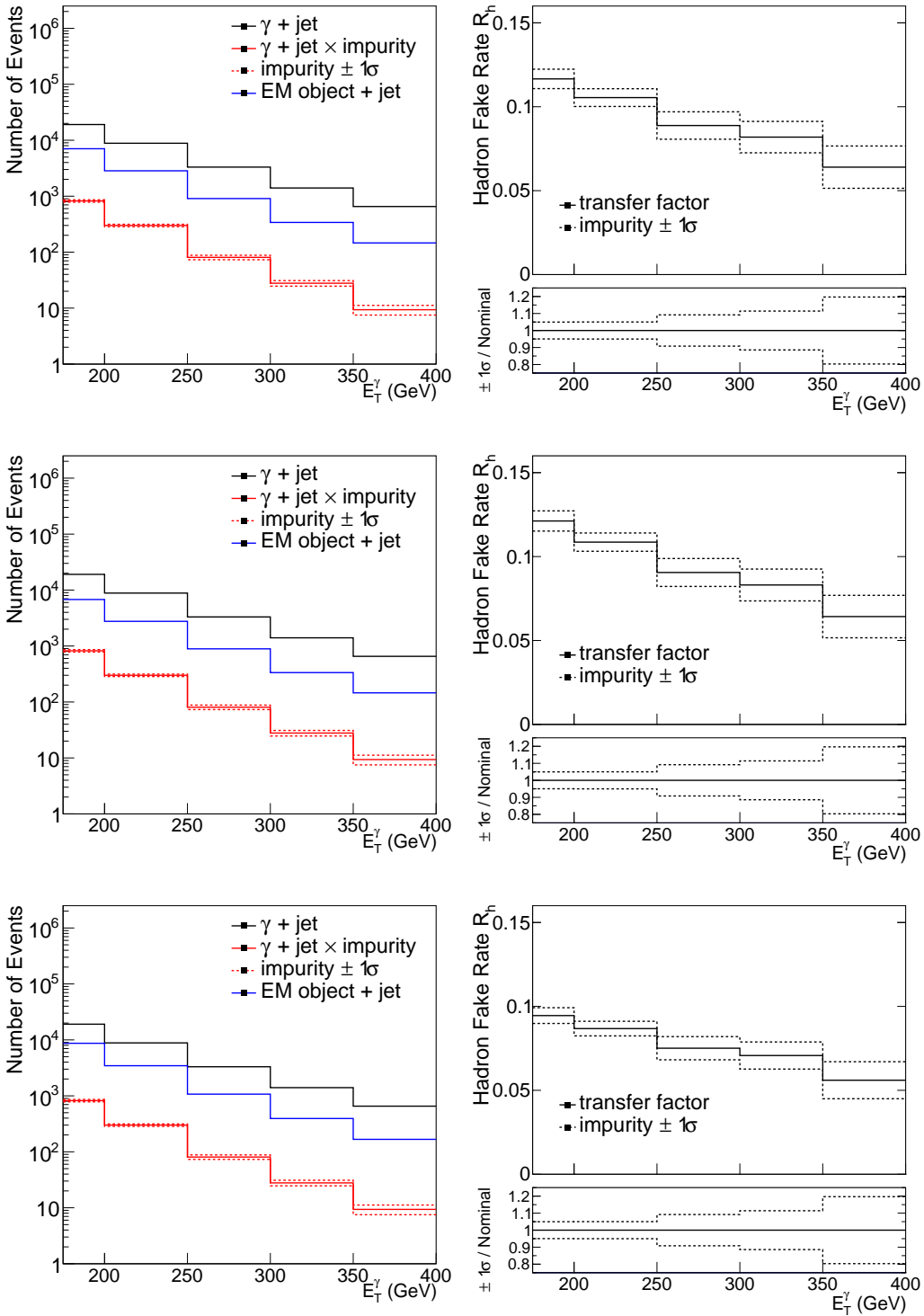


Figure 6-14: Left: The  $p_T$  distribution of the candidate photon object in the photon + jet control sample (black), the result of scaling it with the impurity (red), and the  $p_T$  distribution of the hadronic proxy object in the proxy + jet control sample (blue). Right: Hadronic transfer factor  $R_h$ , which is the ratio of the red and blue distributions in the left plot. Top: Nominal hadron proxy object. Middle: Tighter hadron proxy object. Bottom: Looser hadron proxy object.

has a high- $p_T$  jet or  $E_T^{\text{miss}}$ , the hadron proxy sample is weighted by  $R_h$  to determine the number of events due to misidentified hadrons in the signal region.

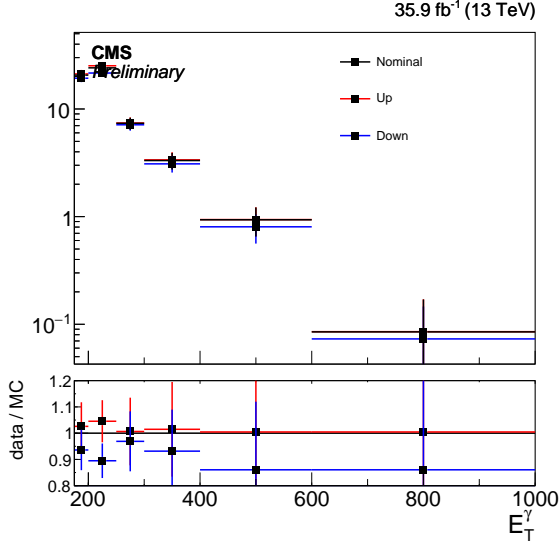


Figure 6-15: The  $p_T$  distribution of the estimated contribution from hadronic fakes in the signal region. The distribution labeled Up (Down) comes from the tighter (looser) selection. The systematic uncertainty resulting from this variation is around 5% at the low end of our  $p_T$  range and increases to 15% after  $p_T > 400$  GeV.

To estimate the uncertainty on this background, we repeat the above method using additional proxy and measurement samples with tighter and looser definitions of the hadron proxy object. The different distributions from the nominal, tight, and loose selections are shown in Figure 6-15. The tight and loose shapes are taken as the one sigma band around the nominal estimate. Additionally, there is an uncertainty coming from the estimation of the photon purity, with values given in Table 6.5.

## 6.6 Irreducible backgrounds

### 6.6.1 Simulation of V+γ Processes

The  $Z(\rightarrow \nu\bar{\nu})+\gamma$  and  $W(\rightarrow \ell\nu)+\gamma$  background contributions are modeled using MC simulations. Samples generated at the leading order (LO) in QCD by MADGRAPH 5 with up to two additional partons and a generator-level requirement of  $E_T^\gamma > 130$  GeV are employed for this purpose.

A study using an aMC@NLO sample with high  $E_T^\gamma$  threshold confirms that the predicted kinematic distributions would not change drastically by using the NLO sample. Figures 6-16 and 6-17 show the comparisons of the aMC@NLO samples<sup>1</sup> and the MADGRAPH 5 samples used for the background estimation in the key kinematic distributions.

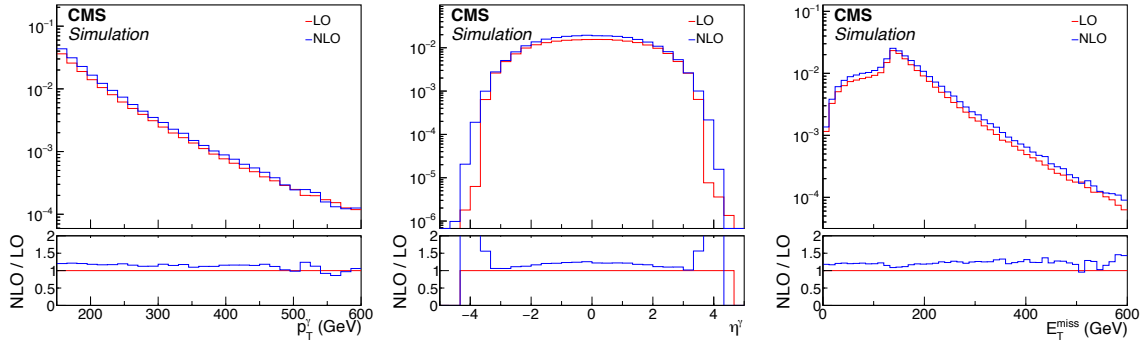


Figure 6-16: Distributions of  $E_T^\gamma$  (left),  $\eta^\gamma$  (middle), and  $p_T^Z$  (right) in  $Z(\rightarrow \nu\bar{\nu}) + \gamma$  process from the private aMC@NLO sample (blue) and the LO sample used for background prediction (red) along with the NLO / LO ratios.

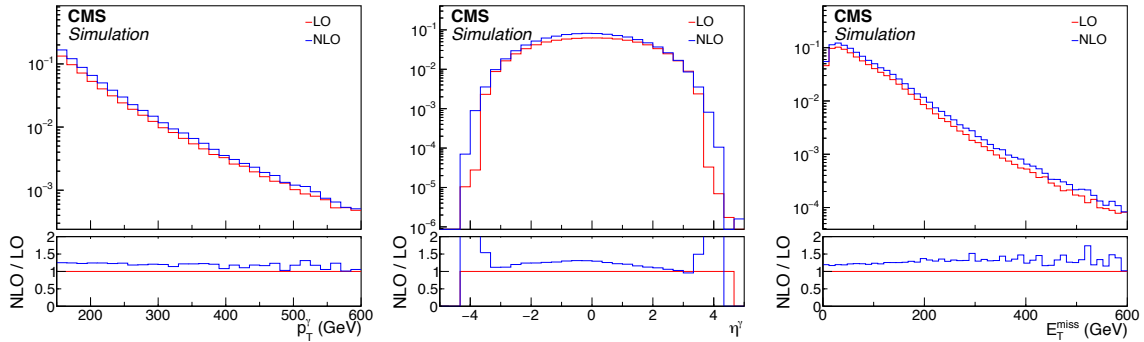


Figure 6-17: Distributions of  $E_T^\gamma$  (top left),  $\eta^\gamma$  (top right), and  $p_T^W$  (bottom left) in  $W(\rightarrow \ell\nu) + \gamma$  process from the private aMC@NLO sample (blue) and the LO sample used for background prediction (red) along with the NLO / LO ratios.

To approximate the QCD higher-order effects,  $Z(\rightarrow \nu\bar{\nu}) + \gamma$  and  $W(\rightarrow \ell\nu) + \gamma$  events are reweighted with  $E_T^\gamma$  by the factors given in Tab. 6.6. These factors are the ratios of QCD next-to-next-to leading order (NNLO) differential cross sections calculated by Grazzini et al. [83] to the LO cross sections given in the centrally

<sup>1</sup>These samples were privately produced.

produced samples. Note that the denominator cross section includes contributions from processes with up to two additional partons, and is therefore not a LO cross section in the strict sense of the word.  $V\gamma$  k-factors found in literature are  $\gg 1$  at high  $E_T^\gamma$ , if the denominator only accounts for the cross section of  $q\bar{q} \rightarrow V\gamma$  process.

$E_T^\gamma$ range (GeV)	$Z(\rightarrow \nu\bar{\nu}) + \gamma$	$W(\rightarrow \ell\nu) + \gamma$
[175, 190]	1.44	1.40
[190, 250]	1.41	1.37
[250, 400]	1.35	1.31
[400, 700]	1.29	1.26
[700, $\infty$ )	1.15	1.15

Table 6.6: Correction factors  $k_{\text{QCD}}^{\text{NNLO}}$  for  $Z(\rightarrow \nu\bar{\nu}) + \gamma$  and  $W(\rightarrow \ell\nu) + \gamma$  samples.

Higher-order electroweak correction factors are also applied as a function of  $E_T^\gamma$ . Out of various electroweak higher-order effects, ones that can give sizeable ( $\gg \mathcal{O}(\alpha)$ ) corrections to the cross section are the Sudakov suppression at high boson  $p_T$  and potentially the addition of photon-induced scattering processes [84, 85]. We apply the correction factors shown in Figure 6-18, which are the combinations of Sudakov suppression factors and photon-induced enhancements, and are provided by the authors of Reference [85] in addition to the NNLO QCD correction.

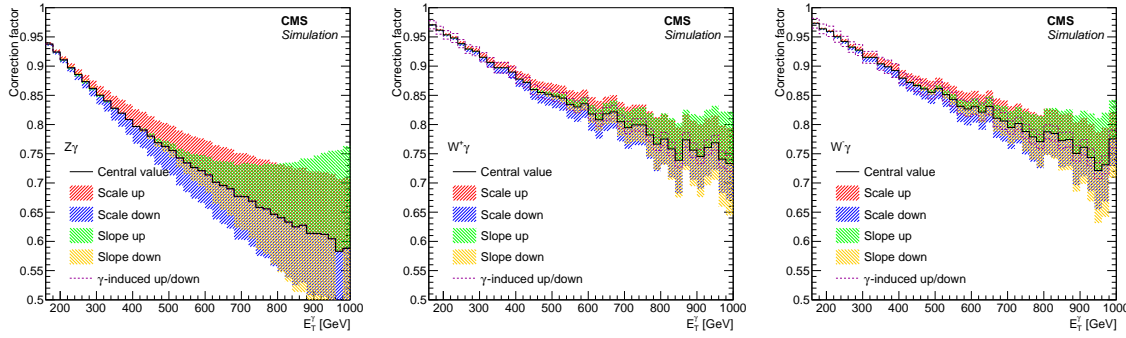


Figure 6-18: Electroweak NLO cross section corrections as a function of photon  $p_T$  for  $Z(\rightarrow \nu\bar{\nu}) + \gamma$  (left),  $W^+ + \gamma$  (middle), and  $W^- + \gamma$  (right) processes, overlaid with uncertainty bands. See text for descriptions of the individual components of the uncertainty. The uncertainty due to  $\gamma$ -induced production is negligible in  $Z(\rightarrow \nu\bar{\nu}) + \gamma$  production.

The differential cross section after the full higher-order corrections is

$$d\sigma_{\text{QCD}}^{\text{LO}} \cdot k_{\text{QCD}}^{\text{NNLO}} \cdot (1 + k_{\text{EW}}^{\text{Sudakov}} + k_{\text{EW}}^{q\gamma}) , \quad (6.6)$$

where  $k_{\text{QCD}}^{\text{NNLO}} = d\sigma_{\text{QCD}}^{\text{NNLO}}/d\sigma_{\text{QCD}}^{\text{LO}}$ , and the two  $k_{\text{EW}}$  terms are the Sudakov suppression and photon-induced enhancement components of the electroweak correction, respectively.

Furthermore, subtle differences between simulation and observation in the reconstruction and identification efficiencies for various particle candidates are accounted for with the set of selection efficiency correction factors  $\rho$ . The value of an individual  $\rho$  typically lies within a few percent of unity.

Four sources of systematic uncertainties considered for  $E_{\text{T}}^{\gamma}$  distribution ratios of the  $V+\gamma$  processes are higher-order QCD corrections, higher-order EWK corrections, choice of PDF set, and data-to-simulation correction factors  $\rho$ . The four uncertainties are evaluated for each  $E_{\text{T}}^{\gamma}$  bin and fully correlated between the different bins..

The higher-order QCD renormalization and factorization scale uncertainties on the NNLO cross sections are assessed by varying the respective scales by factors 2 and 0.5 during the cross section computation. The uncertainties vary between 7-8% across the bins and are considered uncorrelated in the ratio between the  $Z(\rightarrow \nu\bar{\nu})+\gamma$  and  $W(\rightarrow \ell\nu)+\gamma$  processes.

Theoretical uncertainties on the electroweak corrections are not well understood to date for  $V\gamma$  processes. Our treatment of them is informed by discussions with the authors of Reference [86], which provides a prescription for electroweak correction uncertainties for  $V+\text{jets}$  processes. We estimate the magnitude of the uncertainty on  $k_{\text{EW}}^{\text{Sudakov}}$  and  $k_{\text{EW}}^{q\gamma}$  to be  $(k_{\text{EW}}^{\text{Sudakov}})^2$  and  $k_{\text{EW}}^{q\gamma}$ , i.e., square of the correction for Sudakov suppression and the 100% of the correction itself for the photon-induced enhancement. The choice of using the square of  $k_{\text{EW}}^{\text{Sudakov}}$  is motivated by the fact that fully resummed leading-log Sudakov suppression is an exponential of  $k_{\text{EW}}^{\text{Sudakov}}$ .

For the Sudakov suppression, which is the dominant term in the electroweak correction, we further consider two types of systematic variations. In this paper, elec-

Electroweak correction as a function of the boson  $p_T$  is varied in overall scale and in slope. The slope variation is realized by selecting a point in the boson  $p_T$  spectrum and letting the shift in correction cross over at the point (see Figure 6-19). Following this prescription, we let the Sudakov suppression vary in overall scale and in slope, where we choose our crossover point for the slope variation to be at  $E_T^\gamma = 590 \text{ GeV}$ .

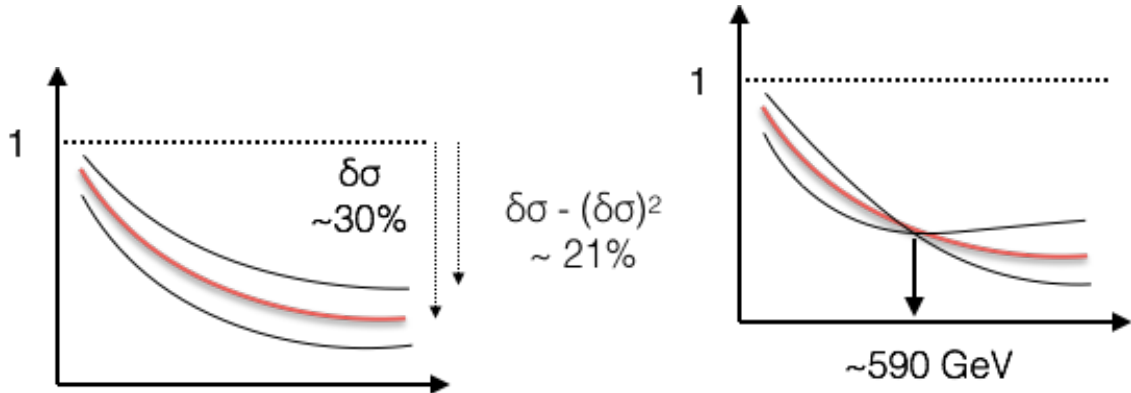


Figure 6-19: Electroweak correction variation scheme to cover the scale (left) and shape (right) uncertainties.

The PDF uncertainty is evaluated by varying the weight of each event using the weights provided in the NNPDF set, and taking the standard deviation of the resulting  $E_T^\gamma$  distributions. This uncertainty is considered fully correlated in the ratio between the  $Z(\rightarrow \nu\bar{\nu}) + \gamma$  and  $W(\rightarrow \ell\nu) + \gamma$  processes, i.e., the variation of the ratio is bounded by the ratios formed by the simultaneous upward and downward variations of the numerator and denominator. .

Finally, data-to-simulation correction factors  $\rho$  for the lepton identification efficiencies have associated uncertainties that do not cancel when taking ratios between regions defined by different lepton selection requirements. The lepton efficiencies are measured using the “tag-and-probe” method where the tag object is an electron (muon) object passing the tight ID and matched to a SingleElectron (SingleMuon) trigger and the probe object is a PF electron (muon) without any ID applied. The passing (failing) categories are defined by events with probes passing (failing) the ID definition in question. The electron (muon) scale factors  $\rho$  are approximately unity with a flat 2% (1%) systematic uncertainty.

## 6.6.2 Data-driven Control Regions

Contributions from the  $Z(\rightarrow \nu\bar{\nu})+\gamma$  and  $W(\rightarrow \ell\nu)+\gamma$  processes are estimated using observed data in four mutually exclusive single-electron, single-muon, dielectron, and dimuon control regions. The various ratios between the expected  $Z(\rightarrow \nu\bar{\nu})+\gamma$  yield in the combined signal regions and the expected  $W(\rightarrow \ell\nu)+\gamma$  and  $Z(\rightarrow \ell\bar{\ell})+\gamma$  yields in the control region are constrained by MC simulations. When a ratio is calculated using MC samples as a function of  $E_T^\gamma$ , it is referred to as the “transfer factor” between the two processes. This background estimation method exploits the cancellation of some of the systematic uncertainties, both experimental and theoretical, in the transfer factors between the different  $V+\gamma$  processes.

For the transfer factor  $R_{\ell\ell\gamma}^{Z\gamma}$ , the numerator is the expected  $Z(\rightarrow \nu\bar{\nu})+\gamma$  yield in the combined signal regions and the denominator is the expected  $Z(\rightarrow \ell\bar{\ell})+\gamma$  yield in the relevant dilepton control region. The uncertainties due to photon energy calibration, jet energy resolution, and higher-order QCD effects are significantly reduced on  $R_{\ell\ell\gamma}^{Z\gamma}$  compared to when such effects are considered for individual processes. The only uncertainties in the transfer factor  $R_{\ell\ell\gamma}^{Z\gamma}$  that do not largely cancel are those on lepton identification efficiency, the statistical uncertainty due to the limited MC sample size, and a minor uncertainty due to the different acceptances between the  $Z(\rightarrow \nu\bar{\nu})+\gamma$  and  $Z(\rightarrow \ell\bar{\ell})+\gamma$  processes. Figure 6-20 shows the transfer factor  $R_{ee\gamma}^{Z\gamma}$  ( $R_{\mu\mu\gamma}^{Z\gamma}$ ) between the dielectron (dimuon) control region and the combined signal regions.

For increasing  $E_T^\gamma$ , the  $Z$  boson in a  $Z(\rightarrow \ell\bar{\ell})+\gamma$  event tends to emerge with lower rapidity, and hence so do its decay products. As a consequence, the charged leptons are more likely to fall within the inner tracker acceptance, which increases the dilepton control region selection efficiency of these events. In contrast, the signal region selection efficiency of  $Z(\rightarrow \nu\bar{\nu})+\gamma$  events is unaffected by the rapidity of the final state neutrinos, as long as the observed  $E_T^{\text{miss}}$  has the appropriate magnitude and azimuthal direction. This causes the distinctive drop in the ratio  $R_{\ell\ell\gamma}^{Z\gamma}$  with increasing  $E_T^\gamma$ .

Using the transfer factor  $R_{\ell\ell\gamma}^{Z\gamma}$ , the total estimated event yield  $T_{\ell\ell\gamma}$  in each dilepton

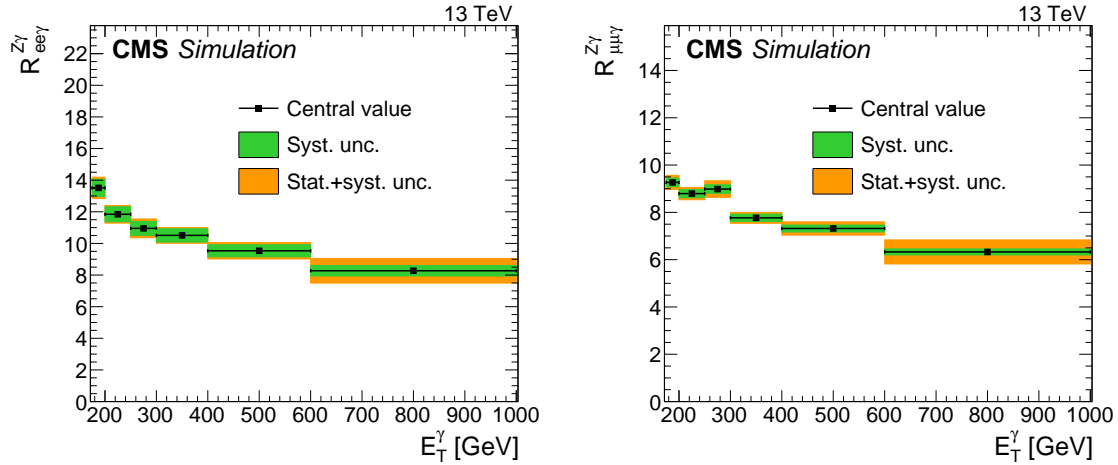


Figure 6-20: Transfer factors  $R_{ee\gamma}^{Z\gamma}$  (left) and  $R_{\mu\mu\gamma}^{Z\gamma}$  (right). The numerator is the expected  $Z(\rightarrow \nu\bar{\nu})+\gamma$  yield in the combined signal regions and the denominator is the expected  $Z(\rightarrow \ell\bar{\ell})+\gamma$  yield in the dielectron (left) or dimuon (right) control region. The uncertainty bands in green (inner) and orange (outer) show the systematic uncertainty, and the combination of systematic and statistical uncertainty arising from limited MC sample size, respectively. The systematic uncertainties considered are the uncertainties in the data-to-simulation correction factors  $\rho$  for the lepton identification efficiencies.

control region in the  $i^{\text{th}}$  bin of the  $E_T^\gamma$  distribution is given by

$$T_{\ell\ell\gamma,i} = \frac{N_i^{Z\gamma}}{R_{\ell\ell\gamma,i}^{Z\gamma}} + b_{\ell\ell\gamma,i}, \quad (6.7)$$

where  $N^{Z\gamma}$  is the predicted number of  $Z(\rightarrow \nu\bar{\nu})+\gamma$  events in the combined signal regions and  $b_{\ell\ell\gamma}$  is the predicted contribution from other background sources in the dilepton control region, namely  $t\bar{t}\gamma$ ,  $VV\gamma$ , and misidentified hadrons. The subscript  $i$  indicates that the quantities are evaluated in bin  $i$  of the  $E_T^\gamma$  distribution.

Similar considerations apply to events arising from the  $W(\rightarrow \ell\nu)+\gamma$  process. A large fraction of such events are rejected by the electron and muon vetoes in the signal region selection and end up in the control regions instead. However, hadronic tau events and events where the leptons are out of acceptance or fail to be reconstructed will remain in the signal region, on top of the vetoes having imperfect efficiencies. In the ratio of these two classes of events, denoted  $R_{\ell\gamma}^{W\gamma}$ , the only uncertainties that remain non-negligible are those associated with the lepton identification efficiency

and the MC statistical uncertainty.

Table 6.7 gives the breakdown of the  $W(\rightarrow \ell\nu) + \gamma$  background passing the full event selection for the signal region, categorized by the lepton flavor and, for the case of electrons and muons, the lepton pseudorapidity at the parton-level. From this breakdown, one sees that events where the  $W$  boson decays to a  $\tau$  and a neutrino constitute approximately 60% of the  $W(\rightarrow \ell\nu) + \gamma$  background. The remaining 40% of the  $W(\rightarrow \ell\nu) + \gamma$  background comes from events where the  $W$  boson decays to a  $\mu$  or  $e$  and a neutrino. Events containing an electron are more likely to be within the detector acceptance, while those with a muon are more likely to be out of acceptance. For the in-acceptance background ( $|\eta| < 2.5$ ), the identification efficiency, which is lower for electrons than for muons, which translates to a larger background contribution from the electrons. The requirement for large  $E_T^{\text{miss}}$  removes events with out-of-acceptance electrons because the energy from these electrons is captured by the calorimeters and retains events with out-of-acceptance muons because they contribute directly to the missing momentum. The overall result is a larger background contribution from events with out-of-acceptance muons than from events with out-of-acceptance electrons.

Subprocess	$A \times \epsilon \times 10^3$
$W \rightarrow e\nu + \gamma$	1.68
$ \eta^e  < 2.5$	1.35
$ \eta^e  > 2.5$	0.32
$W \rightarrow \mu\nu + \gamma$	1.83
$ \eta^\mu  < 2.5$	0.74
$ \eta^\mu  > 2.5$	1.08
$W \rightarrow \tau\nu + \gamma$	5.03

Table 6.7: The breakdown of simulated  $W + \gamma$  events passing the full event selection. Events are categorized in the  $W$  decay mode. Events with  $e\nu$  and  $\mu\nu$  final states are further divided into those where the lepton is roughly within acceptance ( $|\eta| < 2.5$ ) but failed the lepton veto, and those where the lepton is out of acceptance ( $|\eta| > 2.5$ ). For each  $W$  decay mode, the fraction out of total generated ( $A \times \epsilon$ ) is shown.

Figure 6-21 shows the transfer factor  $R_{e\gamma}^{W\gamma}$  ( $R_{\mu\gamma}^{W\gamma}$ ) between the single-electron (single-muon) control region and the combined signal regions, for which the numerator is the estimated  $W(\rightarrow \ell\nu) + \gamma$  yield in the combined signal regions, and the

denominator is the estimated  $W(\rightarrow \ell\nu)+\gamma$  yield in the relevant control region. The ratio  $R_{e\gamma}^{W\gamma}$  decreases with increasing  $E_T^\gamma$  in a similar manner to  $R_{\ell\ell\gamma}^{Z\gamma}$ . The underlying logic is the same; e.g., that the signal region selection efficiency is unaffected by  $E_T^\gamma$  while the control region acceptances increase with increasing  $E_T^\gamma$  due to increased lepton efficiency resulting from lower  $W$  rapidity.

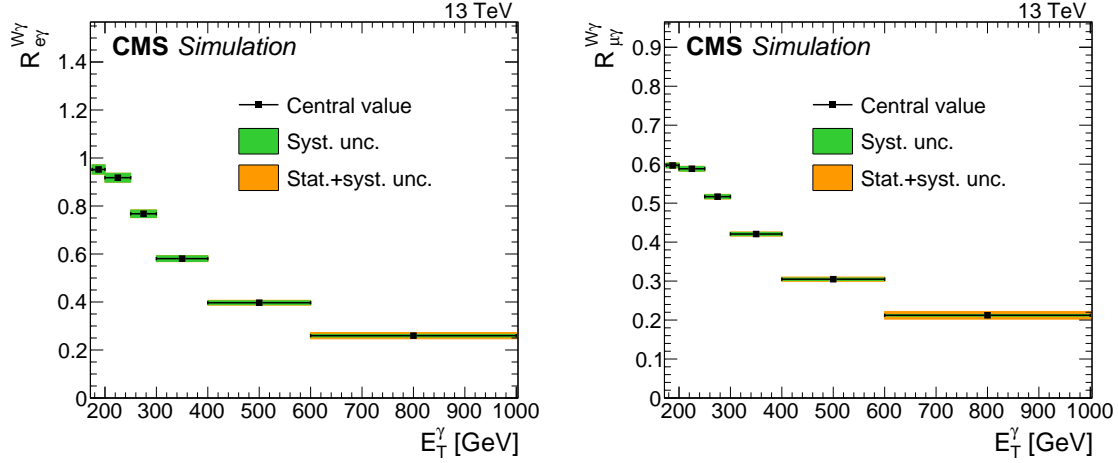


Figure 6-21: Transfer factors  $R_{e\gamma}^{W\gamma}$  (left) and  $R_{\mu\gamma}^{W\gamma}$  (right). The numerator is the expected  $Z(\rightarrow \nu\bar{\nu})+\gamma$  yield in the combined signal regions and the denominator is the expected  $W(\rightarrow \ell\nu)+\gamma$  yield in the mono-electron (left) or mono-muon (right) control region. The uncertainty bands in green (inner) and orange (outer) show the systematic uncertainty, and the combination of systematic and statistical uncertainty arising from limited MC sample size, respectively. The systematic uncertainties considered are the uncertainties in the data-to-simulation correction factors  $\rho$  for the lepton identification efficiencies.

Finally, to benefit further from the larger statistical power that the single-lepton control samples provides, an additional transfer factor  $f_{W\gamma}^{Z\gamma} = N^{Z\gamma}/N^{W\gamma}$  is defined to connect the  $Z(\rightarrow \nu\bar{\nu})+\gamma$  and  $W(\rightarrow \ell\nu)+\gamma$  background yields in the signal regions, where the quantity  $N^{W\gamma}$  is the number of  $W(\rightarrow \ell\nu)+\gamma$  events in the combined signal regions. When calculating the ratio  $f_{W\gamma}^{Z\gamma}$ , all experimental uncertainties associated with the data-to-simulation correction factors  $\rho$  cancel since both processes result in very similar event configurations. The main uncertainties in  $f_{W\gamma}^{Z\gamma}$  are those from higher-order theoretical corrections, discussed in Section 6.6.1. Figure 6-22 shows the effect of each systematic uncertainty in  $f_{W\gamma}^{Z\gamma}$  with respects to its nominal value for

$Z(\rightarrow \nu\bar{\nu})+\gamma$  and  $W(\rightarrow \ell\nu)+\gamma$ , respectively.

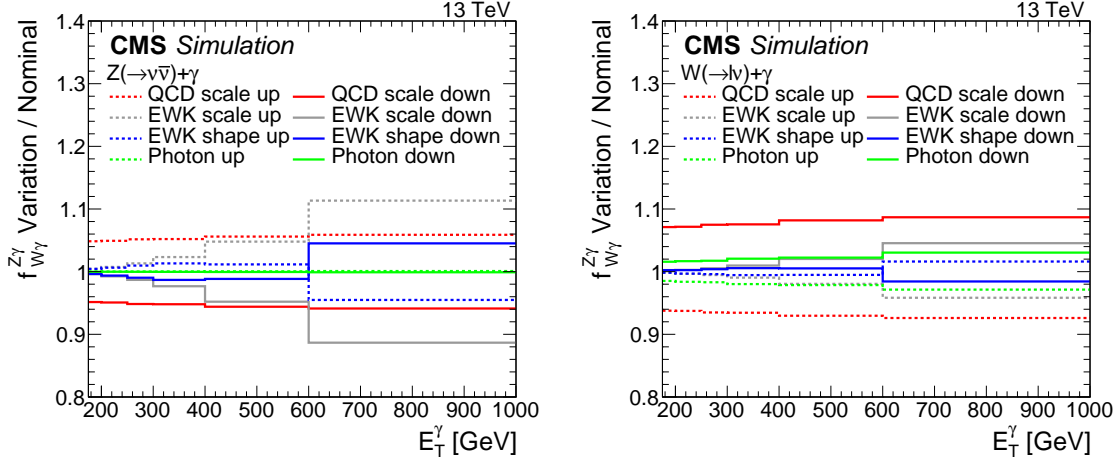


Figure 6-22: Systematic uncertainty in the transfer factors for  $Z(\rightarrow \nu\bar{\nu})+\gamma$  (left) and  $W(\rightarrow \ell\nu)+\gamma$  (right). The last bin includes all events with  $E_T^\gamma > 1000$  GeV.

The ratio  $f_{W\gamma}^{Z\gamma}$  rises rather than falls with increasing  $E_T^\gamma$  because  $W(\rightarrow \ell\nu)+\gamma$  events have a lower signal region selection efficiency when the charged lepton falls within the tracker acceptance due to the lepton veto while the  $Z(\rightarrow \nu\bar{\nu})+\gamma$  efficiency is independent of  $E_T^\gamma$ . Figure 6-23 shows the transfer factor  $f_{W\gamma}^{Z\gamma}$  between the  $Z(\rightarrow \nu\bar{\nu})+\gamma$  and  $W(\rightarrow \ell\nu)+\gamma$  processes in the combined signal region.

Using  $R_{\ell\gamma}^{W\gamma}$  and  $f_{W\gamma}^{Z\gamma}$ , the total estimated event yield  $T_{\ell\gamma}$  in each single-lepton control region in the  $i^{\text{th}}$  bin of the  $E_T^\gamma$  distribution is given by

$$T_{\ell\gamma,i} = \frac{N_i^{Z\gamma}}{R_{\ell\gamma,i}^{W\gamma} f_{W\gamma,i}^{Z\gamma}} + b_{\ell\gamma,i}, \quad (6.8)$$

where  $b_{\ell\gamma}$  is the predicted contribution from other background sources in the single-lepton regions, namely misidentified electrons and hadrons and other minor SM processes.

## 6.7 Beam halo

Bremsstrahlung photons emitted by beam halo muons in the ECAL volume generate a physical EM shower in the ECAL crystals [87]. Large deposits energy are rare,

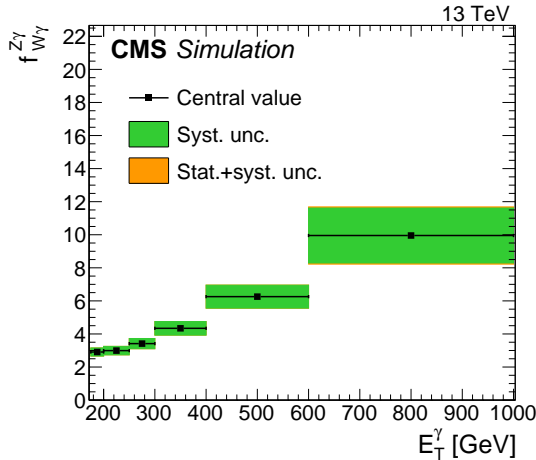


Figure 6-23: Transfer factor  $f_{W\gamma}^{Z\gamma}$  in the combined signal regions. The numerator is the expected  $Z(\rightarrow \nu\bar{\nu})+\gamma$  yield and the denominator is the expected  $W(\rightarrow \ell\nu)+\gamma$  yield. The uncertainty bands in green (inner) and orange (outer) show the systematic uncertainty, and the combination of systematic and statistical uncertainty arising from limited MC sample size, respectively. The systematic uncertainties considered are the uncertainties from higher-order theoretical corrections.

but the rate of beam halo penetration during the 2016 run was substantial. The characteristic features of a shower caused by a halo particle include coincident hits in the barrel muon system and a “trail” of low-energy clusters in ECAL along the particle trajectory. The beam halo MET filter described in Section 5.2.6 exploits the former, while the  $E_{\text{MIP}}$  variable described in Section 5.2.3 captures the latter.

Because beam halo particles are produced through complex LHC machine effects, the observed distribution of the halo showers is not symmetric in the azimuthal angle in the detector coordinates. The right side of Figure 6-24 is a  $\phi^\gamma$  distribution of the halo showers obtained from the SinglePhoton dataset, requiring  $E_{\text{T}}^{\text{miss}} > 140$  GeV. Halo showers are defined as those that fail the MIP-tagging and in the event tagged by the CSC beam halo tagger. On the other hand, reconstructed showers from all other sources are symmetric in  $\phi^\gamma$  as shown on the left side of Figure 6-24.

For the distribution of Fig. 6-24 to be a valid template for halo showers, it must be first confirmed that its shape is invariant under photon selection requirements. However, further study of the  $\phi^\gamma$  distribution of the halo showers indicates that the relative strength of the two prominent peaks in the distribution may change under

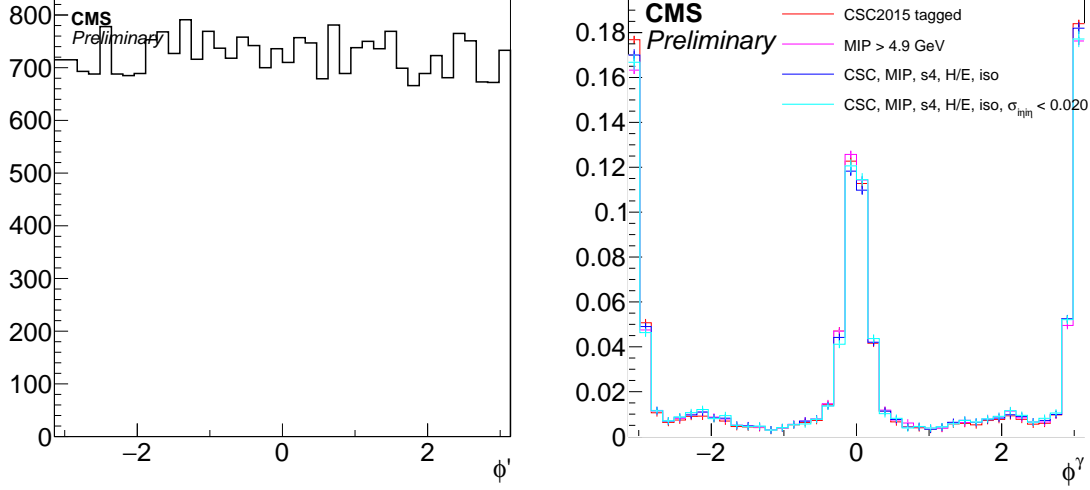


Figure 6-24: Left: The  $\phi^\gamma$  distribution from  $Z(\rightarrow \nu\bar{\nu})+\gamma$  MC simulation. Right: The  $\phi^\gamma$  distribution of the halo-like showers, tagged in multiple ways. Histograms are normalized to unity. The cyan histogram is the  $\phi^\gamma$  distribution after applying photon identification selections except for the shower shape. It can be seen that the  $\phi^\gamma$  distribution is highly stable against the listed identification selections.

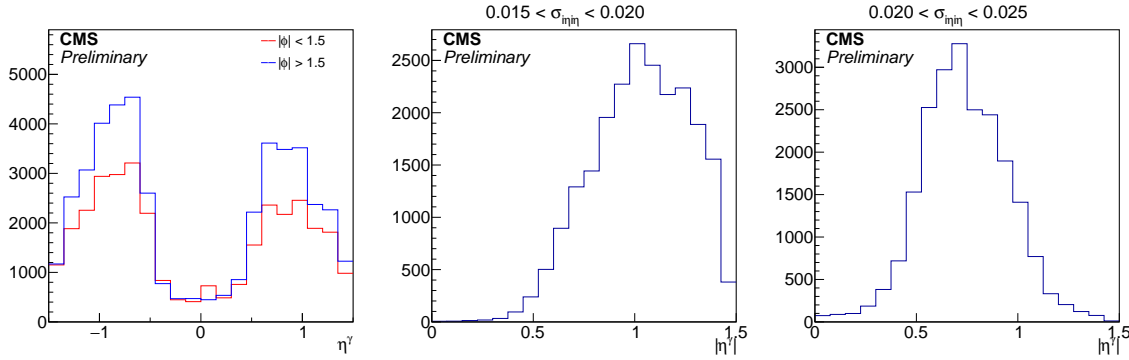


Figure 6-25: Left:  $\eta$  distribution of the halo-like showers with  $|\phi| < \pi/2$  and  $|\phi| > \pi/2$ . Middle and right: shift in the  $\eta$  distribution of the halo-like showers with respect to the requirement on  $\sigma_{inj\eta}$ .

the  $\sigma_{i\eta i\eta}$  selection requirement. To explain this phenomenon, one needs to look at the the  $\eta^\gamma$  distribution of the shower populations near  $\phi^\gamma \sim 0$  and  $\phi^\gamma \sim \pi$ , shown in the top portion of Figure 6-25. Meanwhile, halo showers tend to have narrower shape in the  $\eta$  direction when occurring at high  $\eta$ , due to the projective geometry of the ECAL crystals, visible in the bottom portion of Figure 6-25 bottom). Combining the two observations, the conclusion is that the stringent requirement on the narrowness of the shower in the photon selection will preferentially reduce the  $\phi \sim 0$  population.

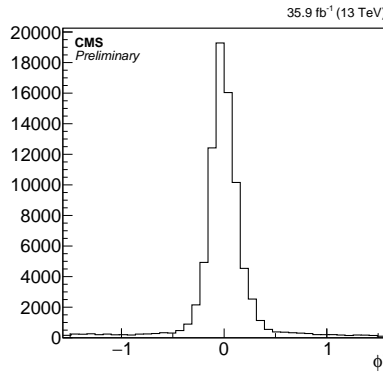


Figure 6-26: Folded  $\phi'$  distribution of the halo sample.

Nevertheless, the invariance under photon selection is recovered by folding the  $\phi^\gamma$  distribution such that the two peaks of the halo showers coincide. To match the positions of the peaks in the halo template, the distribution is shifted by 0.005 and then folded along 0. The new angular variable  $\phi'$

$$\phi' := \left| \left[ [\phi^\gamma + 0.005]_{-\pi}^\pi - \frac{\pi}{2} \right]_{-\pi}^\pi \right| - \frac{\pi}{2}, \quad (6.9)$$

where  $[\cdot]_\pi^\pi$  signifies casting the content into range  $[-\pi, \pi]$ , exhibits a unimodal distribution for the halo template, as shown in Fig. 6-26.

The contribution of real photons into the halo control sample is negligible. This is confirmed from the  $\sigma_{i\eta i\eta}$  distribution of the halo control sample and the correlation between  $\sigma_{i\eta i\eta}$  and  $E_{\text{MIP}}$  in a MC true-photon sample. The  $\sigma_{i\eta i\eta}$  distribution of the halo control sample features a small peak at  $\sigma_{i\eta i\eta} \sim 0.01$ , which can be attributed to contributions from true photons, as the photon  $\sigma_{i\eta i\eta}$  distribution overlaid in Fig-

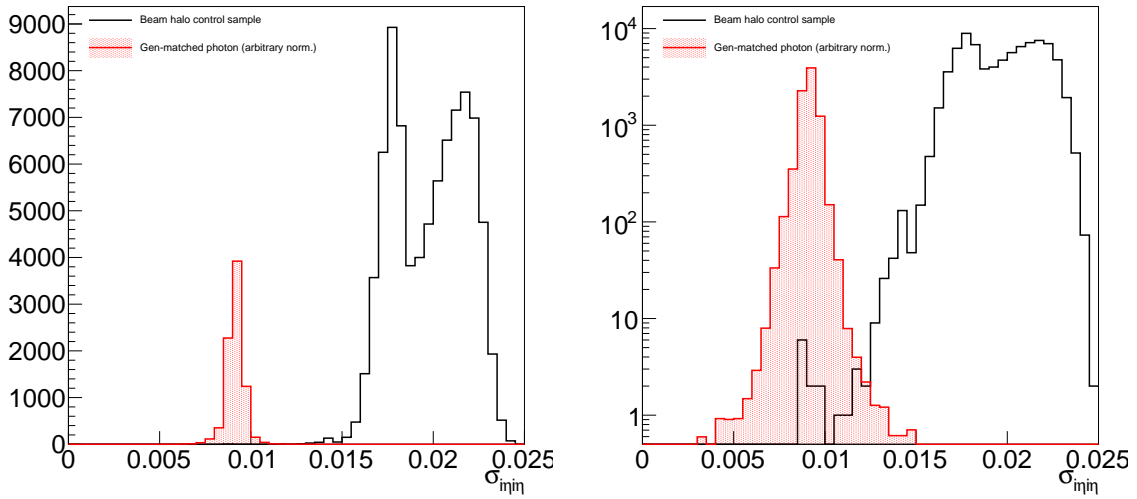


Figure 6-27: The  $\sigma_{i\eta i\eta}$  distribution of the beam halo control sample and a reference distribution from truth-matched MC photons. Left: linear scale, Right: log scale. There is a small peak at  $\sigma_{i\eta i\eta} \sim 0.01$  in the beam halo control sample, which is not visible in linear-scale.

ure 6-27 suggests. However, the contribution of true photons diminishes rapidly with increasing  $\sigma_{i\eta i\eta}$ . Additionally, Figure 6-28 illustrates that the shape of the true-photon  $\sigma_{i\eta i\eta}$  does not change significantly with respect to  $E_{\text{MIP}}$ . From these two observations, we can see that there are only a negligible number of true photons in the halo control sample.

While the peaking behavior is a robust feature of the halo showers, their rate is not easily predictable. Therefore, a two-template fit to the  $\phi'$  distribution of the photons in the candidate sample, where the templates are a uniform distribution (Figure 6-24 left) and that of the halo shower (Figure 6-26), accurately estimates the amount of beam halo background present in the signal region. For this analysis, the splitting of the signal region functions in a similar manner, enabling us to determine the beam halo contribution during the signal extraction procedure.

In the horizontal ( $H$ ) and vertical ( $V$ ) signal regions, collision processes occupy the relative fractions of phase space  $C_H = 1/\pi$  and  $C_V = (\pi - 1)/\pi$  corresponding to  $|\phi'| < 0.5$  and  $0.5 < |\phi'| < \pi/2$ , respectively. The corresponding fractions for beam halo events are determined by selecting a halo-enriched sample where the halo veto

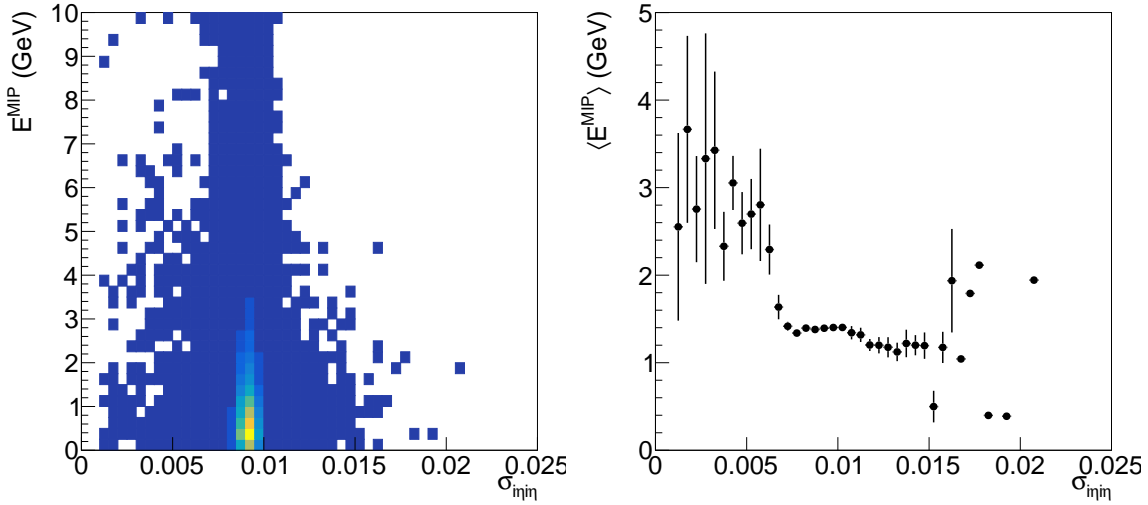


Figure 6-28: Correlation between  $\sigma_{i\eta i\eta}$  and  $E_{\text{MIP}}$  in truth-matched MC photons. Left:  $E_{\text{MIP}}-\sigma_{i\eta i\eta}$  distribution. Right: average  $E_{\text{MIP}}$  in bins of  $\sigma_{i\eta i\eta}$ .

is inverted. Thus, a fit of the two signal regions provides an estimate of the overall normalization of the beam halo background, denoted  $h$ .

The  $E_{\text{T}}^{\gamma}$  dependence of the halo background is encoded in  $n_{K,i}^{\text{halo}}$ , the unit-normalized beam halo prediction in the  $i^{\text{th}}$  bin of the signal region  $K \in \{H, V\}$ . Using the notation introduced in Section 6.6, the total estimated background  $T_K$  in the two signal regions are

$$\begin{aligned} T_{K,i} &= C_K \left[ N_i^{Z\gamma} + N_i^{W\gamma} + b_{K,i} \right] + h n_{K,i}^{\text{halo}} \\ &= C_K \left( \left[ 1 + \left( f_{W\gamma i}^{Z\gamma} \right)^{-1} \right] N_i^{Z\gamma} + b_{K,i} \right) + h n_{K,i}^{\text{halo}}, \end{aligned} \quad (6.10)$$

where  $b_{K,i}$  is the total contribution to bin  $i$  of region  $K$  from electron and hadron misidentification, ECAL spikes, and other minor SM background processes.

## 6.8 ECAL spikes

Noise in the photodetector or the detector electronics can result in spurious photon signals. Most of the time, such spurious signal is filtered out by multiple layers of protection, starting from the so-called ‘‘spike killer’’ algorithm at the Level 1 trig-

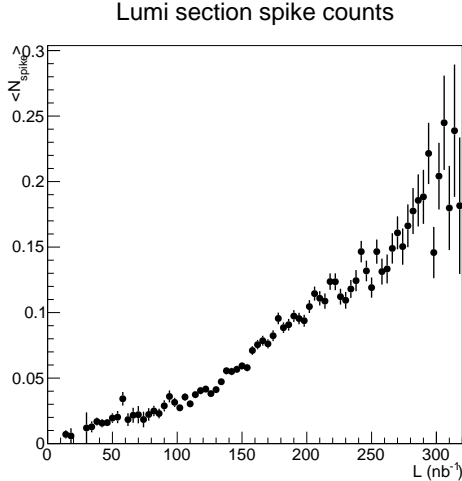


Figure 6-29: Average number of spike clusters in a luminosity section, identified by  $\sigma_{inj} < 0.001$  and  $E > 50$  GeV, in muon-triggered events, versus integrated luminosity of the luminosity section.

ger [88]. Nevertheless, in rare cases, noise in a single ECAL channel coincides with pileup or other energy deposit in the nearby crystals and appear as a high-energy photon cluster.

The origin of ECAL spikes is believed to be interactions of neutrons and other hadronic particles (collectively called neutral hadrons hereafter) with the photocathode material of the ECAL avalanche photo diodes (APD) [89]. Nuclear fission at the APD surface then causes a large electron avalanche, which is mistaken as a large photon yield scintillation in the ECAL crystal. Evidences supporting this hypothesis is documented in Reference [88]. In Figure 6-29, scaling of the rate of spikes with the instantaneous luminosity is confirmed, up to much higher luminosity values than was observed at the time when Reference [88] was written.

A known feature of such spurious photon clusters is that the recorded pulse shape of the seed crystal, i.e., the channel with the noise, is not what is expected from a real electromagnetic shower in ECAL. In particular, this translates to a distinctive early rec hit time distribution, since the rec hit time is extracted from a fit to the pulse shape assuming a normal pulse.

In the normal CMS data reconstruction, rec hits that are tagged as spike-like are ignored in clustering. Rec hits are tagged as spikes if there is very little energy deposit

recorded in the surrounding crystals, or if the reconstructed time is out of an allowed window. Identical algorithms are employed in the HLT and offline reconstructions.

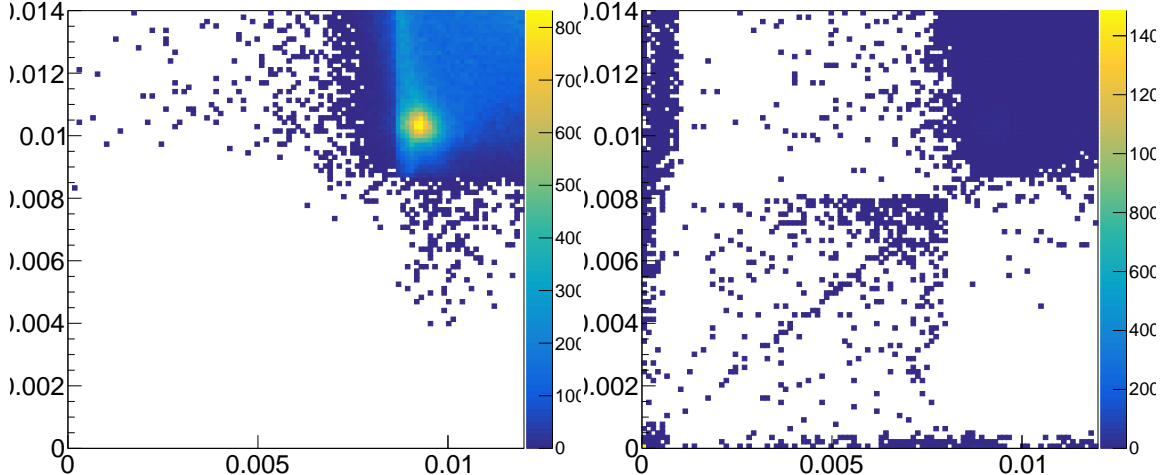


Figure 6-30: Two-dimensional distributions in  $\sigma_{i\phi i\phi}$  and  $\sigma_{i\eta i\eta}$  of ECAL clusters in the standard reconstruction (left) and the special reconstruction with no spike cleaning (right).

To study an unbiased spike sample, ECAL DIGI samples stored in the SingleMuon AOD datasets are reconstructed into ECAL clusters with no spike cleaning applied. DIGIs associated with the standard and “uncleaned” photon objects are stored in AOD, and ones for the uncleaned photons is rich in spike-like hits. Figure 6-30 shows how narrow clusters are cleaned away in the normal reconstruction.

Figure 6-31 shows the spacial and temporal distributions of the rec hits seeding narrow ( $\sigma_{i\eta i\eta} < 0.001$ ) clusters. The spacial distribution appears mostly random, indicating that there is no single source of spike-like rec hits. The two highest peaks in the time distribution at  $t \sim -15$  ns and  $t \sim 10$  ns are characteristic of pulse shapes, which rise faster than the pulse from the normal scintillation. The second peak is understood to come from the next bunch crossing.

The small peak at  $t \sim 0$  in the time distribution of Fig. 6-31 is due to actual “physical” clusters that happened to have a very narrow cluster shape. By processing the  $\gamma + \text{jets}$  MC simulation events through this special reconstruction, we see that about 0.5% of ECAL clusters from prompt photons have  $\sigma_{i\eta i\eta} < 0.001$  as shown in

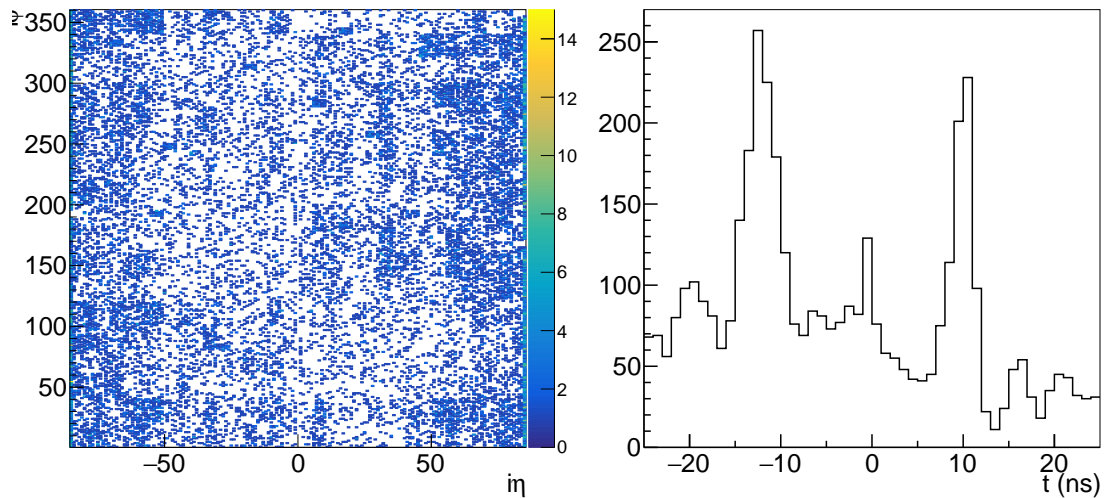


Figure 6-31:  $\eta-\phi$  and time distributions of seed hits of narrow ( $\sigma_{i\eta i\eta} < 0.001$ ) clusters.

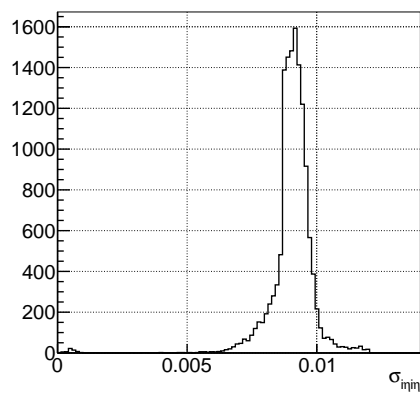


Figure 6-32:  $\sigma_{i\eta i\eta}$  distribution of uncanceled clusters from  $\gamma+\text{jets}$  MC simulation.

Figure 6-32.

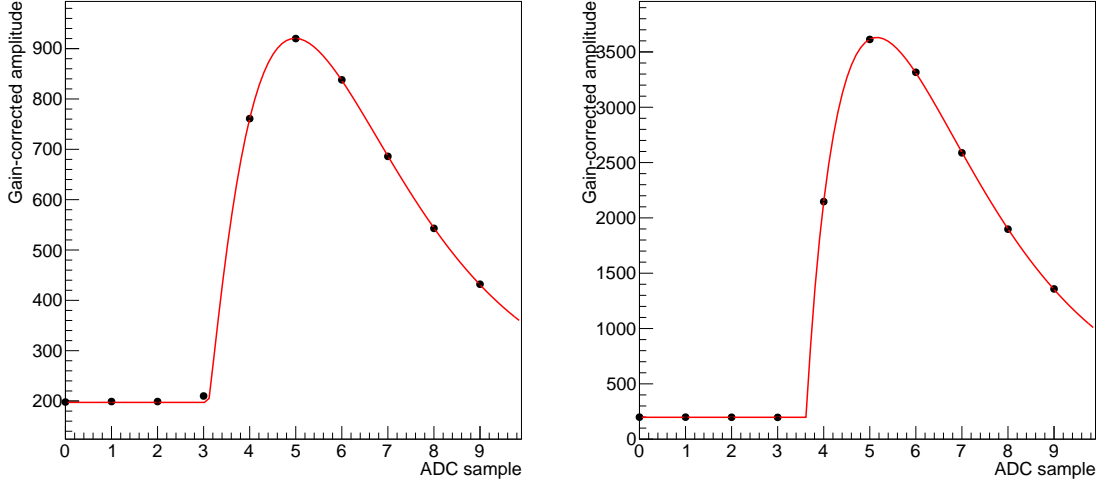


Figure 6-33: Example ECAL DIGIs and corresponding pulse shapes reconstructed through  $\chi^2$  fits of Equation 6.11, for normal (left) and spike-like (right) hits.

To understand the time distribution, one can investigate the original DIGI samples from which rec hits are made. At each event readout, a single ECAL channel outputs 10 ADC signals corresponding to a sampling of the analog pulse output of multi-gain preamplifier (MGPA) in range  $t_0 - 125 \text{ ns} < t < t_0 + 100 \text{ ns}$ , where  $t_0$  is the time of the triggering bunch crossing. These 10 signal points can be described well by the formula

$$f(t) = A \left(1 - \frac{t - \tau}{\alpha\beta}\right)^\alpha \exp\left(-\frac{t - \tau}{\beta}\right). \quad (6.11)$$

In the formula, parameters  $A$  and  $\tau$  correspond to the pulse amplitude and peak time, whereas  $\alpha$  and  $\beta$  control the shape of the pulse. Figure 6-33 illustrates various observed pulse shapes fit with the above formula with all parameters floating. A  $\chi^2$  fit is employed using the average noise amplitude of each MGPA channel as the errors on the data points. The noise is measured in ECAL calibration cycles in the inter-fill period and is recorded in the conditions database.

In the  $\alpha-\beta$  parameter space, seed rec hits of wide clusters concentrate around  $(\alpha, \beta) \sim (1.1, 1.7)$ , while spike-like hits populate the region  $\alpha < 0.9$  as shown in

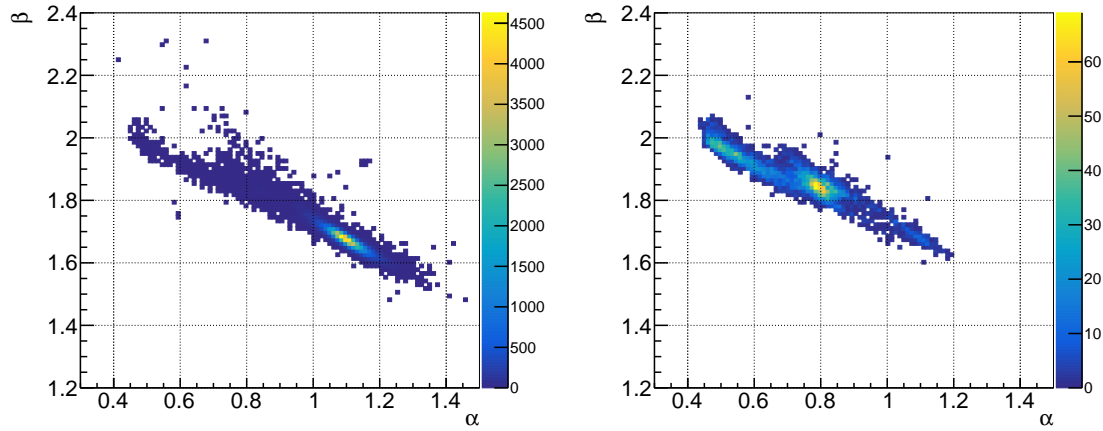


Figure 6-34:  $\alpha$ - $\beta$  distributions of the seed hits of physical wide clusters (left) and spike-like clusters (right).

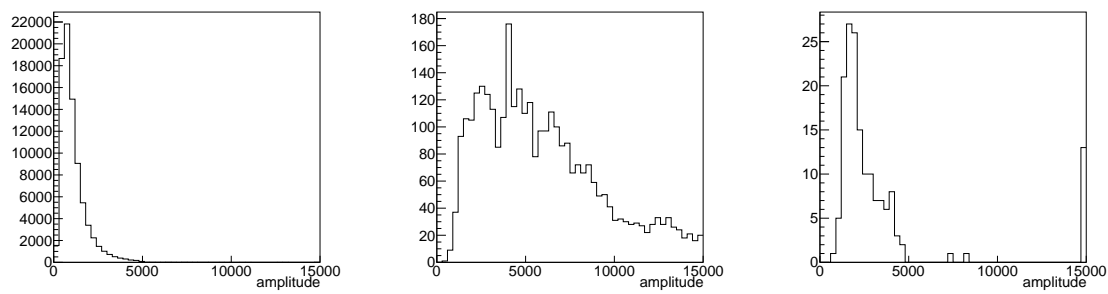


Figure 6-35: Seed crystal pulse amplitude distributions of physical wide clusters (left), narrow clusters with  $\alpha < 0.9$  (center), and narrow clusters with  $\alpha > 0.9$  (right).

Figure 6-34. In fact, the pulse amplitude distribution of narrow-cluster seeds with  $\alpha > 0.9$  is unlike that of the narrow-cluster seeds with  $\alpha < 0.9$ , and resembles the amplitude distribution of wide-cluster seeds shown in Figure 6-35. This suggests that the population  $\alpha > 0.9$  correspond to the clusters of physical, prompt photons. It then follows that spike hits can be regarded to exclusively have sharp pulse shapes.

Given these observations, the time distribution of spike-like rec hits outside of the window  $-15 \text{ ns} < t < -10 \text{ ns}$  (and the equivalent with one-bunch-crossing shift) is understood to be due to delayed interactions of neutral hadrons with the APDs, as documented also in Reference [88]. In other words, ECAL spike clusters which survive the time cleaning cut of the standard reconstruction are a part of a broad tail of a distribution, and there is no evidence of spike signals that specifically populate the “in-time” region  $-3 \text{ ns} < t < 3 \text{ ns}$ .

Having established that there is no special population of ECAL spikes in the in-time region, we can estimate the number  $D$  of ECAL spike events present in the signal candidate sample to be

$$D = C \times \frac{B}{A}, \quad (6.12)$$

where

- A = Number of clusters with  $\sigma_{i\eta i\eta}$  or  $\sigma_{i\phi i\phi}$  less than 0.001 and seed time  $-15 \text{ ns} < t < -10 \text{ ns}$ , counted in the special-reconstruction sample,
- B = Number of clusters with both  $\sigma_{i\eta i\eta}$  and  $\sigma_{i\phi i\phi}$  greater than 0.001 and seed time  $-15 \text{ ns} < t < -10 \text{ ns}$ , counted in the special-reconstruction sample,
- C = Number of clusters with  $\sigma_{i\eta i\eta}$  or  $\sigma_{i\phi i\phi}$  less than 0.001 but an in-time seed, counted in the standard-reconstruction sample passing all other signal event selection.

The special-reconstruction samples for A and B are from the SinglePhoton datasets, with only the timing cleaning removed from the offline reconstruction. In this way, the selection bias over spikes from the L1T, HLT, and offline reconstruction is equally

applied to samples A, B, and C. Plugging in the observed numbers, we have

$$A = 4969$$

$$B = 1180$$

$$C = 54$$

$$\therefore D = 12.8 \pm 1.8(\text{stat.})$$

There are, however, at least two reasons to believe that this method overestimates the number of spike events in the signal region. One is that the population C contains some physical, prompt photon clusters that just happen to be narrow, as observed in Fig. 6-32. Another reason is that there is likely a correlation between the cluster width and the seed time such that the ratio of true D to C is smaller than  $B/A$ . This statement is based on the standard hypothesis that the wide-cluster spike is an ECAL spike embedded in a physical EM shower cluster. Under this model, spikes in wide clusters are mainly caused by prompt neutral hadrons in a jet, which implies that they strongly prefer seed time  $-15 \text{ ns} < t < -10 \text{ ns}$ . Given that this is a minor background with a relatively large uncertainty, as described below, we will still use this estimate as the nominal value of predicted spike contribution in the signal region.

The uncertainty in the estimate of D is evaluated by two modifications to A, B, and C. First, the three values are recomputed with using  $\sigma_{inj\eta} < 0.001$  as the only definition of narrow cluster. This results in a minor change of the value of D of  $12.1 \pm 1.7$ . Next, A and B are computed using a lower- $p_T$  SinglePhoton sample, requiring triggers `Photon135_PFMET100` or `Photon120_R9Id90_HE10_IsoM` to have fired, instead of the signal trigger. The second modification gives  $D = 9.1 \pm 1.3$ . We then take twice the discrepancy between the nominal D and the D value from the second modification to obtain a 33% systematic uncertainty on the spike background estimate.

## 6.9 Minor SM Backgrounds

After the full selection described in Section 6.2, the SM  $\gamma$ +jets,  $t\bar{t}\gamma$ ,  $VV\gamma$ ,  $Z(\rightarrow \ell\bar{\ell})+\gamma$ , and  $W \rightarrow \ell\nu$  processes are minor ( $\sim 10\%$ ) background processes in the signal region. These processes, collectively denoted as minor SM backgrounds, contribute in the signal region when the jet energy is severely mismeasured or the leptons fail to be reconstructed resulting in large  $E_T^{\text{miss}}$  in the signal region. However, the  $E_T^{\text{miss}}$  is typically aligned with the photon or one of the jets in such cases, and therefore various selections on the kinematic relations between the  $E_T^{\text{miss}}$ , photons, and jets are used to reduce these backgrounds to a manageable rate. The estimates for all five processes are taken from MADGRAPH5\_amc@NLO simulations at LO in QCD and are listed in Tables 6.8 and 6.9.

## 6.10 Statistical Interpretation

The potential signal contribution is extracted from the data via simultaneous fits to the  $E_T^\gamma$  distributions in the signal and control regions defined in Section 6.2. Uncertainties in various quantities are represented by nuisance parameters in the fit. Predictions for  $Z(\rightarrow \nu\bar{\nu})+\gamma$ ,  $W(\rightarrow \ell\nu)+\gamma$ , and the beam halo backgrounds are varied in the fit. Beam halo is not a major background, but the extraction of its rate requires a fit to the observed distributions in the signal region.

Free parameters of the fit are the yield of  $Z(\rightarrow \nu\bar{\nu})+\gamma$  background in each bin of the signal regions ( $N_i^{Z\gamma}$ ) and the overall normalization of the beam halo background ( $h$ ). Bin-by-bin yields of  $W(\rightarrow \ell\nu)+\gamma$  and  $Z(\rightarrow \ell\bar{\ell})+\gamma$  samples in all regions are related to the yield of  $Z(\rightarrow \nu\bar{\nu})+\gamma$  through the MC prediction through the transfer factors defined in Section 6.6. The transfer factors are allowed to shift within the aforementioned theoretical and experimental uncertainties. The background-only

likelihood that is maximized in the fit is

$$\begin{aligned}
\mathcal{L} &= \prod_i \left\{ \mathcal{L}_{\text{signal}} \times \mathcal{L}_{\text{single-lepton}} \times \mathcal{L}_{\text{dilepton}} \right\} \times \mathcal{L}_{\text{nuisances}} \\
&= \prod_i \left\{ \prod_{K=H,V} \mathcal{P}(d_{K,i} | T_{K,i}(\vec{\theta})) \times \prod_{\ell=e,\mu} \mathcal{P}(d_{\ell\gamma,i} | T_{\ell\gamma,i}(\vec{\theta})) \times \prod_{\ell=e,\mu} \mathcal{P}(d_{\ell\ell\gamma,i} | T_{\ell\ell\gamma,i}(\vec{\theta})) \right\} \times \prod_j \mathcal{N}(\theta_j) \\
&= \prod_i \left\{ \prod_{K=H,V} \mathcal{P}\left(d_{K,i} \middle| C_K \left( \left[ 1 + (f_{W\gamma,i}^{Z\gamma}(\vec{\theta}))^{-1} \right] N_i^{Z\gamma} + b_{K,i}(\vec{\theta}) \right) + h n_{K,i}^{\text{halo}}(\vec{\theta}) \right) \right. \\
&\quad \times \prod_{\ell=e,\mu} \mathcal{P}\left(d_{\ell\gamma,i} \middle| \frac{N_i^{Z\gamma}}{R_{\ell\gamma,i}^{W\gamma}(\vec{\theta}) f_{W\gamma,i}^{Z\gamma}(\vec{\theta})} + b_{\ell\gamma,i}(\vec{\theta}) \right) \\
&\quad \left. \times \prod_{\ell=e,\mu} \mathcal{P}\left(d_{\ell\ell\gamma,i} \middle| \frac{N_i^{Z\gamma}}{R_{\ell\ell\gamma,i}^{Z\gamma}(\vec{\theta})} + b_{\ell\ell\gamma,i}(\vec{\theta}) \right) \right\} \times \prod_j \mathcal{N}(\theta_j),
\end{aligned} \tag{6.13}$$

following the notation introduced in Section 6.6, and where  $\mathcal{P}(n|\lambda)$  is the Poisson probability of  $n$  for mean  $\lambda$ ,  $\mathcal{N}$  denotes the unit normal distribution, and  $d_{K,i}$  is the observed number of events in bin  $i$  of region  $K$ . Systematic uncertainties on  $R_e$ ,  $R_h$ ,  $k_{\text{QCD}}^{\text{NNLO}}$ ,  $k_{\text{EW}}^{\text{Sudakov}}$ ,  $k_{\text{EW}}^{q\gamma}$ , and the various scale factors  $\rho$  are treated as nuisance parameters in the fit and are represented by  $\vec{\theta}$ . Quantities such as  $R_{\ell\ell\gamma}^{Z\gamma}$ ,  $R_{\ell\gamma}^{W\gamma}$ ,  $f_{W\gamma}^{Z\gamma}$ ,  $n_K^{\text{halo}}$ , and  $b_K$  appear in the likelihood function as  $Q(\vec{\theta}) = \overline{Q} \sum_j \exp(\sigma_j \theta_j)$ , where  $\overline{Q}$  is the nominal value of the quantity and  $\sigma_j$  is standard deviation of each systematic uncertainty  $\theta_j$  on the quantity.

## 6.11 Results

Using the likelihood from the previous section, we perform a maximum likelihood fit to the observed  $E_T^\gamma$  distributions in all the control samples and signal region simultaneously. The minimization of the negative log likelihood is performed using the Minuit2 algorithm through an interface provided in the RooStats package [90].

The comparison between the observed distributions and the results from simulations before and after performing the simultaneous fit are shown in Figures 6-36 and 6-37 for the signal and control regions, respectively. The observed distributions are in agreement with the prediction from SM and non-collision backgrounds and no significant excess of events beyond the SM expectation is observed.

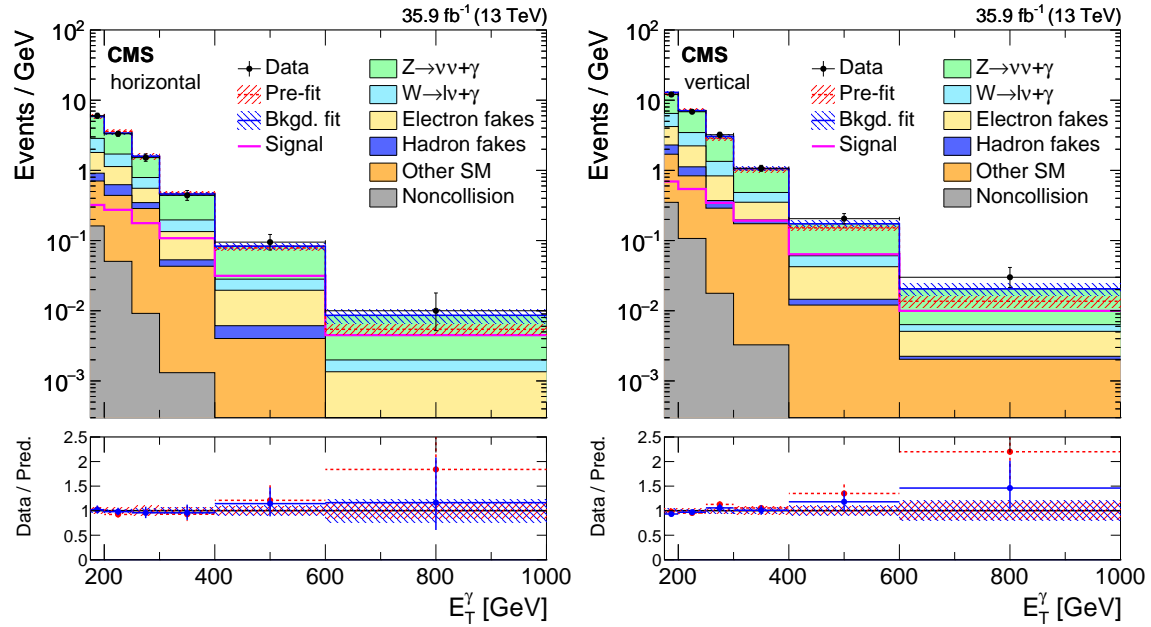


Figure 6-36: Observed  $E_T^\gamma$  distributions in the horizontal (left) and vertical (right) signal regions compared with the post-fit background expectations for various SM processes. The last bin of the distribution includes all events with  $E_T^\gamma > 1000$  GeV. The expected background distributions are evaluated after performing a combined fit to the data in all the control samples and the signal region. The ratios of data with the pre-fit background prediction (red dashed) and post-fit background prediction (blue solid) are shown in the lower panels. The bands in the lower panels show the post-fit uncertainty after combining all the systematic uncertainties. The expected signal distribution from a 1 TeV vector mediator decaying to 1 GeV DM particles is overlaid.

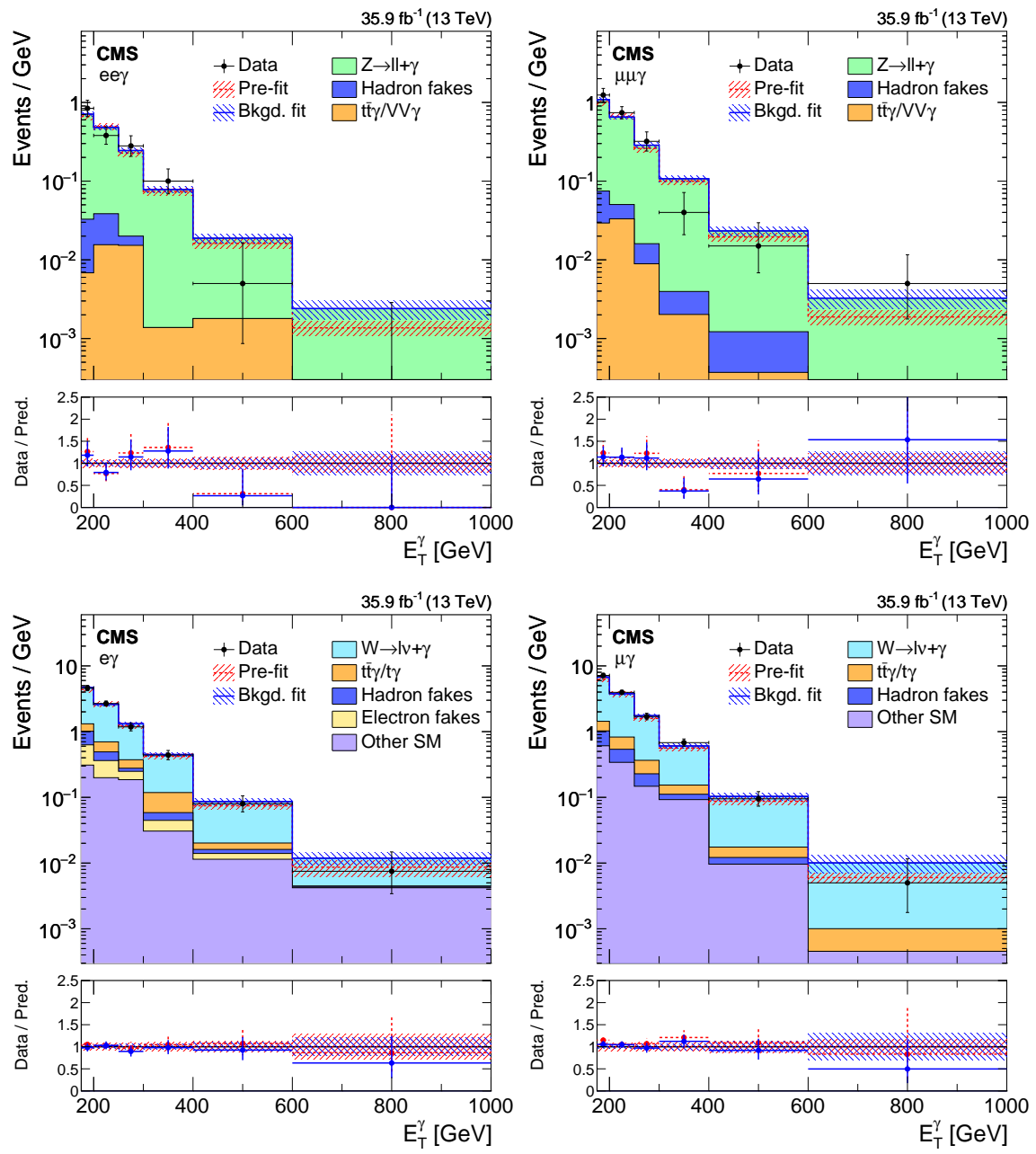


Figure 6-37: Comparison between data and MC simulation in the four control regions:  $ee\gamma$  (upper left),  $\mu\mu\gamma$  (upper right),  $e\gamma$  (lower left),  $\mu\gamma$  (lower right) before and after performing the simultaneous fit across all the control samples and signal region, and assuming absence of any signal. The last bin of the distribution includes all events with  $E_T^\gamma > 1000$  GeV. The ratios of data with the pre-fit background prediction (red dashed) and post-fit background prediction (blue solid) are shown in the lower panels. The bands in the lower panels show the post-fit uncertainty after combining all the systematic uncertainties.

### 6.11.1 Limits

Upper limits are determined for the production cross section of the new-physics processes mentioned in Section 2.4. For each model, a 95% confidence level (CL) upper limit is obtained utilizing the asymptotic  $CL_s$  criterion [91–93], using a test statistic based on the negative logarithm of the likelihood in Section 6.10.

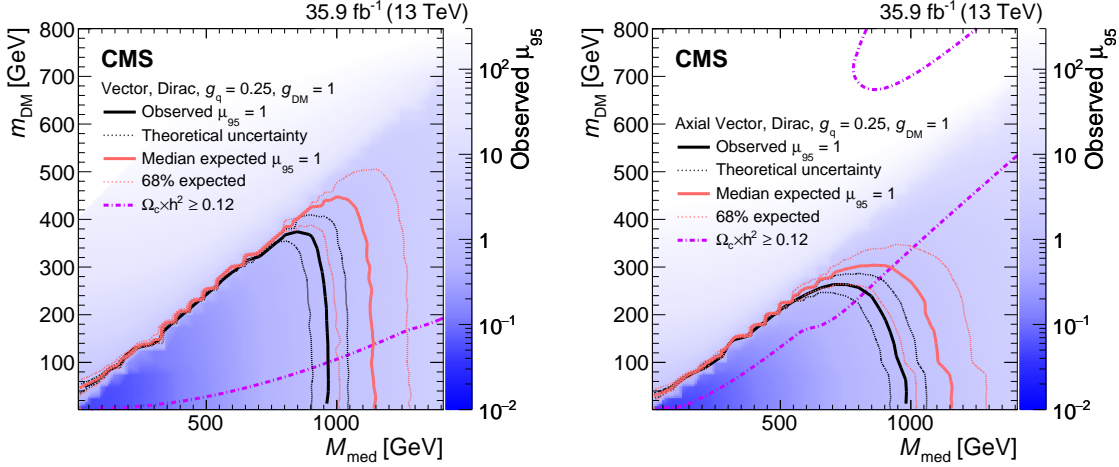


Figure 6-38: The ratio of 95% CL upper cross section limits to the theoretical cross section ( $\mu_{95}$ ), for DM simplified models with vector (left) and axial-vector (right) mediators, assuming  $g_q = 0.25$  and  $g_{DM} = 1$ . The expected  $\mu_{95} = 1$  contours are overlaid in red. The region under the observed contour is excluded. For DM simplified model parameters in the region below the lower violet dot-dash contour, and also above the corresponding upper contour in the right hand plot, cosmological DM abundance exceeds the density observed by the Planck satellite experiment.

Figure 6-38 shows the 95% CL upper cross section limits with respect to the corresponding theoretical cross section ( $\mu_{95} = \sigma_{95\%}/\sigma_{\text{theory}}$ ) for the vector and axial-vector mediator scenarios, in the  $M_{\text{med}} - m_{\text{DM}}$  plane. The solid black (dashed red) curves are the observed (expected) contours of  $\mu_{95} = 1$ . The  $\sigma_{\text{theory}}$  hypothesis is excluded at 95% CL or above in the region with  $\mu_{95} < 1$ . The uncertainty in the expected upper limit includes the experimental uncertainties. For the simplified DM LO models considered, mediator masses up to 950 GeV are excluded for values of  $m_{\text{DM}}$  less than 1 GeV.

The results for vector and axial-vector mediators are compared to constraints from the observed cosmological relic density of DM as determined from measurements of the

cosmic microwave background by the Planck satellite experiment [94]. The expected DM abundance is estimated, separately for each model, using the thermal freeze-out mechanism implemented in the MADDM [95] framework and compared to the observed cold DM density  $\Omega_c h^2 = 0.12$  [94], where  $\Omega_c$  is the DM relic abundance and  $h$  is the dimensionless Hubble constant.

### 6.11.2 Comparison to Results from Other Experiments

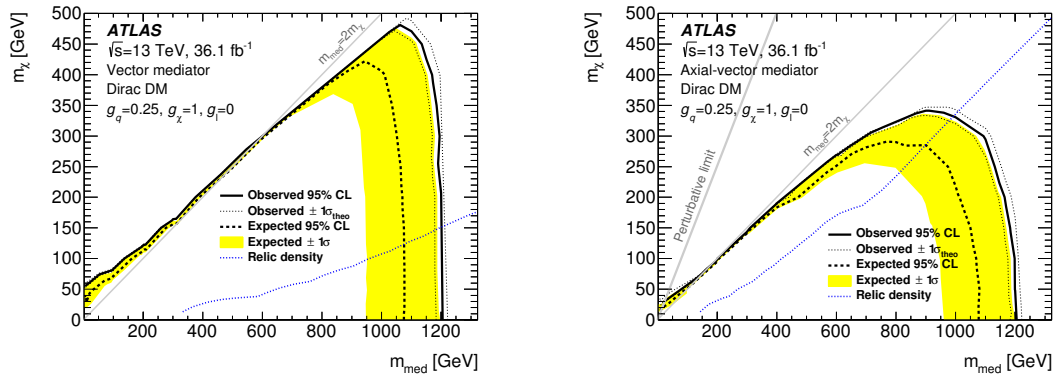


Figure 6-39: The equivalent of Figure 6-38 with results from ATLAS. The expected  $\mu_{95} = 1$  contours are overlaid in yellow. The region under the observed contour is excluded. Reprinted from Reference [96]

The results from an equivalent analysis by ATLAS [96] are shown in Figure 6-39. To enable a direct comparison with results from direct and indirect detection experiments, the 95% CL limits on the mediator mass for the vector and axial-vector models are translated to 90% CL limits on the spin-independent and spin-dependent DM–nucleon scattering cross sections,  $\sigma_{\text{SI}}$  and  $\sigma_{\text{SD}}$  respectively, following the prescriptions given in Reference [97] and [47]. The exclusion contours for the vector and axial-vector models shown in Figure 6-38 are translated into the  $\sigma_{\text{SI}} - m_{\text{DM}}$  and  $\sigma_{\text{SD}} - m_{\text{DM}}$  planes shown in Figure 6-40. When compared to recent results by the CDMSLite [52], LUX [51], PandaX-II [98], XENON1T [99], and CRESST-II [100] collaborations, the limits obtained from this search provide stronger constraints for DM masses less than 2 GeV for spin independent models. When compared to recent results by the PICO-60 [53], IceCube [58], PICASSO [101] and Super-Kamiokande [102] collaborations,

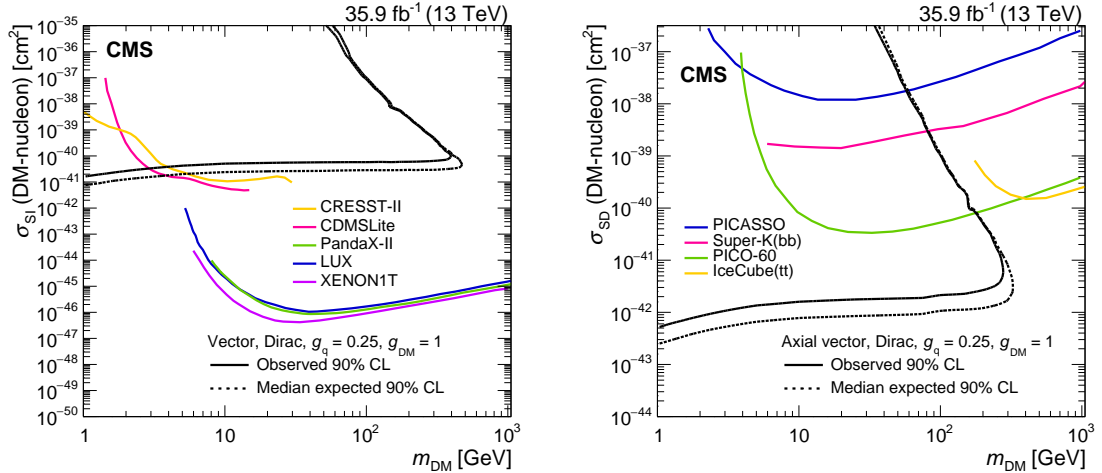


Figure 6-40: The 90% CL exclusion limits on the  $\chi$ -nucleon spin-independent scattering cross sections involving the vector operator (top) and the  $\chi$ -nucleon spin-dependent scattering cross sections involving the axial-vector operator (bottom) as a function of the  $m_{\text{DM}}$ . Simplified model DM parameters of  $g_q = 0.25$  and  $g_{\text{DM}} = 1$  are assumed. The region to the upper left of the contour is excluded. On the plots, the median expected 90% CL curve overlaps the observed 90% CL curve. Also shown are corresponding exclusion contours, where regions above the curves are excluded, from the recent results by the direct and indirect detection experiments listed in the text.

the limits obtained from this search provide stronger constraints for DM masses less than 200 GeV for spin dependent models.

### 6.11.3 Interpretation of Additional Models

In addition to the background-only fit to all of the signal and control regions, we performed a simultaneous maximum likelihood fit to the observed  $E_T^\gamma$  distributions in the control regions only. The results of this fit enable the interpretation of new physics models not studied in this thesis with the simplified likelihood approach detailed in Reference [103]. The predicted yields in each bin of  $E_T^\gamma$  for all backgrounds in the horizontal and vertical signal regions after performing the control region only fit are given in Tables 6.8 and 6.9, respectively. The covariances between the predicted background yields across all the  $E_T^\gamma$  bins in the two signal regions are shown in Fig. 6-41.

$E_T^\gamma$ [GeV]	[175, 200]	[200, 250]	[250, 300]	[300, 400]	[400, 600]	[600, 1000]
$Z\gamma$	$81.2 \pm 8.0$	$88.2 \pm 8.4$	$38.8 \pm 4.8$	$26.8 \pm 3.7$	$8.8 \pm 1.9$	$1.4 \pm 0.7$
$W\gamma$	$27.9 \pm 3.7$	$29.9 \pm 3.9$	$11.4 \pm 1.7$	$6.3 \pm 1.2$	$1.4 \pm 0.4$	$0.1 \pm 0.1$
Misid. electrons	$22.5 \pm 2.7$	$25.7 \pm 2.7$	$10.5 \pm 1.0$	$8.2 \pm 0.7$	$2.7 \pm 0.2$	$0.5 \pm 0.0$
Misid. hadrons	$5.2 \pm 2.2$	$9.3 \pm 1.8$	$3.1 \pm 0.7$	$1.0 \pm 0.3$	$0.4 \pm 0.1$	$0.0 \pm 0.0$
Other SM	$13.6 \pm 2.0$	$19.6 \pm 1.3$	$13.9 \pm 0.4$	$4.2 \pm 0.2$	$0.8 \pm 0.0$	$0.1 \pm 0.0$
ECAL spikes	$4.3 \pm 1.3$	$2.7 \pm 0.8$	$0.5 \pm 0.1$	$0.1 \pm 0.0$	$0.0 \pm 0.0$	$0.0 \pm 0.0$
Total prediction	$154.6 \pm 8.3$	$175.4 \pm 8.8$	$78.2 \pm 5.3$	$46.6 \pm 4.0$	$14.1 \pm 2.1$	$2.1 \pm 0.8$
Observed	$150 \pm 12$	$166 \pm 13$	$76.0 \pm 8.7$	$44.0 \pm 6.6$	$19.0 \pm 4.4$	$4.0 \pm 2.0$

Table 6.8: Expected event yields in each  $E_T^\gamma$  bin for the various background processes in **the horizontal signal region**. The background yields and the corresponding uncertainties are obtained after performing a combined fit to data in all the control samples, excluding data in the signal region. The observed event yields in the horizontal signal region are also reported.

$E_T^\gamma$ [GeV]	[175, 200]	[200, 250]	[250, 300]	[300, 400]	[400, 600]	[600, 1000]
$Z\gamma$	$172 \pm 17$	$190 \pm 18$	$83 \pm 10$	$58.6 \pm 7.9$	$18.0 \pm 3.9$	$3.1 \pm 1.6$
$W\gamma$	$59.9 \pm 7.8$	$63.6 \pm 7.8$	$24.6 \pm 3.5$	$13.4 \pm 2.4$	$3.0 \pm 0.8$	$0.3 \pm 0.2$
Misid. electrons	$48.4 \pm 5.6$	$56.2 \pm 5.1$	$23.4 \pm 1.8$	$15.7 \pm 1.4$	$5.6 \pm 0.4$	$1.2 \pm 0.1$
Misid. hadrons	$15.1 \pm 4.4$	$14.5 \pm 3.1$	$4.2 \pm 0.8$	$2.3 \pm 0.8$	$0.5 \pm 0.1$	$0.1 \pm 0.1$
Other SM	$33.8 \pm 4.1$	$36.6 \pm 2.7$	$13.6 \pm 0.5$	$17.1 \pm 0.6$	$2.4 \pm 0.1$	$0.8 \pm 0.0$
ECAL spikes	$9.3 \pm 2.8$	$5.7 \pm 1.7$	$0.9 \pm 0.3$	$0.3 \pm 0.1$	$0.0 \pm 0.0$	$0.0 \pm 0.0$
Total prediction	$339 \pm 18$	$366 \pm 19$	$150 \pm 11$	$107.5 \pm 8.7$	$29.6 \pm 4.3$	$5.4 \pm 1.7$
Observed	$301 \pm 17$	$342 \pm 19$	$161 \pm 13$	$107 \pm 10$	$41.0 \pm 6.4$	$12.0 \pm 3.5$

Table 6.9: Expected event yields in each  $E_T^\gamma$  bin for the various background processes in **the vertical signal region**. The background yields and the corresponding uncertainties are obtained after performing a combined fit to data in all the control samples, excluding data in the signal regions. The observed event yields in the vertical signal region are also reported.

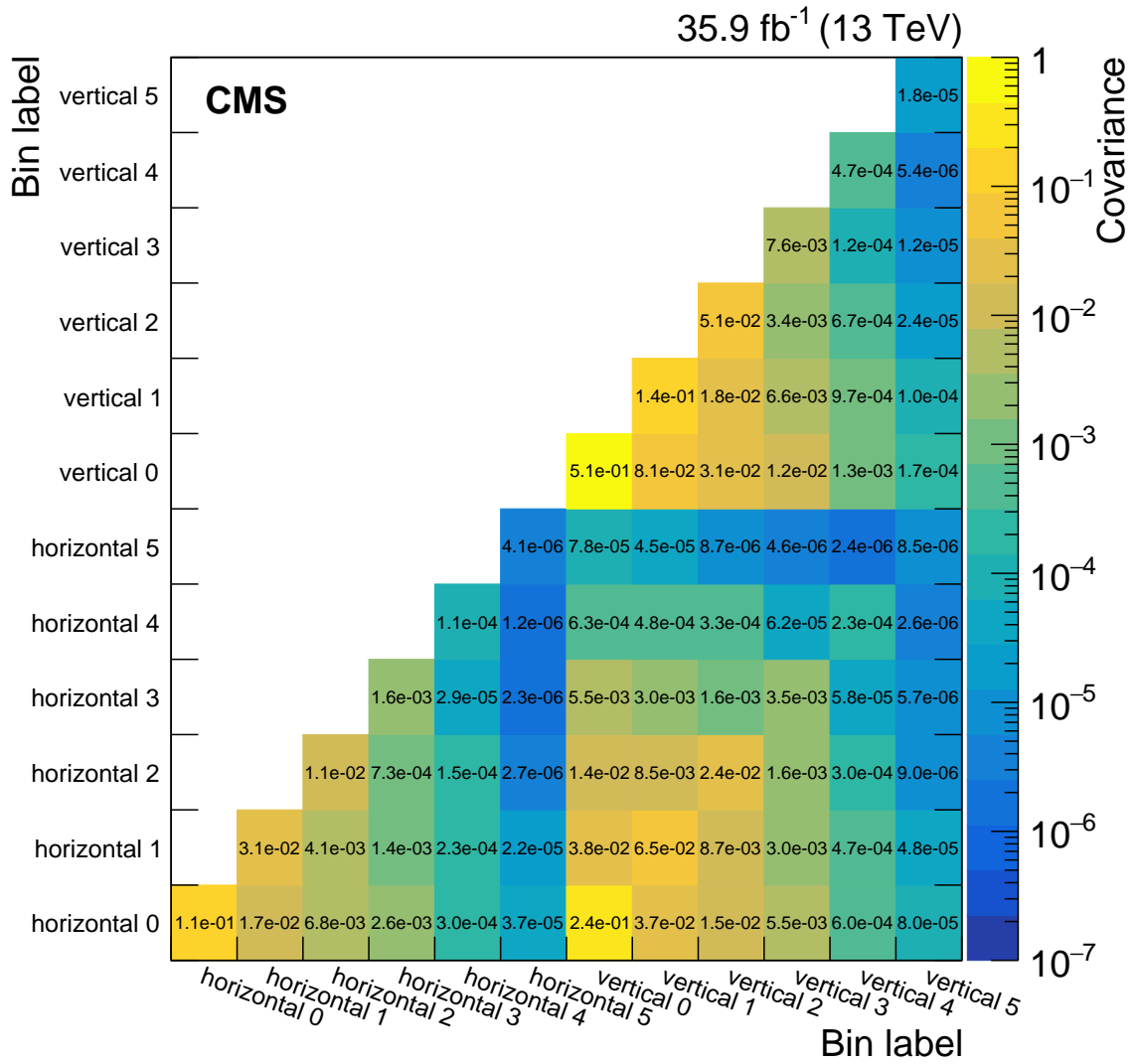


Figure 6-41: Covariances between the predicted background yields in all the  $E_T^\gamma$  bins of the horizontal and vertical signal regions. The bin labels specify which signal region the bin belongs to and what number bin it is for that region.

# Bibliography

- <sup>1</sup>M. Thomson, *Modern particle physics* (Cambridge University Press, 2013).
- <sup>2</sup>D. J. Gross and F. Wilczek, “Ultraviolet behavior of non-abelian gauge theories”, Phys. Rev. Lett. **30**, 1343–1346 (1973).
- <sup>3</sup>H. D. Politzer, “Reliable perturbative results for strong interactions?”, Phys. Rev. Lett. **30**, 1346–1349 (1973).
- <sup>4</sup>M. Tanabashi et al., “Review of particle physics”, Phys. Rev. D **98**, 030001 (2018).
- <sup>5</sup>R. D. Peccei and H. R. Quinn, “CP conservation in the presence of pseudoparticles”, Phys. Rev. Lett. **38**, 1440–1443 (1977).
- <sup>6</sup>R. D. Peccei, “The strong cp problem and axions”, in *Axions: theory, cosmology, and experimental searches* (Springer Berlin Heidelberg, Berlin, Heidelberg, 2008), pp. 3–17.
- <sup>7</sup>D. J. Gross and F. Wilczek, “Asymptotically free gauge theories. i”, Phys. Rev. D **8**, 3633–3652 (1973).
- <sup>8</sup>M. Gell-Mann, “A schematic model of baryons and mesons”, Physics Letters **8**, 214–215 (1964).
- <sup>9</sup>R. Aaij et al., “Observation of  $j/\psi p$  resonances consistent with pentaquark states in  $\Lambda b \rightarrow j/\psi K^- p$  decays”, Phys. Rev. Lett. **115**, 072001 (2015).
- <sup>10</sup>S. L. Glashow, “Partial-symmetries of weak interactions”, Nuclear Physics **22**, 579–588 (1961).
- <sup>11</sup>S. Weinberg, “A model of leptons”, Phys. Rev. Lett. **19**, 1264–1266 (1967).

- <sup>12</sup>A. Salam, “Weak and Electromagnetic Interactions”, Conf. Proc. **C680519**, 367–377 (1968).
- <sup>13</sup>J. Bardeen, L. N. Cooper, and J. R. Schrieffer, “Theory of superconductivity”, Phys. Rev. **108**, 1175–1204 (1957).
- <sup>14</sup>Y. Nambu, “Quasi-particles and gauge invariance in the theory of superconductivity”, Phys. Rev. **117**, 648–663 (1960).
- <sup>15</sup>P. W. Anderson, “Plasmons, gauge invariance, and mass”, Phys. Rev. **130**, 439–442 (1963).
- <sup>16</sup>J. Goldstone, “Field theories with «superconductor» solutions”, Il Nuovo Cimento (1955–1965) **19**, 154–164 (1961).
- <sup>17</sup>J. Goldstone, A. Salam, and S. Weinberg, “Broken symmetries”, Phys. Rev. **127**, 965–970 (1962).
- <sup>18</sup>F. Englert and R. Brout, “Broken symmetry and the mass of gauge vector mesons”, Phys. Rev. Lett. **13**, 321–323 (1964).
- <sup>19</sup>P. W. Higgs, “Broken symmetries, massless particles and gauge fields”, Physics Letters **12**, 132–133 (1964).
- <sup>20</sup>P. W. Higgs, “Broken symmetries and the masses of gauge bosons”, Phys. Rev. Lett. **13**, 508–509 (1964).
- <sup>21</sup>P. W. Higgs, “Spontaneous symmetry breakdown without massless bosons”, Phys. Rev. **145**, 1156–1163 (1966).
- <sup>22</sup>G. S. Guralnik, C. R. Hagen, and T. W. B. Kibble, “Global conservation laws and massless particles”, Phys. Rev. Lett. **13**, 585–587 (1964).
- <sup>23</sup>T. W. B. Kibble, “Symmetry breaking in non-abelian gauge theories”, Phys. Rev. **155**, 1554–1561 (1967).
- <sup>24</sup>G. t’Hooft and M. Veltman, “Regularization and renormalization of gauge fields”, Nuclear Physics B **44**, 189–213 (1972).

- <sup>25</sup>N. Cabibbo, “Unitary symmetry and leptonic decays”, Phys. Rev. Lett. **10**, 531–533 (1963).
- <sup>26</sup>M. Kobayashi and T. Maskawa, “CP-Violation in the Renormalizable Theory of Weak Interaction”, Progress of Theoretical Physics **49**, 652–657 (1973).
- <sup>27</sup>B. Pontecorvo, “Mesonium and anti-mesonium”, Sov. Phys. JETP **6**, [Zh. Eksp. Teor. Fiz. 33, 549(1957)], 429 (1957).
- <sup>28</sup>B. Pontecorvo, “Neutrino Experiments and the Problem of Conservation of Leptonic Charge”, Sov. Phys. JETP **26**, [Zh. Eksp. Teor. Fiz. 53, 1717(1967)], 984–988 (1968).
- <sup>29</sup>M. Nakagawa, S. Sakata, and Z. Maki, “Remarks on the Unified Model of Elementary Particles”, Progress of Theoretical Physics **28**, 870–880 (1962).
- <sup>30</sup>J. J. Condon and A. M. Matthews, “ $\Lambda$ CDM cosmology for astronomers”, Publications of the Astronomical Society of the Pacific **130**, 073001 (2018).
- <sup>31</sup>M. Roos, “Dark Matter: The evidence from astronomy, astrophysics and cosmology”, arXiv e-prints, arXiv:1001.0316, arXiv:1001.0316 (2010).
- <sup>32</sup>F. Zwicky, “Die Rotverschiebung von extragalaktischen Nebeln”, Helvetica Physica Acta **6**, 110–127 (1933).
- <sup>33</sup>G. D’Amico, M. Kamionkowski, and K. Sigurdson, “Dark Matter Astrophysics”, arXiv e-prints, arXiv:0907.1912, arXiv:0907.1912 (2009).
- <sup>34</sup>V. C. Rubin, W. K. Ford Jr., and N. Thonnard, “Rotational properties of 21 SC galaxies with a large range of luminosities and radii, from NGC 4605 /R = 4kpc/ to UGC 2885 /R = 122 kpc/”, **238**, 471–487 (1980).
- <sup>35</sup>A. H. Broeils, K. G. Begeman, and R. H. Sanders, “Extended rotation curves of spiral galaxies: dark haloes and modified dynamics”, Monthly Notices of the Royal Astronomical Society **249**, 523–537 (1991).
- <sup>36</sup>R. Massey, T. Kitching, and J. Richard, “The dark matter of gravitational lensing”, Reports on Progress in Physics **73**, 086901 (2010).

- <sup>37</sup>D. Clowe, M. Bradač, A. H. Gonzalez, M. Markevitch, S. W. Randall, C. Jones, and D. Zaritsky, “A direct empirical proof of the existence of dark matter”, *The Astrophysical Journal* **648**, L109–L113 (2006).
- <sup>38</sup>G. Jungman, M. Kamionkowski, and K. Griest, “Supersymmetric dark matter”, *Physics Reports* **267**, 195–373 (1996).
- <sup>39</sup>N. Aghanim et al., “Planck 2018 results. VI. Cosmological parameters”, (2018).
- <sup>40</sup>G. G. Raffelt, “Astrophysical axion bounds”, in *Axions: theory, cosmology, and experimental searches*, edited by M. Kuster, G. Raffelt, and B. Beltrán (Springer Berlin Heidelberg, Berlin, Heidelberg, 2008), pp. 51–71.
- <sup>41</sup>V. Anastassopoulos et al., “New CAST Limit on the Axion-Photon Interaction”, *Nature Phys.* **13**, 584–590 (2017).
- <sup>42</sup>N. Du et al., “Search for invisible axion dark matter with the axion dark matter experiment”, *Phys. Rev. Lett.* **120**, 151301 (2018).
- <sup>43</sup>C. Boutan et al., “Piezoelectrically tuned multimode cavity search for axion dark matter”, *Phys. Rev. Lett.* **121**, 261302 (2018).
- <sup>44</sup>M. Drewes, “The Phenomenology of Right Handed Neutrinos”, *Int. J. Mod. Phys. E* **22**, 1330019 (2013).
- <sup>45</sup>A. Boyarsky, O. Ruchayskiy, and M. Shaposhnikov, “The role of sterile neutrinos in cosmology and astrophysics”, *Annual Review of Nuclear and Particle Science* **59**, 191–214 (2009).
- <sup>46</sup>A. Boyarsky, M. Drewes, T. Lasserre, S. Mertens, and O. Ruchayskiy, “Sterile neutrino dark matter”, *Progress in Particle and Nuclear Physics* **104**, 1–45 (2019).
- <sup>47</sup>D. Abercrombie et al., “Dark Matter Benchmark Models for Early LHC Run-2 Searches: Report of the ATLAS/CMS Dark Matter Forum”, edited by A. Boveia, C. Doglioni, S. Lowette, S. Malik, and S. Mrenna (2015).
- <sup>48</sup>P. Harris, V. V. Khoze, M. Spannowsky, and C. Williams, “Constraining dark sectors at colliders: beyond the effective theory approach”, *Phys. Rev. D* **91**, 055009 (2015).

- <sup>49</sup>E. Gabrielli, B. Mele, F. Piccinini, and R. Pittau, “Asking for an extra photon in higgs production at the lhc and beyond”, Journal of High Energy Physics **2016**, 3 (2016).
- <sup>50</sup>T. M. Undagoitia and L. Rauch, “Dark matter direct-detection experiments”, Journal of Physics G: Nuclear and Particle Physics **43**, 013001 (2015).
- <sup>51</sup>D. S. Akerib et al., “Results from a search for dark matter in the complete lux exposure”, Phys. Rev. Lett. **118**, 021303 (2017).
- <sup>52</sup>R. Agnese et al., “New results from the search for low-mass weakly interacting massive particles with the cdms low ionization threshold experiment”, Phys. Rev. Lett. **116**, 071301 (2016).
- <sup>53</sup>C. Amole et al., “Dark matter search results from the PICO–60 C3f8 bubble chamber”, Phys. Rev. Lett. **118**, 251301 (2017).
- <sup>54</sup>T. R. Slatyer, “Indirect Detection of Dark Matter”, in Proceedings, Theoretical Advanced Study Institute in Elementary Particle Physics : Anticipating the Next Discoveries in Particle Physics (TASI 2016): Boulder, CO, USA, June 6-July 1, 2016 (2018), pp. 297–353.
- <sup>55</sup>L. Accardo et al., “High statistics measurement of the positron fraction in primary cosmic rays of 0.5–500 gev with the alpha magnetic spectrometer on the international space station”, Phys. Rev. Lett. **113**, 121101 (2014).
- <sup>56</sup>M. Ackermann et al., “Searching for dark matter annihilation from milky way dwarf spheroidal galaxies with six years of fermi large area telescope data”, Phys. Rev. Lett. **115**, 231301 (2015).
- <sup>57</sup>J. M. Gaskins, “A review of indirect searches for particle dark matter”, Contemporary Physics **57**, 496–525 (2016).
- <sup>58</sup>M. Aartsen et al., “Improved limits on dark matter annihilation in the sun with the 79-string IceCube detector and implications for supersymmetry”, Journal of Cosmology and Astroparticle Physics **2016**, 022–022 (2016).

- <sup>59</sup>L. Evans and P. Bryant, “LHC machine”, Journal of Instrumentation **3**, S08001–S08001 (2008).
- <sup>60</sup>M. Benedikt, P. Collier, V. Mertens, J. Poole, and K. Schindl, *LHC Design Report*, CERN Yellow Reports: Monographs (CERN, Geneva, 2004).
- <sup>61</sup>E. Mobs, “The CERN accelerator complex - August 2018”, General Photo (2018).
- <sup>62</sup>*CMS luminosity - public results*, (2019) <https://twiki.cern.ch/twiki/bin/view/CMSPublic/LumiPublicResults> (visited on 03/19/2019).
- <sup>63</sup>M. Perelstein, “Introduction to collider physics”, (2010) 10.1142/9789814327183\_0008.
- <sup>64</sup>J. C. Collins, D. E. Soper, and G. Sterman, “Factorization of hard processes in qcd”, in *Perturbative qcd* (1989), pp. 1–91.
- <sup>65</sup>Y. L. Dokshitzer, “Calculation of the Structure Functions for Deep Inelastic Scattering and e+ e- Annihilation by Perturbation Theory in Quantum Chromodynamics.”, Sov. Phys. JETP **46**, [Zh. Eksp. Teor. Fiz. 73, 1216(1977)], 641–653 (1977).
- <sup>66</sup>V. N. Gribov and L. N. Lipatov, “Deep inelastic e p scattering in perturbation theory”, Sov. J. Nucl. Phys. **15**, [Yad. Fiz. 15, 781(1972)], 438–450 (1972).
- <sup>67</sup>G. Altarelli and G. Parisi, “Asymptotic freedom in parton language”, Nuclear Physics B **126**, 298–318 (1977).
- <sup>68</sup>R. D. Ball et al., “Parton distributions for the lhc run ii”, Journal of High Energy Physics **2015**, 40 (2015).
- <sup>69</sup>J. Alwall et al., “The automated computation of tree-level and next-to-leading order differential cross sections, and their matching to parton shower simulations”, Journal of High Energy Physics **2014**, 79 (2014).
- <sup>70</sup>R. Frederix and S. Frixione, “Merging meets matching in mc@nlo”, Journal of High Energy Physics **2012**, 61 (2012).
- <sup>71</sup>T. Sjostrand et al., “An introduction to pythia 8.2”, English, Computer Physics Communications **191**, 159–177 (2015).

- <sup>72</sup>B. Andersson, G. Gustafson, G. Ingelman, and T. Sjostrand, “Parton fragmentation and string dynamics”, Physics Reports **97**, 31–145 (1983).
- <sup>73</sup>S. Chatrchyan et al., “The CMS experiment at the CERN LHC”, Journal of Instrumentation **3**, S08004–S08004 (2008).
- <sup>74</sup>*CMS detector design*, (2019) <http://cms.web.cern.ch/news/cms-detector-design> (visited on 11/23/2011).
- <sup>75</sup>S. Agostinelli et al., “Geant4 simulation toolkit”, Nuclear Instruments and Methods in Physics Research Section A: Accelerators, Spectrometers, Detectors and Associated Equipment **506**, 250–303 (2003).
- <sup>76</sup>J. Allison et al., “Geant4 developments and applications”, IEEE Transactions on Nuclear Science **53**, 270–278 (2006).
- <sup>77</sup>A. Sirunyan et al., “Particle-flow reconstruction and global event description with the CMS detector”, Journal of Instrumentation **12**, P10003–P10003 (2017).
- <sup>78</sup>The CMS Collaboration, “Description and performance of track and primary-vertex reconstruction with the CMS tracker”, Journal of Instrumentation **9**, P10009–P10009 (2014).
- <sup>79</sup>A. Sirunyan et al., “Identification of heavy-flavour jets with the CMS detector in pp collisions at 13 TeV”, Journal of Instrumentation **13**, P05011–P05011 (2018).
- <sup>80</sup>The CMS Collaboration, “Performance of electron reconstruction and selection with the CMS detector in proton-proton collisions at  $\sqrt{s} = 8$  TeV”, Journal of Instrumentation **10**, P06005–P06005 (2015).
- <sup>81</sup>The CMS Collaboration, “Performance of photon reconstruction and identification with the CMS detector in proton-proton collisions at  $\sqrt{s} = 8$  TeV”, Journal of Instrumentation **10**, P08010–P08010 (2015).
- <sup>82</sup>*CMS luminosity measurements for the 2016 data taking period*, CMS Physics Analysis Summary CMS-PAS-LUM-17-001 (CERN, 2017).

- <sup>83</sup>G. Bozzi, S. Catani, G. Ferrera, D. de Florian, and M. Grazzini, “Production of Drell-Yan lepton pairs in hadron collisions: Transverse-momentum resummation at next-to-next-to-leading logarithmic accuracy”, Phys. Lett. **B696**, 207–213 (2011).
- <sup>84</sup>A. Denner, S. Dittmaier, M. Hecht, and C. Pasold, “NLO QCD and electroweak corrections to  $W + \gamma$  production with leptonic  $W$ -boson decays”, JHEP **04**, 018 (2015).
- <sup>85</sup>A. Denner, S. Dittmaier, M. Hecht, and C. Pasold, “NLO QCD and electroweak corrections to  $Z + \gamma$  production with leptonic  $Z$ -boson decays”, JHEP **02**, 057 (2016).
- <sup>86</sup>J. M. Lindert et al., “Precise predictions for  $V +$  jets dark matter backgrounds”, Eur. Phys. J. **C77**, 829 (2017).
- <sup>87</sup>M. J. Ambrose et al., “A novel beam halo monitor for the CMS experiment at the LHC”, JINST **10**, P11011 (2015).
- <sup>88</sup>D. Petyt et al., *Characterization and treatment of anomalous signals in the cms electromagnetic calorimeter*, CMS Note 2010/357 (2010).
- <sup>89</sup>D. A. Petyt et al., “Mitigation of anomalous APD signals in the CMS electromagnetic calorimeter”, J. Phys.: Conf. Series **404**, 012043 (2012).
- <sup>90</sup>K. Belasco et al., “The RooStats Project”, PoS **ACAT2010**, Comments: 11 pages, 3 figures, ACAT2010 Conference Proceedings, 057 (2010).
- <sup>91</sup>T. Junk, “Confidence level computation for combining searches with small statistics”, Nucl. Instrum. Meth. A **434**, 435 (1999).
- <sup>92</sup>A. L. Read, “Presentation of search results: the  $cl_s$  technique”, J. Phys. G **28**, 2693 (2002).
- <sup>93</sup>G. Cowan, K. Cranmer, E. Gross, and O. Vitells, “Asymptotic formulae for likelihood-based tests of new physics”, Eur. Phys. J. C **71**, [Erratum: 10.1140/epjc/s10052-013-2501-z], 1554 (2011).
- <sup>94</sup>P. A. R. Ade et al., “Planck 2015 results. XIII. Cosmological parameters”, Astron. Astrophys. **594**, A13 (2016).

- <sup>95</sup>M. Backović, K. Kong, and M. McCaskey, “MadDM v.1.0: computation of dark matter relic abundance using MadGraph5”, Phys. Dark Univ. **5-6**, 18 (2014).
- <sup>96</sup>M. Aaboud et al., “Search for dark matter at  $\sqrt{s} = 13$  tev in final states containing an energetic photon and large missing transverse momentum with the atlas detector”, The European Physical Journal C **77**, 393 (2017).
- <sup>97</sup>G. Busoni et al., “Recommendations on presenting LHC searches for missing transverse energy signals using simplified  $s$ -channel models of dark matter”, 2016.
- <sup>98</sup>X. Cui et al., “Dark matter results from 54-ton-day exposure of PandaX-II experiment”, Phys. Rev. Lett. **119**, 181302 (2017).
- <sup>99</sup>E. Aprile et al., “Dark matter search results from a one Tonne  $\times$  Year exposure of XENON1T”, 2018.
- <sup>100</sup>G. Angloher et al., “Results on light dark matter particles with a low-threshold CRESST-II detector”, Eur. Phys. J. C **76**, 25 (2016).
- <sup>101</sup>E. Behnke et al., “Final results of the PICASSO dark matter search experiment”, Astropart. Phys. **90**, 85 (2017).
- <sup>102</sup>K. Choi et al., “Search for neutrinos from annihilation of captured low-mass dark matter particles in the Sun by Super-Kamiokande”, Phys. Rev. Lett. **114**, 141301 (2015).
- <sup>103</sup>The CMS Collaboration, *Simplified likelihood for the re-interpretation of public CMS results*, CMS Note CMS-NOTE-2017-001 (2017).